INVESTIGATING THE CATALYTIC MECHANISM OF THE *meta*-CLEAVAGE PRODUCT HYDROLASES

by

Antonio C. Ruzzini

B.Sc. (Honours), Trent University, 2008

A THESIS SUBMITTED IN PARTIAL FULFILLMENT OF

THE REQUIREMENTS FOR THE DEGREE OF

DOCTOR OF PHILOSOPHY

in

THE FACULTY OF GRADUATE AND POSTDOCTORAL STUDIES

(Biochemistry and Molecular Biology)

THE UNIVERSITY OF BRITISH COLUMBIA

(Vancouver)

September 2013

ABSTRACT

The *meta*-cleavage product (MCP) hydrolases are members of the α/β-hydrolase superfamily that utilize a Ser-His-Asp triad to catalyze the hydrolysis of a C-C bond. The catalytic mechanism of the MCP hydrolases is poorly defined and particularly interesting due to a requisite substrate ketonization that precedes hydrolysis. To resolve the catalytic mechanism of the MCP hydrolases, two enzymes were studied: tetrameric $BphD_{LB400}$ from *Burkholderia xenovorans* LB400 and dimeric DxnB2 from *Sphingomonas witichii* RW1. Both efficiently hydrolyze 2-hydroxy-6-oxo-6-phenylhexa-2,4-dienoic acid (HOPDA) to produce 2-hydroxypenta-2,4-dienoic acid (HPD) and benzoic acid.

A series of experiments established that $BphD_{LB400}$ uses an histidine-independent nucleophilic mechanism of catalysis and is half-site reactive. Benzoylation of Ser112 was demonstrated by LC ESI/MS/MS analyses and a pre-steady-state kinetic burst of HPD formation indicated the reactivity. While acylation during HOPDA hydrolysis by $BphD_{LB400}$ occurred on a similar timescale for the WT and H265Q variant, esterase activity was abrogated in the histidine variant. Thus, alternative mechanisms of nucleophile activation are employed for C-C and C-O bond cleavage.

A covalent mechanism of catalysis was inferred for DxnB2, however, the turnover of HOPDA was 1:1 with respect to enzyme concentration. A solvent kinetic isotope effect suggested that a proton transfer, and therefore, substrate ketonization determines the rate of acylation in the MCP hydrolases. Substrate ketonization, and therefore acylation, can be indirectly observed as consumption of ES^{red}, an intermediate named for its bathochromically-shifted absorption spectrum. A proton transfer to ES^{red} allowed the assignment of this species to an enzyme-bound HOPDA dianion. An extended Brønsted analysis revealed a linear

correlation between substrate basicity and the rate constant determined for the ketonization reaction. Finally, the MCP hydrolase P-subsite, which contacts the MCP dienoate moiety, was definitively linked to substrate ketonization. In DxnB2 Asn43 and Arg180 variants, ES^{red} formation was found to limit this proton transfer reaction.

A substrate-assisted nucleophilic mechanism of catalysis has been proposed for the MCP hydrolases. Therein, the electron-rich dienoate moiety substitutes for the His-Asp pair as the general base for nucleophile activation. Overall, definition of the chemical mechanism of the MCP hydrolases has implications for environmental bioremediation strategies and the rational design of therapeutics.

PREFACE

Several parts of this thesis have been published in or submitted to refereed journals; an asterisk has been used to indicate shared authorship. Two of these manuscripts are a result of a fruitful collaboration with the laboratory of Jeffrey T. Bolin at Purdue University. In each, the Bolin Lab was responsible for crystallization, X-ray diffraction experiments and the generation and refinement of three-dimensional models of $BphD_{LB400}$ and DxnB2.

(1) Ruzzini AC*, Ghosh S*, Horsman GP, Foster LJ, Bolin JT, and Eltis LD. 2012. Identification of an acyl-enzyme intermediate in a meta-cleavage product hydrolase reveals the versatility of the catalytic triad. *J. Am. Chem. Soc.* **134**, 4615.

For this manuscript, I was responsible for the *in vitro* characterization of $BphD_{LB400}$ WT and H265Q, including kinetic and chemical quench experiments, the preparation of samples and analysis of protein MS experiments, and the characterization reactions in $H_2{}^{18}O$.

(2) Ruzzini AC, Horsman GP, Eltis LD. 2012. The catalytic serine of meta-cleavage product hydrolases is activated differently for C-O bond cleavage than for C-C bond cleavage. *Biochemistry* **51**, 5831.

For this manuscript, I was responsible for the characterization of the rate-limiting step for MCP hydrolases catalysis, the $BphD_{LB400}$ methanol-dependent esterase activity, the mechanism of nucleophile activation for C-O bond cleavage, and empirically determining the steady-state partitioning of methano- and hydrolysis reaction products.

(3) Ruzzini AC*, Bhowmik S*, Yam KC, Ghosh S, Bolin JT, and Eltis LD. 2013. The lid domain of the MCP hydrolase DxnB2 contributes to an increased specificity for recalcitrant PCB metabolites. *Biochemistry* **52**, 5685.

For this manuscript, I was responsible for the transient-state kinetic analysis of DxnB2-mediate turnover of recalcitrant 3-Cl HOPDAs, analysis of the enzyme's oligomeric state and the comparison of seven MCP hydrolases, which lead to discovery of previously unrecognized determinants in enzyme oligomeric state stabilization as well as determinants in substrate specificity.

TABLE OF CONTENTS

LIST OF TABLES

LIST OF FIGURES

ABBREVIATIONS

$1/\tau$	reciprocal relaxation time
Abs	absorbance
Amp	amplitude
AU	absorbance units
BPDO	biphenyl dioxygenase (EC 1.14.12.18)
CoA	coenzyme A
DHB	2,3-dihydroxybiphenyl
EI	electron ionization
ESI	electrospray ionization
FAD	flavin adenine dinucleotide
GSH/GSSG	reduced glutathione/oxidized glutathione
HEPES	4-(2-hydroxyethyl)-1-piperazineethansulfonic acid
HOPDA	2-hydroxy-6-oxo-6-phenylhexa-2,4-dienoic acid
HPD	2-hydroxypenta-2,4-dienoic acid
HPLC	high performance liquid chromatography
KPi	potassium phosphate
LC	liquid chromatography
MCP	*meta*-cleavage product
MS	mass spectrometery
NADH	β-nicotinamide adenine dinucleotide
NMR	nuclear magnetic resonance
PCB	polychlorinated biphenyl
PDA	photodiode array
pNP	*p*-nitrophenol
pNPB	*p*-nitrophenyl benzoate
SDS-PAGE	sodium dodecyl sulphate polyacrylamide gel electrophoresis
SEC-MALS	Size exclusion chromatography multiple angle light scattering
SKIE	solvent kinetic isotope effect
$t_{1/2}$	half-life
v_0	initial reaction velocity
v_{ss}	steady-state reaction velocity
WT	wild type

ACKNOWLEDGEMENTS

To begin, I would like to thank my supervisor Lindsay Eltis for accepting me into his laboratory and providing me with support and guidance throughout my graduate studies.

I must also acknowledge the past and present members of the Eltis lab. I have had the chance to interact with many enthusiastic researchers but I was most inspired working alongside Carola Dresen, Sachi Okamoto, Hiroshi Otani, Nicolas Seghezzi and Rahul Singh. Along with these individuals, Eugene Kuatsjah, Jon Penfield, Joseph Roberts, and many others in the LSI have been good friends in and outside of the lab. Finally, Jennifer Lian was of great assistance during the purification of a number of DxnB2 variants.

Next, I would like to thank my supervisory committee members, Lawrence McIntosh and Michael Murphy. Both have provided helpful suggestions, support and the opportunity to interact with and learn from their own lab members. Specifically, Mark Okon and Jason Grigg were responsible for training and technical assistance with NMR and X-ray crystallography, respectively. It was a great pleasure to work in close proximity to both of these groups as well as the Beatty, Mauk, Mohn and Davies labs. A special thanks is also required for all the helpful discussions and training provided Fred Rosell.

Many thanks to Jeffrey Bolin, Subhangi Ghosh and Shiva Bhowmik. The structural characterization of BphD and DxnB2 were invaluable for the interpretation of kinetic data and experimental design in the latter stages of my studies.

To the Davies Lab coffee club, thank you for providing stimulating discussions, academic and beyond.

Finally, I would like to thank my family and friends, especially my parents and above everyone else, Marta.

Chapter 1: INTRODUCTION

1.1 Aromatic Compounds

Aromatic compounds are widely distributed in nature, possessing diverse chemical structures and indispensible biological functions (Figure 1). For example, simple low molecular weight aromatic compounds are integral components of nucleic acids, proteins and enzyme cofactors. Moreover, the evolution of biosynthetic pathways for complex high molecular weight aromatic compounds reshaped our environment as approximately 30% of organic carbon in the biosphere is now stored as lignin[1]. Indeed, aromatic compounds are the second most abundant class of organic compounds in nature after the carbohydrates.

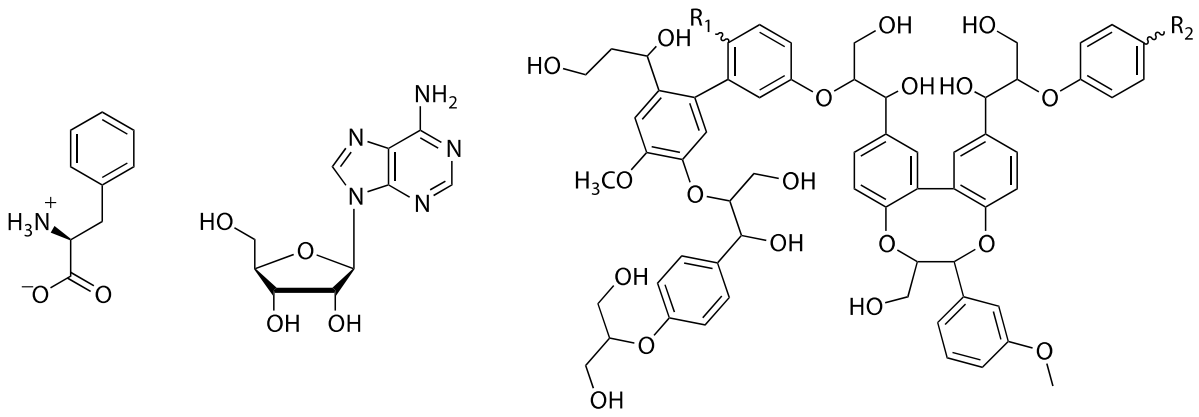

Figure 1. Biologically relevant aromatic compounds: phenylalanine, adenosine and lignin.

Aromaticity is defined by Hückel's rule: an aromatic compound is cyclic, planar, and possesses a conjugated *p*-orbital system that contains $4n + 2\pi$ electrons (where n is a positive integer). Delocalization of these π-electrons acts to lower the energy of the conjugated system and thereby increase the inherent stability of the aromatic molecule.

1.2 Catabolism of aromatic compounds by bacteria

Bacterial catabolic pathways of aromatic-containing biomass contribute significantly to the global carbon cycle. Aerobic, anaerobic and "hybrid" catabolic pathways occur in

nature and use a shared catabolic logic: activation of the aromatic ring followed by its cleavage[2,3]. For polyaromatic compound degradation, an iterative version of this strategy is employed.

In aerobic catabolism, molecular oxygen (O_2) serves as a cosubstrate for two separate reactions: O_2 is utilized for the activation and cleavage of aromatic rings[4]. Several distinct enzymatic processes have been observed for both the activation and oxygenolysis of aromatic rings. Activation is accomplished by the enzymatic incorporation of oxygen, which typically involves dihydroxylation by a non-heme iron-dependent dioxygenase[5] or a single hydroxylation event by a flavin-dependent monooxygenase[6]. In either case, catecholic compounds that are formed by the hydroxylation reactions are eventually cleaved by either an intra- or extradiol dioxygenase (Figure 2A), which generate *ortho* and *meta*-cleavage products (MCPs), respectively[3,7]. The ring-cleavage products are then metabolized by other pathway-specific enzymes and are channeled into central metabolic pathways.

The anaerobic catabolism of aromatic compounds has been less extensively studied than the aerobic catabolism[8]. A significant number of aromatic compounds serve as carbon sources in anoxic environments, including aniline, aromatic amino acids, benzoic acids, catechols, hydroquinones, nicotinate, pyrogallol, α-, β-, and γ-resorcylate and xylene[2]. Despite the plethora of growth substrates, anaerobic catabolism converges on a relatively smaller number of shared metabolites, as observed in aerobic catabolism. The best-studied pathways involve thioesterification, typically by a CoA ligase, for aromatic ring activation (Figure 2B). Alternatively, CoA-independent pathways exploit the susceptibility of multiply *meta*-substituted aromatics to an enol-to-keto tautomerization. The relatively few documented shared cyclic metabolites are then subjected to reductive dearomatization before

entering primary metabolic pathways as aliphatic acids. These latter reactions include a broad range of enzymatic reactions, many of which are poorly characterized. However, hydrolytic ring-opening is a prevalent strategy.

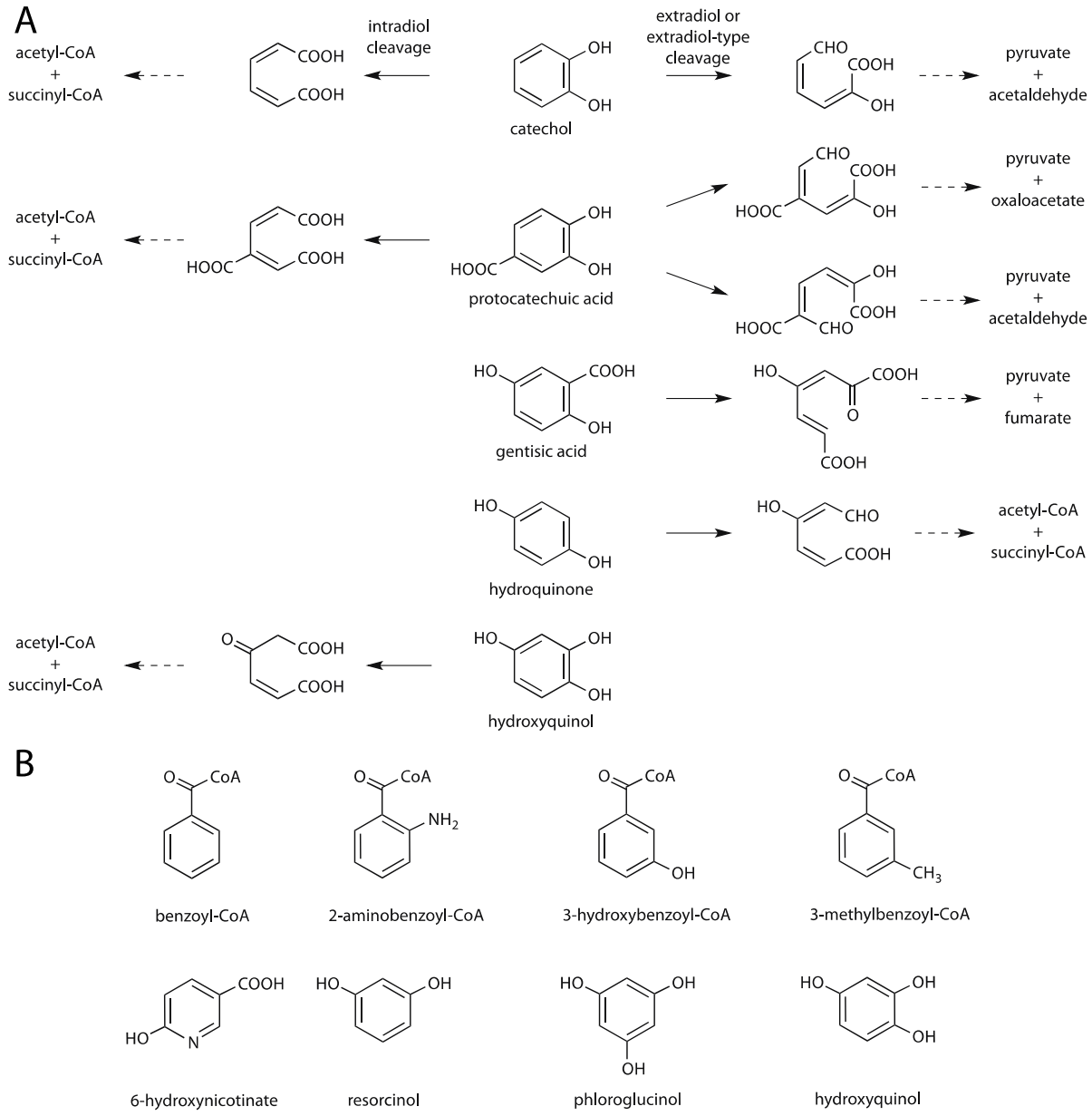

Figure 2. (A) Aerobic, dioxygenase-catalyzed aromatic ring cleavage. The O_2-dependent reactions (solid arrows) and the products of each pathway are shown (dashed arrows indicate from 2 to 5 enzymatic reactions). (B) Shared metabolites that occur in anaerobic aromatic catabolism. Adapted from [2,3].

Finally, in addition to the discrete aerobic and anaerobic pathways, some bacteria utilize “hybrid pathways” to catabolize aromatic compounds. In such pathways, O_2 is used in only one of the two critical steps of ring activation and cleavage. A hybrid pathway was first identified and implicated in the degradation of phenylacetic acid in *Pseudomonas putida* U[9]. Subsequent studies on the benzoyl-CoA oxidizing (Box) pathway enzymes in *Azoarcus evansii*, BoxABC, demonstrated that benzoyl CoA assimilation proceeds through the formation and hydrolysis of a 2,3-epoxy-benzoyl-CoA rather than a catechol in these hybrid pathways[10].

1.2.1 The biphenyl (Bph) pathway

The aerobic biphenyl catabolic pathway is a typical *meta*-cleavage pathway. The microbial capacity to mineralize biphenyl was first described in 1970 when Lunt and Evans demonstrated that it could be utilized as a sole growth substrate by pure cultures of Gram-negative bacteria[11]. This seminal report, reading less than 200 words, also presented three possible biphenyl metabolites: (i) 2,3-dihydroxybiphenyl, (ii) a yellow colored α-hydroxy-β-phenylmuconic semialdehyde (λ_{max} 430 nm), and (iii) phenylpyruvate. Since the pathway’s discovery, all of the enzymatic activities associated with biphenyl utilization have been established and extensively reviewed[12].

While the genes associated with biphenyl degradation can be encoded within a single operon, the Bph pathway has been conceptually divided into upper and lower pathways. The upper Bph pathway generates 2-hydroxypenta-2,4-dienoic acid (HPD) and benzoic acid from biphenyl whereas the lower pathway metabolizes HPD to acetyl-CoA and pyruvate, which can enter the citric acid cycle. Historically, the upper and lower pathways have also been studied from distinct research perspectives. The ability of the upper Bph pathway to

transform polychlorinated biphenyls (PCBs; see section 1.2.2) was the impetus for the earliest genetic and biochemical studies[13,14]. In contrast, recent studies on lower pathway enzymes have focused on enzyme engineering for the production of enantiomerically pure antiobiotic precursors[15].

The upper Bph pathway comprises four enzymatic steps that result in the *meta*-cleavage of one of the biphenyl rings (Figure 3). The first step is catalyzed by biphenyl 2,3-dioxygenase (BPDO), a multicomponent enzyme that includes a two-subunit Rieske non-heme iron dioxygenase (BphAE), a ferredoxin (BphF), and an FAD-containing reductase (BphG)[13,16]. BPDO utilizes O_2 and two electrons derived from NADH to transform biphenyl to *cis*-2,3-dihydro-DHB, which is then reduced to DHB by BphB at the expense of NAD^+. The third enzyme, BphC is an Fe(II)-dependent extradiol dioxygenase that incorporates O_2 into the catecholic ring of DHB, generating an MCP, 2-hydroxy-6-oxo-6-phenylhexa-2,4-dienoic acid (HOPDA). Finally, BphD, an MCP hydrolase, uses water to catalyze the fission of a carbon-carbon (C-C) bond to yield HPD and benzoic acid.

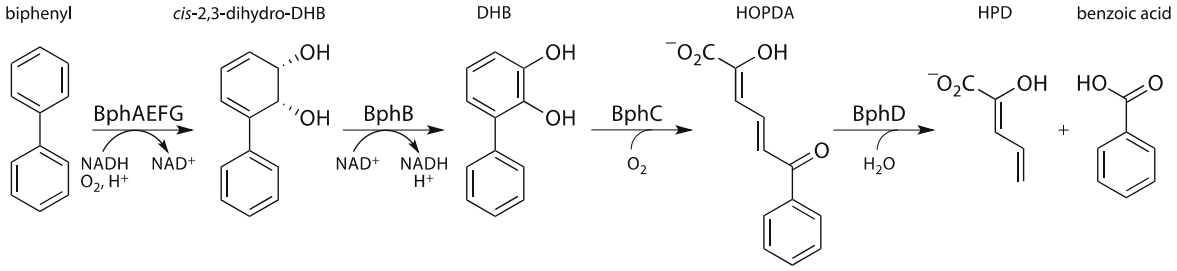

Figure 3. The upper Bph pathway.

1.2.2 The Bph pathway can cometabolize PCBs

PCBs are aromatic xenobiotic compounds that had prominent industrial applications in the twentieth century[17]. The chlorination of biphenyl theoretically yields 209 possible congeners. However, commercial mixtures of PCBs typically included from twenty to sixty

congeners containing three to six chlorine substitutions. Links between PCB exposure and a multitude of human diseases including cancers, developmental and neurological disorders (reviewed in [18]) ultimately led to bans on their use and production that began in the 1970s. Nevertheless, it is estimated that approximately 10% of all PCBs manufactured, amounting to ~2.8×10^8 kilograms, are still present in mobile environmental reservoirs[17] and exposure remains a health risk[19].

In general, studies of bacterial PCB degradation have revealed the process to be strain-dependent and limited by the degree and position of chlorination on each PCB congener[14]. Therefore, the degradation patterns observed in bacteria directly reflect the respective substrate specificities of enzymes encoded by the corresponding *bph* genes. Among the most potent PCB-degrading bacteria, *Burkholderia xenovorans* LB400 is remarkable not only for its ability to transform certain hexachlorinated congeners[20], but also due to the recruitment of a reductive dehalogenase to its *bph* operon[21].

The molecular characterization of PCB-degradation in bacteria has focused almost exclusively on the upper Bph pathway's dioxygenases. As the initiating enzyme, BPDO congener specificity has been thoroughly investigated in a number of homologues[20,22,23], and the reported substrate ranges are often used to classify the corresponding bacterium[24]. Recently, metagenomic analyses of PCB-contaminated soils revealed extensive diversity in the toluene/biphenyl dioxygenases[25], and phylogenetic analyses demonstrated that BPDO could be subgrouped based on sequence similarity to at least two well-characterized enzymes from potent PCB-degrading soil bacteria[26]. More specifically, class I was correlated to *bph*A from *B. xenovorans* LB400 and class II to *Pseudomonas pseudoalcaligenes* KF707. A possible third class was similar to BPDO from *Rhodococcus jostii* RHA1, although biphenyl

may not be the cognate substrate of this enzyme considering that it shares ~40% identity to an alkylbenzene dioxygenase from *Rhodococcus strain* sp. DK17[27]. Moreover, this strain cannot use biphenyl as a growth substrate[28] and encodes for a ring-cleaving dioxygenase that is identical to a gene annotated as ethylbenzene dioxygenase in *R. jostii* RHA1[29]. Attempts to increase the range of congeners cometabolized by the Bph pathway have focused on expanding the substrate specificity of BPDO using directed evolution[30-34]. In addition, laboratory evolution of 1,2-dihydroxynapthalene dioxygenase, DoxG, a BphC homologue yielded an enzyme with increased specificity for 3,4-dihydroxybiphenyls, which are often produced during PCB degradation[35]. In spite of the naturally encoded genetic diversity present throughout soil-dwelling bacteria and ongoing *in vitro* efforts, a number of highly recalcitrant and "dead-end" metabolites still represent significant bottlenecks to both naturally occurring and potential anthropogenic bioremediation strategies.

1.2.3 BphD is a determinant of PCB degradation

The reaction catalyzed by BphD, the final enzyme of the upper Bph pathway, is a common bottleneck during PCB degradation by bacteria. At least three observations indicate that BphD activity can determine the extent and rate PCB cometabolism. First, yellow-coloured metabolites, specifically 3-Cl HOPDAs, accumulated during bacterial growth on 2,4'-dichlorobiphenyls[14]. Second, this accumulation was strain-independent[36]. Finally, 3-Cl HOPDAs inhibit BphD[37,38]. Steady-state kinetic characterization of several BphD homologues revealed that phenyl-substituents have a relatively modest effect on turnover whereas dienoate-substituents, particularly at C3, have pronounced detrimental effects on catalysis[37-39]. In fact, the inability of Bph pathway hydrolases to metabolize recalcitrant HOPDAs is reflected in the recruitment of a glutathione *S*-transferase, BphK, which

catalyzes a reductive dehalogenation of 3 and 5-Cl HOPDAs at the expense of two molecules of glutathione (GSH) in a subset of bacteria (Figure 4). Nevertheless, many powerful PCB-degraders, such as *R. jostii* RHA1 cannot produce GSH, underlining the importance of understanding the catalytic limitations of BphD. Along these lines, DxnB2, an MCP hydrolase from *Sphingomonas witichii* RW1, was recently distinguished for its reactivity towards recalcitrant 3-Cl HOPDAs[39]. In comparison to BphD from *B. xenovorans* LB400 ($BphD_{LB400}$) and BphD from *Rhodococcus globerulus* P6 ($BphD_{P6}$), DxnB2 was 13- and 83-fold more specific (k_{cat}/K_M) for the model PCB metabolite 3-Cl HOPDA or 3.4- and > 2600-fold more specific for the biologically relevant 3,9,11 tri-Cl HOPDA.

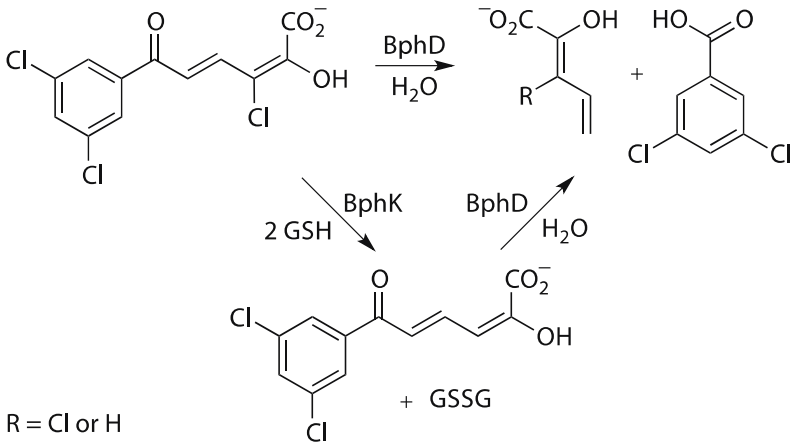

Figure 4. The metabolic fate(s) of 3-Cl HOPDAs in soil bacteria.

1.2.4 The MCP hydrolases

MCP hydrolases such as BphD (EC 3.7.1.8) belong to the α/β-hydrolase superfamily. As outlined above, MCPs are characterized by a 2,6-dioxo-2,4-dienoic acid moiety that results from the extradiol cleavage of catechols (Figure 5). Mirroring the trend in the study of aromatic compound degradation, most identified MCP hydrolases occur in soil-dwelling bacteria. One exception is HsaD, which occurs in a steroid catabolic pathway found in a range of bacteria including the intracellular pathogen *Mycobacterium tuberculosis*[40,41].

$BphD_{LB400}$ along with 2-hydroxy-6-oxo-nona-2,4-diene-1,9-dioic acid 5,6- hydrolase, MhpC from the phenylproprionate degradation pathway of *Escherichia coli* W3110, are considered the archetypical MCP hydrolases following a large body of work on these enzymes.

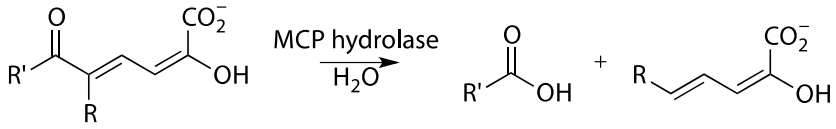

Figure 5. The MCP hydrolase reaction.

1.2.5 The α/β-hydrolase superfamily

The catalytic versatility of the α/β-hydrolase fold was first highlighted by a structural comparison of five hydrolytic enzymes acting on different substrates[42]. In fact, the α/β-hydrolases were among the earliest reported examples of divergent enzyme evolution, which constitutes the basis for the classification of enzymes into superfamilies. Since the discovery of the α/β-hydrolase superfamily, the known chemical reactions have expanded from hydrolyses and acyl transfers involving carbon-heteroatom (C-X) bonds to a number of more interesting reactions including C-C bond cleavage and the cofactor-less activation of O_2 (Figure 6).

The α/β-hydrolase fold consists of an eight-stranded, mostly parallel, β-sheet that is characterized by a left-handed superhelical twist, and is surrounded by α-helices[43]. Typically, catalysis by this superfamily originates from a triad of residues that includes a nucleophile, an invariant histidine, and the conjugate base of an acidic amino acid. Reactions are further supported by an 'oxyanion hole,' and inspection of the active site reveals a mirror image relationship between the α/β-hydrolases and the serine proteases[42]. Interestingly, the α-helical content of the α/β-hydrolases is variable. Only the αC-helix, which is part of a

structurally conserved strand-turn-helix motif that carries the catalytic nucleophile is conserved. The nucleophilic residue, an Asp, Cys or Ser, is embedded within a Small-X_1-Nu-

Activity	Catalytic Triad	Example Reaction	Reaction mechanism
esterase	Ser-His-Asp	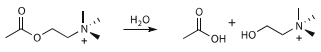	nucleophilic
esterase	Cys-His-Asp	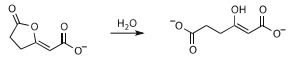	nucleophilic
esterase	Ser-His	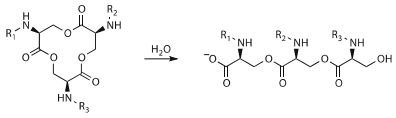	nucleophilic
C-peptidase	Ser-His-Asp	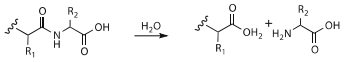	nucleophilic
N-peptidase	Ser-His-Asp	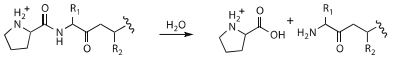	nucleophilic
lipase	Ser-His-Asp	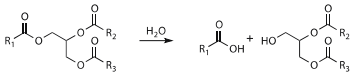	nucleophilic
thioesterase	Ser-His-Asp	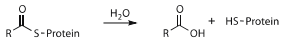	nucleophilic
lactamase	Ser-His-Asp	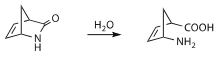	nucleophilic
epoxide hydrolase	Asp-His-Asp	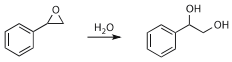	nucleophilic
C-C bond hydrolase	Ser-His-Asp	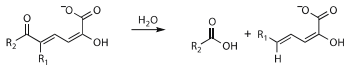	*general base*
fluoroacetate dehalogenase	Asp-His-Asp	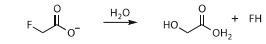	nucleophilic
haloalkane dehalogenase	Asp-His-Asp	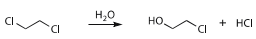	nucleophilic
perhydrolase	Ser-His-Asp	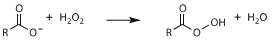	nucleophilic
acetyltransferase	Ser-His-Asp	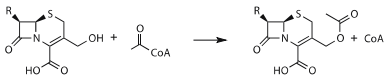	nucleophilic
acyltransferase	Ser-His-Glu	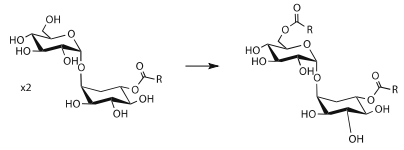	nucleophilic
hydroxynitrile lyase	Ser-His-Asp	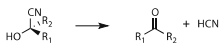	general base
cofactor-less dixoygenase	Ser-His-Asp	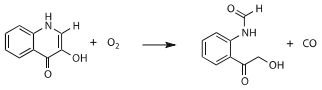	general base

Figure 6. Examples of α/β-hydrolase-catalyzed reactions. The catalytic triad and the proposed catalytic mechanism for each are listed. Adapted from [44].

X_2-Small consensus sequence located within this structural motif that includes β5 and αC, where the "Small" residues are typically glycines and X_n indicates any amino acid. The nucleophile resides at the tip of this sharp turn called the 'nucleophile elbow'[42], which also provides geometric constraints for the surrounding residues. Specifically, the main chain amide of X_2 is positioned to form one half of the 'oxyanion hole.' The invariant catalytic His is carried on a loop, referred to as the Histidine-loop, extending from β8 and positioning the residue near the conjugate base of an acidic residue (Asp or Glu) that occurs primarily after β7. Notably, an α/β-hydrolase with an atypical Ser-His dyad has also been observed[45].

The ability of the α/β-hydrolase fold to tolerate a large number of distinct insertions has been credited for the wide range of chemistry originating from a relative well-conserved active site[43,44]. Insertions of varying size typically occur at β3, β4, β6, β7 or β8. Among the insertions, a flexible cap or lid domain after β6 is preeminent (Figure 6). For example, the epoxide and MCP hydrolases share similar lid domains yet sequence identity and seemingly subtle structural differences effectively modulate active site geometry and act as

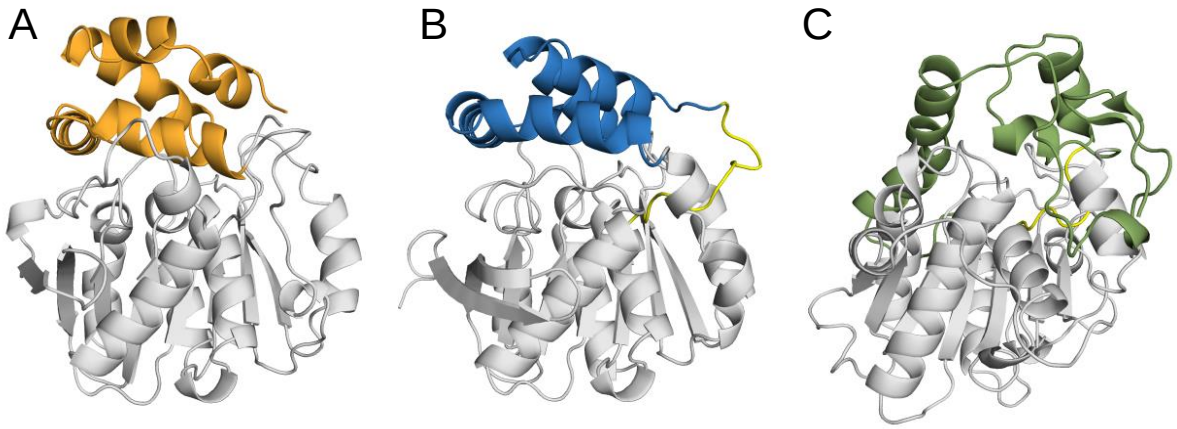

Figure 7. Distinct α/β-hydrolase lids at the common β6 insertion point. (A) Epoxide hydrolase from *Agrobacterium radiobacter* AD1 (PDB ID: 1EHY, chain A). (B) $BphD_{LB400}$ (PDB ID: 2OG1, chain A). (C) *Candida antartica* lipase B (PDB ID: 1LBS, chain A). The α/β-hydrolase core is coloured white, the lid domains are distinctly coloured, and the NC-loop (disordered in 1EHY) is coloured yellow.

determinants of substrate specificity. Finally, the identity of loops extending from α/β-hydrolase core to the different lid domains have also been implicated in catalysis[46,47]. The NC-loop, which extends from β6 connecting the core and N-terminus of the lid domain, is a common example.

In keeping with the conserved catalytic machinery, a nucleophilic mechanism of catalysis has been assigned to most α/β-hydrolases (Figure 6). Early experiments probing catalysis in the α/β-hydrolases superfamily employed radiolabeled substrates. Initially, acetylation of pancreatic lipase[48,49] and a carbethoxylated cutinase enzyme[50] was demonstrated using highly reactive *p*-nitrophenyl [^{3}H]-acetate and *p*-nitrophenyl [1-^{14}C]-acetate, respectively. Later, evidence for covalent catalysis during the turnover of cognate substrates, [^{3}H]-acetylcholine and [^{3}H]-myristoyl-CoA was provided for acetylcholine esterase[51] and myristoyl-ACP thioesterase[52]. Most recently, [^{14}C]-acetylCoA-labeling and mechanism-based inhibition have defined a nucleophilic mechanism for homoserine transacetylases[53,54], and a crystal structure has been reported for an acetlyated deacetylcephalosporin C acetyltransferase[55]. Perhaps the best-characterized catalytic cycle, however, is that of haloalkane dehalogenase for which crystallographic snapshots are available that define a putative reaction coordinate, and include a covalent intermediate[56]. Other α/β-hydrolase families with inferred nucleophilic mechanisms include C- and N-terminal peptidases[57,58], dienelactone hydrolase[59], the human fatty acid synthase thioesterase domain[60] and enzymes that can moonlight as perhydrolases[61]. Indeed, despite the wealth of indirect evidence for covalent catalysis, direct experimental observation of an acyl-enzyme has only been reported for relatively few members of the α/β-hydrolase superfamily.

In contrast, a general base mechanism of catalysis has been proposed for at least three families of α/β-hydrolases. General base mechanisms have been proposed for each of two different hydroxynitrile lyases possessing opposite enantioselectivity: paralleled by distinct proton transfer relay systems[62]. More particularly, the proton from the incipient hydroxyl is abstracted by the histidine and transferred to the cyanide leaving group in the *R*-selective enzyme whereas abstraction and transfer are catalyzed by the serine and histidine, respectively, in the *S*-selective hydroxynitrile lyases. The catalytic histidine has also been ascribed a role as a general base for the deprotonation of hydroxyl-containing substrates in the cofactor-less dixoygenases[63]. Finally, a general base mechanism for the activation of water rather than the catalytic Serine has been forwarded for the MCP hydrolases[64], as discussed in more detail in section 1.4.4.

1.2.6 Structural aspects of the MCP hydrolases

The MCP hydrolases possess an α-helical lid domain (residues 146-212, $BphD_{LB400}$ numbering) inserted between β6 and α9 of the α/β-hydrolase core (residues 1-145 and 213-286). The active site occurs at the interface of the two domains, and additional MCP hydrolase-specific residues are borne by the lid domain. The active site can be divided into two distinct subsites separated by the catalytic triad (Ser112-His265-Asp237) and 'oxyanion hole' residues (Gly42 and Met113; Figure 8A). First, the polar (P-) subsite is formed by five strictly conserved residues that contact the substrate's dienoate moiety: Gly43, Asn51, Asn111, Arg190 and Trp266 ($BphD_{LB400}$ numbering, Figure 8B). Substitution of each of the last three of these residues in MhpC or Arg190 in BphD lead to their implication in substrate binding and catalysis based on the reduction in the observed steady-state kinetic parameters[65]. The second subsite, named the non-polar (NP-) subsite, houses hydrophobic

residues and has been implicated in binding the variable MCP moiety[65,66]. The identities of the residues that form the NP-subsite are not strictly conserved, consistent with their role in determining substrate specificity of distinct enzymes. In $BphD_{LB400}$, Ile153, Leu156, Phe175, Trp216 and Phe239 are involved in binding the substrate's phenyl-moiety.

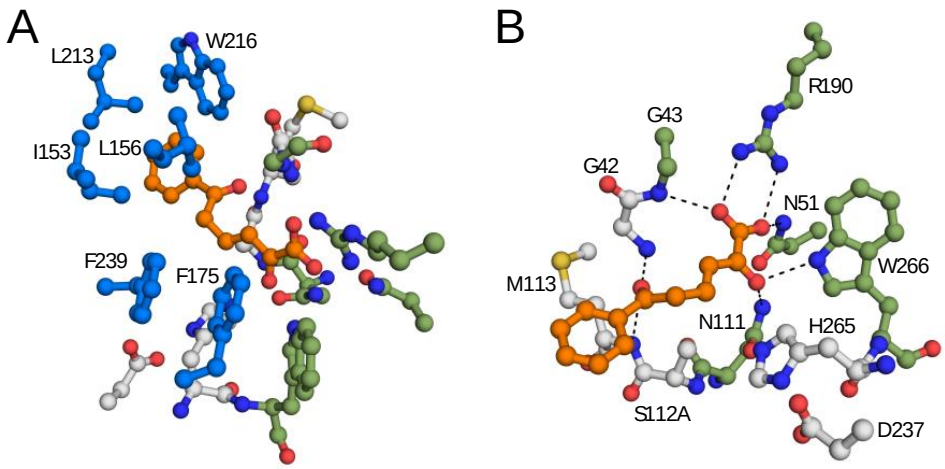

Figure 8. (A) The $BphD_{LB400}$ active site. The P- and NP-subsite residues are coloured green and blue, respectively. The catalytic triad and 'oxyanion hole' residues are shown in white with the catalytic serine substituted for alanine. (B) The conserved MCP hydrolase P-subsite. The conserved enzyme-substrate interactions are illustrated using the $BphD_{LB400}$ S112A:HOPDA binary complex (PDB ID: 2PUH). Dashed lines indicated possible H-bonding (distances $\leq$ 3.4 Å).

1.2.7 Classification of the MCP hydrolases

Phylogenetic analysis based on amino acid sequences represents a powerful starting point for annotation in the post-genomic era. Such analyses can be particularly informative when functional, sequence and structural data are combined. Accordingly, maximum likelihood analyses of a structure-guided sequence alignment revealed at least three subfamilies of MCP hydrolases (named class I to III; Figure 9, [39]). Overall, this classification echoes the known substrate specificities and oligomeric states of the enzymes included in the analysis. Although the substrate specificity reported for class I enzymes is quite broad, all of these enzymes appear to be tetramers. $BphD_{LB400}$ has been reported as a

tetramer in solution[67], while a tetrahedral tetrameric assembly was either inferred or directly observed from the crystal structures of HsaD[68] or MhpC[69]. In contrast, both class II and III enzymes have been reported as dimers[70,71]. The tight clustering of class II enzymes reflects their preference for alkylbenzene-derived MCPs[67,70,72] whereas the preference of class III enzymes is less well-defined but includes carbazole[71]. The grouping of DxnB2 with the class III MCP hydrolases is consistent with the ability of this enzyme to catalyze the hydrolysis of biphenyl metabolites, specifically 9- and 10-substituted HOPDAs, *in vitro*[39]. However, the cognate substrate of DxnB2 is unknown.

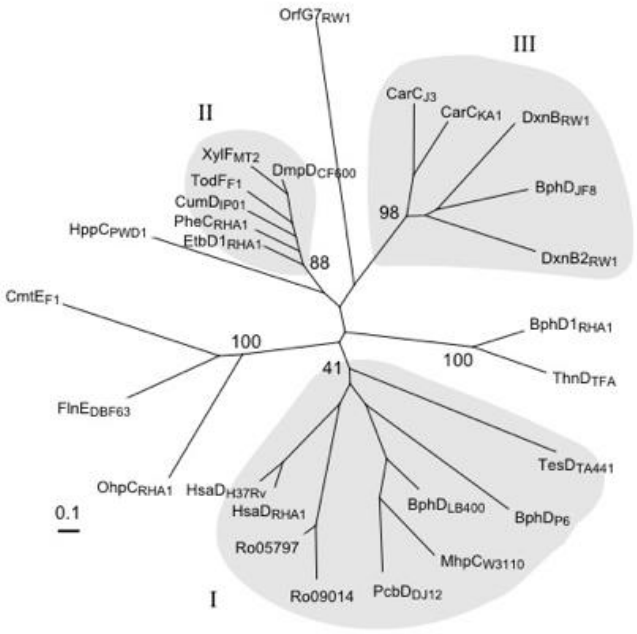

Figure 9. Dendrogram of the best tree obtained from the alignment of 27 MCP hydrolases. The distinct classes and a scale representing the distant of divergence are shown. Numbers at branchpoints represent bootstrap values. Taken from [39].

1.3 Mechanistic aspects of MCP hydrolase catalysis

The MCP hydrolases are interesting due to their purported ability to catalyze both an enol-to-keto substrate tautomerization and hydrolysis of a C-C bond in the absence of organic and inorganic cofactors.

1.3.1 Hydrolysis of carbon-carbon and carbon-heteroatom bonds

The distinct chemical nature of C-X (where X = N, O or S) and C-C bonds has a profound effect on enzyme-catalyzed hydrolysis in Ser-His-Asp triad containing enzymes. Common obstacles to C-X and C-C bond hydrolysis include activation of the scissile bond and a water molecule, which are performed by a general acid and general base, respectively[44,73]. Covalent catalysis is typically employed for these reactions in the α/β-hydrolases (Figure 10). For bond activation, the role of the general acid is fulfilled by the 'oxyanion hole,' which stabilizes two tetrahedral oxyanion intermediates that result from nucleophilic attack at a carbonyl center by the catalytic serine or water, respectively. The catalytic His-Asp pair acts as a general base to facilitate the activation of the serine nucleophile for acylation and water for deacylation. The identity of the atom in the leaving group also contributes greatly to the chemical and kinetic mechanism of bond cleavage. The ability of the catalytic histidine to act as a general acid to protonate the leaving group during the collapse of the first tetrahedral oxyanion intermediate facilitates bond cleavage. In contrast to C-X bond cleavage, a leaving carbon atom is typically non-basic, obviating the aforementioned role of the histidine as an acid and necessitating an alternative electron sink for C-C than for C-X bond cleavage.

MCP hydrolases and at least two other enzyme families that lack a metal cofactor exploit a diketone or diketone-like functionality for C-C bond hydrolysis (Figure 11). First, the serine nucleophile-dependent and independent β-ketolases transform substrates that contain a β-diketone electron sink[74]. A second group of C-C bond hydrolases defined by kynureninase is cofactor-dependent, generating a β-ketiminium moiety by using pyridoxal 5'-phosphate (PLP)[75]. MCP hydrolases are thought to catalyze a substrate enol-to-keto

tautomerization prior to C-C bond cleavage[76]. Common to all these enzymatic reactions is the generation of an electron sink that is capable of stabilizing a leaving carbanion by charge delocalization. In contrast, a mechanistic proposals for orotidine 5'-monophosphate decarboxylase invoke protonation of during[77] or after[78] C-C bond fission.

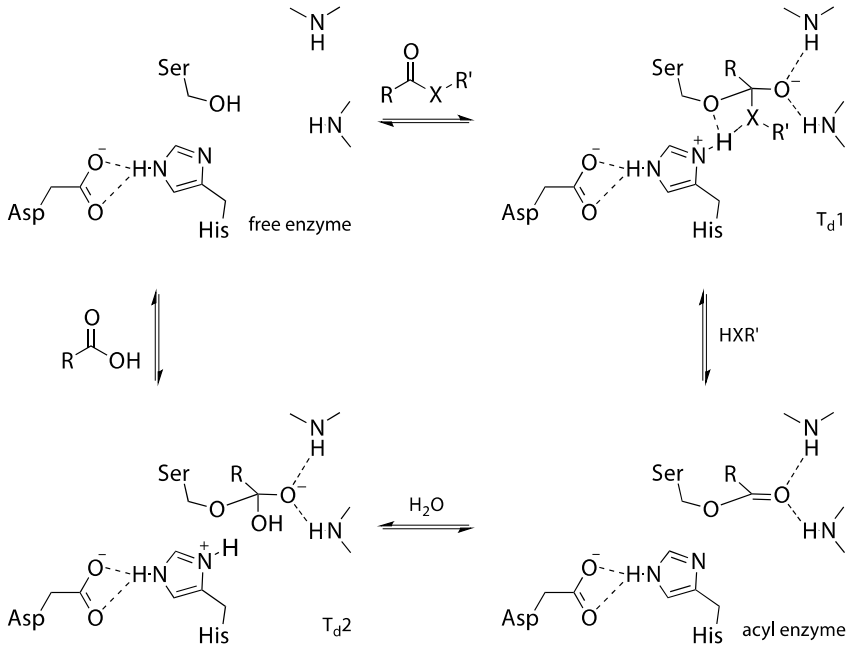

Figure 10. The mechanism of C-X bond hydrolysis in Ser-His-Asp containing α/β-hydrolases. The first (T_d1) and second (T_d2) tetrahedral oxyanion intermediates and acyl-enzyme are drawn. Taken from [79].

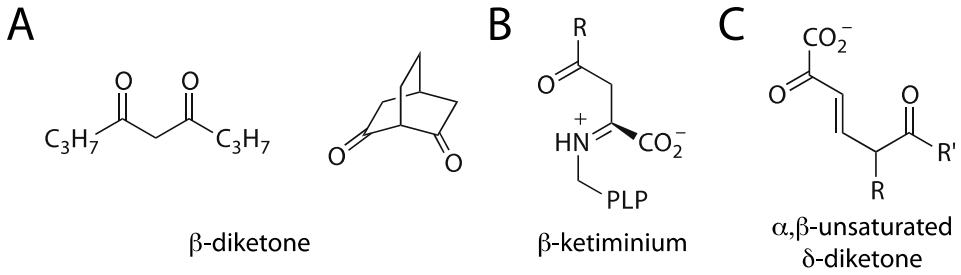

Figure 11. Representative examples of proposed diketone- or diketone-like intermediates during C-C bond hydrolysis by (A) β-ketolases, (B) kynuerninase and (C) the MCP hydrolases.

1.3.2 Substrate ketonization

The mechanism of substrate activation by the MCP hydrolases is poorly understood. The generation of an α,β-unsaturated δ-diketone (Figure 11C) is dependent on protonation of the dienoate moiety at C5. Evidence for an enol-to-keto tautomerization was initially derived from product analyses of reactions performed in $^{2}H_2O$, demonstrating that MhpC catalyzed the stereospecific incorporation of deuterium into the H-5_E position of HPD[80]. This stereospecific deuterium incorporation was confirmed in studies of the $BphD_{LB400}$-mediated hydrolysis of HOPDA[81]. Finally, the ability of $BphD_{LB400}$ to catalyze the tautomerization of HPD to (*E*)-2-oxo-3-pentenoate was also indicative of this prerequisite electron-sink generating enol-to-keto tautomerase activity[66,81].

Although the mechanism is not understood, three residues of the strictly conserved P-subsite have been implicated in substrate binding and/or activation[65]. Notably, the conserved arginine (MhpC Arg188 and $BphD_{LB400}$ Arg190) was ascribed a role in substrate destabilization. Furthermore, a hypothetical role for the catalytic histidine in mediating a proton transfer from an incoming MCP enol, specifically from the C2-hydroxyl to C5, has been forwarded[66,81]. This mechanistic proposal was based largely on two observations. First, the proximity of His265 to the C2-oxo group of the substrate or product in $BphD_{LB400}$ S112A:HOPDA or S112C:HPD binary complexes. Second, BphD H265A and BphD S112A/H265A did not accumulate an intermediate with a bathochromically-shifted spectrum, which is thought to represent a destabilized form of the substrate at the $BphD_{LB400}$ active site (see next section). In spite of the proposal, the protonation state of the substrate as it is bound is not well established. For HOPDA, the p*K*a for the enol:enolate equilibrium (pK_{a2}) is close to physiological pH (see Appendix I for the known chemical properties of MCPs). Moreover,

the visible spectrum of the red-shifted intermediate is also more consistent with an enolate or dianionic species (λ_{max} 434 nm in solution) rather than an enol form of the substrate (λ_{max} 345 nm) arguing against a simple enol-to-keto tautomerization of substrate.

1.3.3 ES^{red}: an unidentified catalytic intermediate

Single turnover kinetic analysis of the $BphD_{LB400}$-catalyzed hydrolysis of HOPDA by stopped-flow revealed the existence of an ES complex with a bathochromically-shifted absorption spectrum (λ_{max} 473 and 492 nm; Figure 12A). The intermediate was named ES^{red}, and its disappearance was mirrored by the production of HPD (Figure 12B), which can be monitored at 270 nm[81]. Subsequent studies revealed that similar red-shifted species with extended lifetimes accumulated in catalytic serine-to-alanine variants of $BphD_{LB400}$ and HsaD, implying that the active site causes substrate destabilization[41,66].

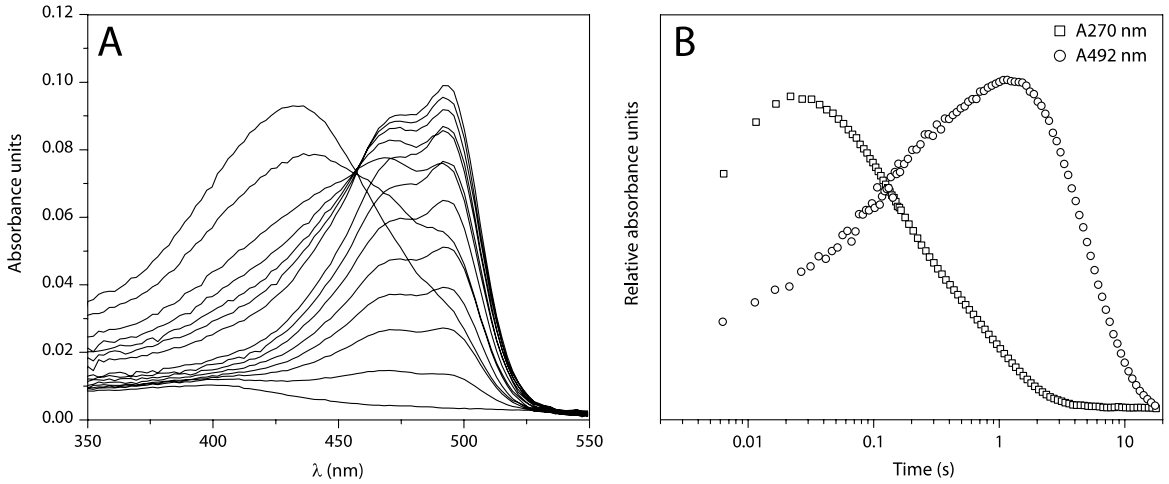

Figure 12. Representative stopped-flow experiment illustrating a single turnover of 4 μM HOPDA by 8.1 μM $BphD_{LB400}$ at 3.2 °C. (A) Changes to the visible spectrum revealing ES^{red}. (B) Data showing that ES^{red} decay (492 nm) is commensurate with HPD production (270 nm). An additional post-catalytic process is visible at 270 nm, HPD ketonization.

Crystallographic characterization of ES complexes in $BphD_{LB400}$ variants with catalytic triad substitutions exposed significantly different HOPDA binding conformations

(Figure 13). Specifically, restrained refinement of HOPDA to the electron density in a 1.6 Å resolution structure of $BphD_{LB400}$ S112A revealed a non-planar binding mode that included a *gauche+* torsion angle around the C4-C5 bond[66]. Single crystal absorption spectra were used to correlate the crystallographic data to the aqueous form of ES^{red}, and therefore, the binding mode was considered to represent a mimic of the catalytic intermediate. The large deviation of the torsion angle around the C4-C5 bond from planarity, resulted in the HOPDA molecule being modeled as a (*E*)-2,6-dioxo-6-phenylhexa-3-enoate. Similar deviations from planarity were also observed in crystalline HsaD S114A:MCP complexes[68]. In contrast to the S112A variants, the binary $BphD_{LB400}$ S112A/H265A:HOPDA complex revealed a binding mode in which C1 through C6 of the dienoate moiety were coplanar. This result was consistent with the lack of spectral perturbation observed in solution and the assignment of the free substrate in acetone in the *trans-transoid* configuration[37,82].

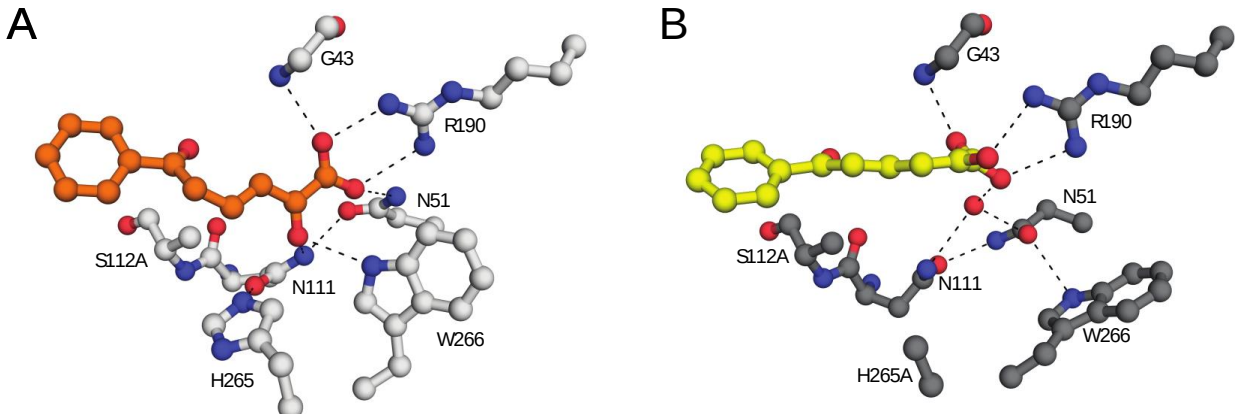

Figure 13. Ball-and-stick diagrams of the $BphD_{LB400}$ variant:HOPDA binary complexes highlighting the differences in binding conformation and P-subsite interactions. (A) $BphD_{LB400}$ S112A:HOPDA (PDB ID: 2PUH) and (B) $BphD_{LB400}$ S112A/H265A:HOPDA (PDB ID: 2PUJ). Polar interactions (≤ 3.4 Å) are indicated using dashed lines.

The crystalline models imply that the catalytic serine variants are capable of substrate activation: generation of the 2,6-diketo intermediate. Thus, the structural data are apparently consistent with the observation that $BphD_{LB400}$ S112A but not H265A is capable of

catalyzing the ketonization of HPD, albeit at approximately 18% of the WT activity[66]. However, the models are contradictory to Woodward's rules, which dictate that the α,β-unsaturated δ-diketone should possess a hypsochromically-shifted spectra relative to the HOPDA enolate dianion. Moreover, ES^{red} formation occurs at essentially an equal rate in $BphD_{LB400}$ WT and S112A[66]. Accordingly, double bond strain has been suggested as a source of the spectral perturbation[83]. In this proposal, a reduction, but not complete disruption, of the *p*-orbital overlap would raise the ground state energy of the substrate thereby lowering the energy of the visible electronic transition. A second hypothesis that is concurrent with the crystalline models, suggests that polarization of π-electrons in the ketonized substrate could also account for the spectral change. Polarization of similar α/β-unsaturated systems in liver alcohol dehydrogenase and enoyl-CoA hydratase explained a 60 and 90 nm red-shift, respectively[84,85]. Despite these proposals, the identity of ES^{red} remains unknown in the MCP hydrolases.

1.3.4 The importance of ES^{red} and molecular basis of inhibition by PCB metabolites

The mechanism of inhibition by 3-Cl HOPDA has been studied extensively in $BphD_{LB400}$ using both kinetic and biophysical approaches. Steady-state kinetic studies revealed that 3-Cl HOPDA is a competitive inhibitor of HOPDA hydrolysis (K_{ic} = 0.57 μM), and that it is ultimately hydrolyzed 470 to 730 times slower than HOPDA[37,86]. The crystal structures of the catalytically inactive $BphD_{LB400}$ S112A variant in complex with HOPDA and 3-Cl HOPDA also revealed major differences in the substrate-binding modes[86]. Instead of the non-planar conformation observed for HOPDA, the 3-Cl HOPDA molecule was bound in a planar conformation that was reminiscent but distinct from the planar binding mode of HOPDA to the S112A/H265A variant. For 3-Cl HOPDA, stabilization of a planar

binding mode was attributed to specific interactions between the chlorine substituent and the side chains of Leu156, Phe175, Phe239 and Met171. These residues form a hydrophobic pocket that accommodates the chlorine substituent (Figure 14). Additionally, unlike all other MCP hydrolase:MCP structures, the carboxylate of 3-Cl HOPDA does not interact with Arg190. Further comparison of available structural data implied that conformational changes would be required to alleviate the observed steric inhibition and reach the productive non-planar binding mode observed for HOPDA.

Much like the $BphD_{LB400}$ H265A variants, ES^{red} was not observed during the hydrolysis of 3-Cl HOPDA and a similar species did not accumulate in complex with $BphD_{LB400}$ S112A in solution[86]. Steady-state kinetic analyses showed that $BphD_{LB400}$ preferentially hydrolyzed a series of 3-substituted HOPDAs in the order H > F > Cl > CH_3. Stopped-flow studies monitoring the single turnover of 3,10-diF HOPDA by $BphD_{LB400}$ revealed a small population of ES^{red}, reinforcing the importance of this intermediate to catalysis. Taken together, the structural and kinetic data suggest that large C3-substituents impede formation of ES^{red}, which can ultimately become rate-limiting to catalysis in the case of 3-Cl HOPDA hydrolysis by $BphD_{LB400}$.

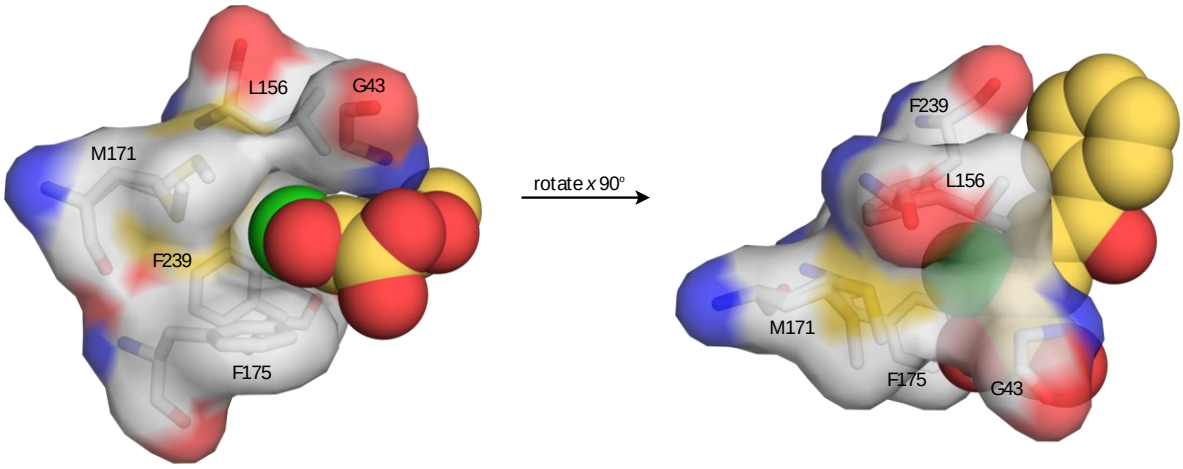

Figure 14. Surface representation of the 3-Cl HOPDA binding mode to $BphD_{LB400}$ S112A. The hydrophobic pocket that accommodates the chlorine substituent is shown (PDB ID: 2RHT).

1.3.5 The hydrolytic reaction

The bulk of the mechanistic studies on the MCP hydrolases have attempted to define the mechanism of the hydrolytic reaction. Despite the wealth of data spanning two decades, no experimental evidence has been reported that satisfactorily delineates the catalytic mechanism of the MCP hydrolases. In fact, both a general base and a nucleophilic mechanism have been proposed (Figure 15), with the former having gained the greatest favour in the literature[87].

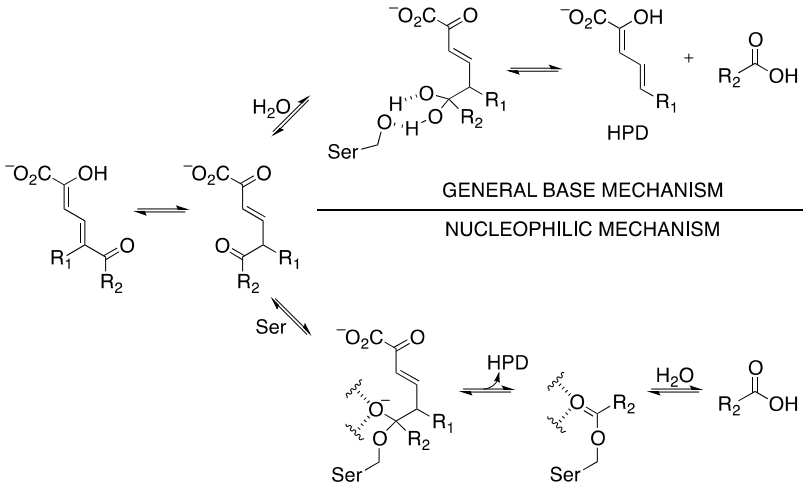

Figure 15. Proposed mechanisms for the MCP hydrolases.

Early work on the MCP hydrolase XylF from *Pseudomonase putida,* which cleaves 2-hydroxymuconic semialdehyde, revealed a chemical inactivation profile resembling that of a typical serine hydrolases[72]. In spite of these experiments, there have been several failed attempts to trap an acyl-enzyme intermediate in MhpC, stimulating support for a general base mechanism of catalysis in the MCP hydrolases[64,83]. Two observations have propelled support for the general base mechanism[64]: (i) a second ^{18}O incorporation event into 3-6% of the succinate product of MhpC-catalyzed hydrolysis of 2-hydroxy-6-oxo-nona-2,4-dienoic acid in $H_2{}^{18}O$, and (ii) an enzyme-catalyzed isotope exchange at the carbonyl of a non-hydrolyzable substrate analog. These data were interpreted as evidence for the reversible formation of a *gem*-diolate intermediate (Figure 16). Precedence for the purported *gem*-diolate was derived from studies on HIV-1 protease, an aspartic protease that utilizes a general base mechanism[88].

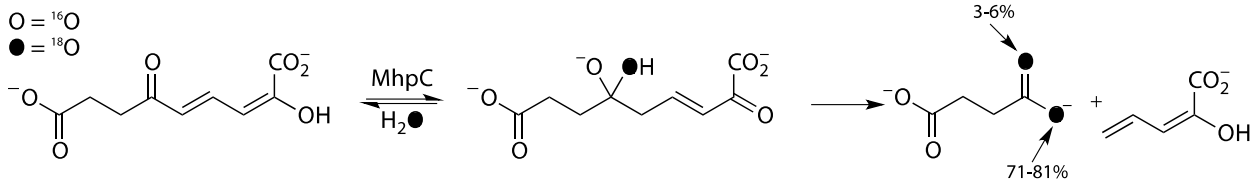

Figure 16. Mechanistic interpretation from studies of MhpC hydrolysis in $H_2{}^{18}O$.

The observation of a ^{13}C NMR signal with a chemical shift that matched a calculated value for a *gem*-diolate species that was hydrogen bonded to a serine residue has been reported as an empirical demonstration of the intermediate and an alternative catalytic role for the catalytic serine[89]. More specifically, a broad signal at 128 ppm was detected during steady-state turnover of (1E:10S) of [^{13}C6]-HOPDA by three variant enzymes, $BphD_{LB400}$ S112A and H265A as well as by MhpC H114A (Figure 17A). These catalytically impaired $BphD_{LB400}$ variants were used to ostensibly increase the likelihood of observing catalytic

intermediates. The MhpC H114A substitution affords the slow turnover of HOPDA by MhpC, a reaction that is not catalyzed by the WT enzyme.

Structural characterization of crystalline HsaD S114A:MCP complexes were also used to strengthen the support for a general base mechanism in the MCP hydrolases. In particular, a conserved active site water molecule was designated as the nucleophilic water. The basis of this assignment were angles measured between the bound MCP carbonyls and the water molecule, which deviated from 10 to 20° from the Bürgi-Dunitz angle of attack on a carbonyl center[41]. Nevertheless, the alleged nucleophilic water was > 5 Å away from the catalytic histidine, and was at hydrogen bonding distances to an asparagine side chain and a ketone group on the substrate, ultimately raising questions about the possible mechanism of nucleophile activation.

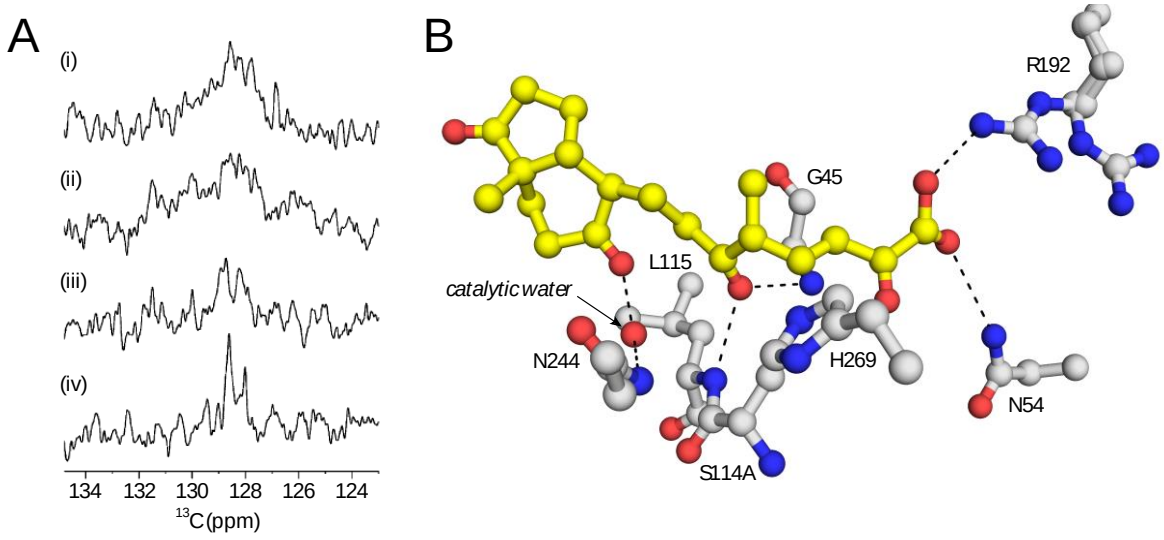

Figure 17. (A) ^{13}C NMR spectra of the putative *gem*-diolate intermediate observed using either (i) $BphD_{LB400}$ H265A, (ii) $BphD_{LB400}$ S112A, (iii) MhpC H114A or (iv) the spectrum of the substrate free in solution. Taken from [89]. (B) Proposed catalytic water in the binary complex of HsaD S114A:4,9 DHSA (a cholesterol-derived metabolite, PDB ID: 2WUF).

Finally, more indirect evidence for a general base mechanism was founded on a Hammett analysis of the $BphD_{LB400}$-catlayzed hydrolysis of *para*-substituted HOPDAs revealing a negative correlation, $\rho = -0.71$, between electron withdrawing *para*-substituents

and k_{cat}[90,91]. This interpretation was largely based on the contrast between these results and the positive correlation observed in serine proteases[92]. Interestingly, Hammett analysis of $BphD_{LB400}$ esterase activity using *p*-substituted *p*-nitrophenyl benzoates was also interpreted as evidence for a general base mechanism[93]. For the *p*-substituted *p*NPBs, the Hammet plot was non-linear, a feature that was attributed to a change in the rate-limiting step from ester bond cleavage to product release for substrates with $\sigma \geq 0$. While this interpretation was ambiguous, the failure to observe a pre-steady-state kinetic burst of product formation from pNPB was cited to strengthen the proposal of a general base mechanism for the MCP hydrolase *in vitro* esterase activity.

1.3.6 Half-site reactivity

Half-site reactivity can be classified as an extreme case of negative cooperativity in which the maximal yield of product formation from a single enzymatic turnover amounts to only half of the apparently equivalent active sites[94]. Differences in substrate binding between protomers in higher order quaternary structures or structural non-equivalence attributed to oligomeric subunit organization are among the explanations for this phenomenon. In the MCP hydrolases, half-site reactivity was first proposed based on half-site occupancy of a crystalline MhpC:inhibitor complex[69]. Similar observations have been reported for two HsaD S114A:MCP complexes. Nevertheless, determination of dissociation constants to the S114A variant suggested stoichiometric binding in solution[41]. Unfortunately, crystallographic symmetry of all $BphD_{LB400}$:MCP complexes requires equivalence across all active sites, limiting comparisons of active site occupancy as in MhpC and HsaD[66,81,86]. In $BphD_{LB400}$, half-site reactivity could account for the biphasic decay of ES^{red} during a single turnover of HOPDA[81]. A two-conformation model of catalysis was

initially proposed based on the mirrored kinetic data correlating ES^{red} decay to product formation (Figure 18). In contrast to the paradigm, the relatively large amplitudes associated with both transient kinetic phases at 492 and 270 nm contradict the proposal of reversible (3-6%) *gem*-diolate formation. Instead, the two-conformation model suggests that the MCP hydrolases utilize a nucleophilic mechanism of catalysis in which deacylation at one site is linked to acylation at another.

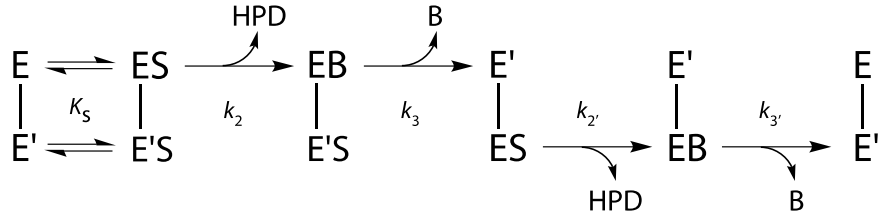

Figure 18. The two-conformation model of catalysis for $BphD_{LB400}$.

1.4.5 Summary of mechanistic studies on the MCP hydrolases

Overall, the balance of the data collected using $BphD_{LB400}$, MhpC and HsaD has been used to challenge the accepted paradigm for serine hydrolases. A general base mechanism is not outside of the scope of the α/β-hydrolase superfamily and is consistent with the mechanisms proposed for other C-C hydrolases that act on a diketone functionality. In contrast, the two- conformation model, the geometric arrangement of the 'nucleophile elbow', and the comparative nucleophilic strength of alkoxides versus hydroxides[95,96] raise questions about the reported mechanism. Accordingly, the chemical mechanism of the MCP hydrolases has not been definitively established and mechanistic studies have been focused only on class I enzymes.

1.4 Aim of this study

Overall, the goal of this thesis was to investigate the kinetic and chemical mechanism of the MCP hydrolases. At the outset of these studies, a general base mechanism of catalysis

had been proposed as the paradigm for the MCP hydrolases[87]. Thus, the first goal of this work was to establish the hydrolytic mechanism of this enzyme family. Stopped-flow and chemical quench experiments followed by mass spectrometry were employed to directly detect catalytically relevant reaction intermediates. Both $BphD_{LB400}$ WT and an H265Q variant were analyzed, and the crystal structures resulting from HOPDA soaking experiments in the H265Q and S112A/H265Q variants are included in the interpretation of the results. These experiments were complemented with indirect studies, which included product analyses of reactions in $H_2{}^{18}O$ by EI GC/MS and solvent partitioning experiments by HPLC.

The second objective of the study was to determine the mechanism of ester hydrolysis by the MCP hydrolases. Stopped-flow was utilized to perform pre-steady-state kinetic analysis of the $BphD_{LB400}$ WT and variant-mediated hydrolysis of pNPB. Nucleophile partitioning experiments were also used to compare the C-O and C-C bond cleavage reactions.

The third goal of this thesis was to investigate the poorly understood mechanism of substrate ketonization. For these studies, DxnB2 from *S. witichii* RW1 was used based on the relatively simple kinetic behaviour observed during preliminary pre-steady-state characterization, namely stoichiometric turnover of HOPDA rather than the half-site reactivity observed for $BphD_{LB400}$. Again, stopped-flow was employed to investigate the mechanism of ketonization by monitoring the single turnover of a series of substituted HOPDAs and performing an extended Brønsted analysis thereof. Solvent viscosity and isotope effects were also measured in order to substantiate and provide additional evidence for the assignment of observable transient kinetic phases. ^{19}F NMR spectra of free and bound

fluorinated substrates were also recorded in order to attempt to assign the electronic nature of ES^{red}.

Next, the role of the catalytic histidine and two conserved P-subsite residues in substrate binding, destabilization and ketonization were assessed. DxnB2 Asn43, Arg180 and His256 variants were prepared and studied using steady- and transient-state kinetic approaches in order to assess their ability to accumulate ES^{red} during the hydrolysis of HOPDA and 9-Cl HOPDA.

The final goal of this work was to investigate the reactivity of DxnB2 towards recalcitrant 3-Cl HOPDAs, which is higher than previously characterized BphD enzymes. Single turnover studies by stopped-flow were performed in order to assess the rate-limiting step for the turnover of 3-Cl HOPDA, a model PCB metabolite, and 3,9,11 tri-Cl HOPDA, a metabolite that can be found in nature. A structural comparison of DxnB2 and other MCP hydrolases was also conducted in order to identify potential determinants in catalysis. The crystal structures of the DxnB2 S105A: binary complexes are included in the discussion of these results.

Chapter 2: MATERIALS AND METHODS

2.1 Chemicals

2.1.1 Sourced reagents

Chlorinated DHBs, including 4-Cl-DHB, 6-Cl-DHB, 2'-Cl-DHB and 3'-Cl-DHB were gifts from Victor Snieckus (Department of Chemistry, Queen's University, Kingston, ON). All other chemicals were of analytical grade and used without further purification unless stated otherwise. Preparations of $BphAE_{LB400}$, $BphF_{LB400}$ and BphG from *Pandoraea pnomenusa* B-356 ($BphG_{B356}$) were purified by Leticia Gómez-Gil according to published protocols[16,22,97]. An *E. coli* OverExpress C41(DE3) strain harbouring a pET14b vector carrying *bph*B_{B356} was provided for protein production by Michel Sylvestre (INRS – Institut Armand Frappier, Point-Claire, QC). His_6-$BphB_{356}$ was purified as previously described[98] except that glycerol was omitted from the purification buffers.

2.1.2 Preparation of 8-F and 5,8-diF DHB

2'-F- and 2',6-diF-DHB was generated from whole cell biotransformation of 2,2'-difluorobiphenyl using *P. pnomenusa* B-356 in the presence of 3-chlorocatechol. A 1 L culture of *P. pnomenusa* B-356 was grown on M9[99] + Goodies[100] supplemented with 100 mg biphenyl was grown until an $OD_{600\ nm}$ of 0.5. These cells were then harvested and washed three times with phosphate buffer saline (PBS, pH 7.3) in an attempt to remove residual biphenyl. The harvested cells were divided into two flasks containing 500 mL PBS + 8 mg 2,2'-diF-biphenyl + 8 mg 3-chlorocatechol, an inhibitor of BphC. These flasks were then incubated at 30 °C for 90 minutes, shaking at 200 rpm. The two samples were then pooled, acidified to pH 2.5, centrifuged and the supernatant was filtered to remove any insoluble 2,2'-difluorobiphenyl. The filtrate was extracted with three 200 mL volumes of

ethyl acetate, dried with $MgSO_4$, and concentrated by rotary evaporation. Dry samples from each biotransformation were stored under nitrogen gas in an Mbraun Labmaster glovebox (Stratham, NH, USA) until further purification.

A Waters 2695 HPLC system (Waters Corp., Milford, MA) was used for the purification of DHBs. The dry samples were dissolved in a solution of 0.5% formic acid (v/v), 50% methanol (v/v). Precipitate was removed from the resuspension by centrifugation and filtration (0.45 μm).. The mixtures were injected on to a 250 x 10 mm Luna 5 μm C18(2) column (Phenomenex, Torrence, CA), equilibrated at a 50:50 ratio of solvent A and B, and operating at a flow rate of 3.5 mL/min. Solvent A was 0.5% formic acid (v/v) and solvent B was methanol. Isocratic elution of 2'-F- and 2',6-diF-DHB was achieved after 27.4 and 25.5 minutes, respectively. Pure fractions were collected, pooled, and partially dried under a stream of N_2 gas to remove excess methanol. The identity of each DHB was confirmed by performing EI GC/MS. Each resulting fluorinated DHB solution, which typically amounted to 10 mL post-purification, was diluted to 200 mL and the pH of the solution was adjusted to 7.5 with 1 M NaOH prior to HOPDA preparation.

2.1.3 Preparation of ^{13}C-DHB

Uniformly labeled ^{13}C-DHB was prepared from the enzymatic transformation of ^{13}C-biphenyl (Sigma). A 40 mL reaction mixture containing 5 mg $BphAE_{LB400}$, 9 mg His_6-$BphF_{LB400}$, 10 mg $BphG_{B356}$, 20 mg His_6-$BphB_{356}$, and 190 μM NADH in KPi (I = 0.05 M), pH 7.5, was used to generate ^{13}C-DHB. The reaction was complete in 1 hour at room temperature with constant stirring. The solution was then passed through a 0.45 μm filter, acidified to pH 2.5 with HCl, extracted with three 20 mL volumes of ethyl acetate, dried with

$MgSO_4$, and concentrated by rotary evaporation. The ^{13}C-DHB, R_t = 32 min, was purified by HPLC, as described for the fluorinated DHBs.

2.1.4 Preparation of HOPDAs

HOPDAs were generated enzymatically using recombinantly expressed and purified BphC from *B. xenovorans* LB400 and the appropriate DHB as previously described[37]. Briefly, ~20 mg of DHB was solubilized in 1 mL of ethanol and added to a 500 mL volume of potassium phosphate buffer (I = 0.1 M), pH 7.5 containing 1 to 2 mg of BphC. For the fluorinated DHBs, 2 to 4 mg were transformed in a 200 mL volume. Quantitative conversion was monitored spectrophotometrically by following the increase in absorbance at the λ_{max} specific to HOPDA enolate dianion that was being generated (see Appendix I). Upon complete conversion, the HOPDA solution was acidified to pH 2.5 using HCl and extracted with three 0.4 volumes of ethyl acetate. The organic extract was then dried over anhydrous $MgSO_4$, concentrated by rotary evaporation, and ultimately dried using a stream of nitrogen gas. The purity of each sample was inspected by HPLC before use. The pK_a of 5,8-diF HOPDA was determined to be 5.0 ± 0.2 by titration of an unbuffered solution, as previously described[37].

2.2 Mutagenesis, protein production and purification

2.2.1 Production and purification of $BphD_{LB400}$

The yield from the purification of recombinant $BphD_{LB400}$ was improved two-fold by using *E. coli* Rosetta(DE3)pLysS cells (EMD4Biosciences) as a host strain at 30 °C. Otherwise, $BphD_{LB400}$ was purified as previously described[101].

2.2.2 Mutagenesis of DxnB2

$BphD_{LB400}$ and DxnB2 were mutated using a modified Quikchange oligonucleotide-

directed mutagenesis method (Stratagene, La Jolla, CA). Briefly, a single, 5'-phosphorylated mutagenic primer was used to amplify the plasmids encoding each gene. For $BphD_{LB400}$, a broad host range plasmid, pSS184, carrying either *bphD* or *bphD* S112A was used as a template with the following primer, 5'-PO_4-CTCCAAGTGCGGC*CAG*TGGGCGCAATGG, affording a His to Gln codon substitution. For DxnB2, the pEMBL18-based plasmids, pEMDXN1 carrying the wild type sequence or pEMDXN105A carrying a codon substitution for the S105A variant were used as templates. A complete list of mutagenic DxnB2 primers can be found in Table 1. After amplification, the PCR template was digested with DpnI, and the single stranded mutated amplicons were transformed and propagated in NovaBlue cells (EMD4Biosciences). The nucleotide sequences of plasmids carrying the mutated genes were confirmed using an ABI 373 Stretch DNA sequencer (Applied Biosystems, Foster City, CA) and a BigDye v3.1 Terminator kit.

Table 1. List of primers used for the mutagenesis of DxnB2

Mutants	Primer sequence
N43A	GGCCGGTCC*GCC*TTCGCCGACAATTTTCCG
N43D	GGCCGGTCC*GAC*TTCGCCGACAATTTTCCG
N43H	GGCCGGTCC*CAC*TTCGCCGACAATTTTCCG
S105A	CCTGATCGGCAAC*GCC*ATGGGCGGGACG
R180K	GATATCGTCCATTAC*AAG*CACGAGGCGTCGCTG
R180M	GATATCGTCCATTAC*ATG*CACGAGGCGTCGCTG
R180Q	GATATCGTCCATTAC*CAG*CACGAGGCGTCGCTG
H255A	CCGAACTGCGGC*GCT*TGGGTGATGATCGAA
H255E	CCGAACTGCGGC*GAA*TGGGTGATGATCGAA
H255Q	CCGAACTGCGGC*CAG*TGGGTGATGATCGAA

2.2.3 Production and purification of DxnB2

DxnB2 was produced in *E. coli* DH5α, as previously described, but purified using a modified version of the published protocol[39]. Buffers were made using water with a

conductivity of > 17 MΩ purified from a Barnstead NANOpure UV apparatus (Barnsted International, Dubuque, IA). Buffer A was 20 mM HEPES, pH 7.5 and Buffer B was 20 mM HEPES, 500 mM NaCl, pH 7.5.

Typically, a cell pellet obtained from 2 litres of culture (~8 g, wet weight) was resuspended to a final volume of 40 mL in Buffer A supplemented with 1 mM $CaCl_2$, 1 mM $MgCl_2$, and 1 mg DNase I (Roche Diagnostics, Laval, QC). The cells were lysed by three successive passages through an Emulsi Flex-C5 homogenizer (Avestin Inc, Ottawa, ON) operating between 10 and 15 kPSI. Cell debris was removed by ultracentrifugation at 50000*g* for 45 min at 4 °C. The resulting supernatant was passed through a 0.45 μm filter before being loaded onto a 28 mL bed volume anion exchange Source 15Q column (GE Healthcare), which was equilibrated at 7% Buffer B and operating at 15 mL/min using an Akta Explorer or Purifier 100 (GE Healthcare). Proteins were eluted using a linear gradient from 7 to 40% B over 15 column volumes. Fractions containing DxnB2, which centered near 130 mM NaCl, were pooled and concentrated using an Amicon stirred cell concentrator fitted with an YM30 membrane (Millipore, Billerica, MA). The concentrated sample was then brought to 1 M $(NH_4)_2SO_4$ at pH 7.5 and stirred for 12 hours at 4 °C. The resulting precipitate was washed with three 25 mL volumes of Buffer A supplemented with 1 M $(NH_4)_2SO_4$ before dissolution in 20 mM TAPS, pH 8.5. Purified preparations (> 99% homogeneity based on SDS-PAGE) were then exchanged into potassium phosphate buffer (KPi; I = 0.1 M), pH 7.5, concentrated to > 20 mg/mL, flash frozen in liquid nitrogen, and stored at -80 °C until further use. The yield obtained from each purification was ~80 mg/L.

The purification scheme for DxnB2 S105A/H255E differed from the protocol outlined above since this variant was produced at lower levels and was recalcitrant to the

standard ammonium sulfate precipitation procedure. Instead, enriched DxnB2 S105A/H255E samples (post-Source 15Q) were brought to 1 M $(NH_4)_2SO_4$, 20 M HEPES, pH 7.5, filtered, and loaded onto a 28 mL bed volume Source 15PHE column (GE Healthcare) for separation based primarily on hydrophobicity. The column was equilibrated with 1 M $(NH_4)_2SO_4$, 20 M HEPES, pH 7.5 and was operated at 15 mL/min. Proteins were eluted using a gradient from 1 to 0 M $(NH_4)_2SO_4$, in 20 mM HEPES, pH 7.5 over 30 column volumes. DxnB2 eluted near 60 mM $(NH_4)_2SO_4$. The purified DxnB2 S105A/H255E enzyme was then buffer exchanged, concentrated, frozen and stored as described above.

2.2.4 Protein Analysis

The concentration of purified enzyme was routinely determined using spectrophotometric analysis of samples prior to all experimentation using the molar absorptivity of $BphD_{LB400}$, $\varepsilon_{280\ nm} = 55.4\ mM^{-1}cm^{-1}$[81], and DxnB2, $\varepsilon_{280\ nm} = 36.2\ mM^{-1}cm^{-1}$. These values were calculated from the absorbance at 280 nm of samples whose concentrations had been determined by amino acid analysis at the Advanced Protein Technology Centre of the Hospital for Sick Children (Toronto, ON, Canada). It was assumed that single or double amino acid substitutions did not significantly perturb the absorptivity of the enzymes.

2.2.5 Size Exclusion Chromatography Multi-angle Light Scattering (SEC-MALS).

SEC-MALS experiments were performed using an AKTA Purifier (GE Healthcare) fitted with Wyatt Technology Corporation SEC column and guard column (WTC-030S5 and WTC-030S5G). The protein concentrations used were between 1.5 and 2.5 mg/ml, prepared in 20 mM HEPES, pH 7.5. Multi-angle light scattering and refractive index was measured using the miniDAWN TREOS and Optilab T-rEX detectors (Wyatt Technology Corporation,

Santa Barbara, CA). Calibration was performed using bovine serum albumin.

2.3 Steady-state kinetic experiments

2.3.1 Standard spectrophotometric assay

A Cary60 or Cary5000 spectrophotometer equipped with a thermostatted cuvette holder (Agilent Technologies Canada Inc., Mississauga, ON) was utilized to monitor the generation or hydrolysis of HOPDAs. DHB ring-cleavage by BphC was followed by monitoring an increase in absorbance at the appropriate wavelength corresponding to the λ_{max} of the HOPDA enolate chromophore (Appendix I). The hydro- or alcoholytic activity of $BphD_{LB400}$ and DxnB2 were measured by monitoring the decay in the absorbance attributed to the HOPDA enolate chromophore. Alternatively esterase activity was monitored at 400 nm, following the appearance of *para*-nitrophenyl (pNP) from the cleavage of *para*-nitrophenyl benzoate (pNPB). Unless otherwise noted, kinetic measurements were performed in KPi (I = 0.1 M), pH 7.5, and the reaction systems were maintained at 25.0 ± 0.5 °C. All reactions were initiated by the addition of a 10 μL aliquot of enzyme prepared at an appropriate concentration. The reaction progress curves were deemed to be linear for at least 1 minute by fitting a series of 12 s intervals without the observation of significant (> 10%) decay in the measured initial rate. For higher concentrations of HOPDAs equal to or exceeding 50 μM, a 2 mm pathlength cuvette was employed. Initial velocities (v_0) were determined from the slopes of the linear progress curves using the regression tool within the Cary WinUV Kinetics application. The Michaelis-Menten equation or one accounting for substrate inhibition was fit to the data using the dynamic least squares fitting option in LEONORA[102].

2.3.2 Enzyme-substrate complex formation

Unless otherwise indicated, enzyme-substrate (ES) complexes were formed by mixing 40 μM DxnB2 S105A with 10 μM HOPDA in KPi (I = 0.1 M), pH 7.5 at 25.0 ± 0.5 °C. Electronic absorption spectra of the substrates alone or in complex were recorded using the Scan application of a Cary5000 spectrophotometer.

2.3.2.1 Determination of dissociation constants

Dissociation constants for DxnB2 S105A P-subsite:substrate complexes were determined by measuring concentration dependent changes to the visible spectra of HOPDAs in KPi (I = 0.1 M), pH 7.5 at 25.0 ± 0.5 °C. Specifically, 4 μM HOPDA or 3 μM 9-Cl HOPDA was titrated with a concentrated solution of enzyme. Titrations into 400 μL of the substrate did not exceed 2% (v/v). The dissociation constants were then evaluated by fitting either a quadratic or hyperbolic binding equation to the data using the non-linear curve fitting were conducted in *R*[103].

2.4 Transient-state kinetic experiments

2.4.1 Standard protocol for stopped-flow kinetic experiments

An SX.18MV stopped-flow reaction analyzer (Applied Photophysics Ltd., Leatherhead, UK) was used to perform transient-state kinetic measurements. The temperature of the optical cell and drive syringe chamber was maintained at 25 °C using a circulating water. The concentration of reactants and specific buffer conditions are stated in the Results section as they depended on the aim of each individual experiment. Multiple wavelength data from 180 to 750 nm were collected using the system's photodiode array (PDA) detector directly coupled to the Xe light source (the practical range was from 250 nm to 750 nm). The settings for the PDA detector were set manually as follows: integration period 1.0 ms, scan

period 0.921 ms, offset 0.1 V, gain 153. A monochromator (4.96 nm/mm bandpass open to 0.5 mm; ~2.5 nm bandpass) was employed to collect single wavelength data. Rate constants from stopped-flow experiments are reported using distinct nomenclature: (i) *k* when the process has been unambiguously assigned or (ii) $1/\tau$ (reciprocal relaxation time) when the assignment of processes were provisional or supported by this work alone.

2.4.2 Rapid-quench methods

Acyl-enzymes were prepared using the sequential mixing option of an SX.18MV stopped-flow reaction analyzer. The temperature of the drive syringe chamber and optical cell were held at 25 °C by a circulating water bath. Samples analyzed by mass spectrometry originated from reactions of 4 μM enzyme and 20 μM HOPDA or 9-Cl HOPDA in KPi (*I* = 0.1 M), pH 7.5 before quenching with acetic acid (5% final v/v). The system was manually calibrated so that each quenched reaction volume totaled 400 μL: 220 μL of the reaction mixture was quenched with 180 μL of 11.1% acetic acid (v/v) originating from a second set of stopped-flow syringes. Quenched samples, which originated from approximately 10-15 shots from the stopped-flow syringes (4 to 6 mL total volume), were collected on ice, measured to be at pH 2.3, and then concentrated 10-fold at 4 °C. Samples were either flash frozen in liquid N_2 and stored at -20 °C until whole protein LC ESI/MS analysis or incubated with 1:50 pepsin (w/w) for 1 h at 37 °C. The digests were halted by flash freezing with liquid N_2, and the resulting peptide mixtures were stored at -20 °C until further analysis.

Samples from the reaction of $BphD_{LB400}$ WT with HOPDA were allowed to age for 0.2, 1 and 10 seconds prior to quenching, while the H265Q variant reaction was quenched after 0.6 seconds. For DxnB2, the reactions with 9-Cl HOPDA were allowed to proceed for 1 second before quenching in the stopped-flow apparatus whereas the reaction with HOPDA

was quenched manually after 10 seconds.

2.5 Mass spectrometry of enzyme samples

Whole protein samples were analyzed using LC ESI-MS. Quenched reaction mixtures were loaded on a C_{18} precolumn (Dionex) and buffer salts were washed from the samples before elution in 80% acetonitrile, 0.1% formic acid (v/v). A Q-TOF hybrid instrument (QSTAR, Pulsar i, Applied Biosystems, Foster City, CA) was used to analyze the eluted samples. Estimates of the amount of modified $BphD_{LB400}$ were based on comparing the observed peak areas calculated from Gaussian peak fitting function in Origin 8.0 (OriginLab Corporation, Northampton, MA).

Pepsin-digested peptides were analyzed by LC ESI MS/MS and identified as previously described[104], except that pepsin specificity was used to limit the MASCOT database search, benzoylated serine residues were allowed as a variable modification, and the fragments were searched against the $BphD_{LB400}$ sequence.

2.6 Product analysis

2.6.1 HPLC analysis of product ratios from nucleophile partitioning

Reactions were analyzed using a Waters 2695 HPLC system (Waters Corp., Milford, MA) equipped with a Hewlett-Packard ODS Hypersil C_{18} column (5 μm pore size, 125 mm × 4 mm) operating at a flow rate of 1 mL min^{-1} and equilibrated at 10% solvent B (methanol) in solvent A (0.5% H_3PO_4 v/v, in H_2O). Reactions were quenched with H_3PO_4 (0.5%, v/v) and mixtures passed through a 0.45 μm filter before injection. Product ratios or percentages of acid product were calculated by measuring the amount of benzoate produced in each reaction relative to controls performed without alcohol. Control reactions in potassium phosphate (I = 0.1 M, pH 7.5) with or without 0.2% acetone (v/v) were considered to be 100% hydrolytic,

and the amount of benzoate was quantified by integrating the eluted peak volume using Empower 3 software (Waters Corp.). All reactions analyzed using HPLC were performed in triplicate: the mean and standard deviation are reported.

Alcoholysis reactions were performed in 400 μL of potassium phosphate (I = 0.1 M) pH 7.5 at 25 ° C containing 40 μM HOPDA and were initiated by adding $BphD_{LB400}$ to a final concentration of 4 nM. The completeness of the reactions was judged spectrophotometrically before quenching. Samples were eluted using the following solvent gradients: (i) 10 to 30% B from 0 to 20 min, (ii) 30 to 60% B from 20 to 30 min, and (iii) 60 to 100% B from 30 to 40 min. Product elution times were as follows: 5.5 min for HPD, 13.7 for benzoate, 25.5 for methyl benzoate, 29.9 for ethyl benzoate, and 32.4 for propyl benzoate. The retention times of the alcoholytic products matched those of purchased standards.

Experiments that aimed to assess the methanol dependence of $BphD_{LB400}$-mediated hydrolysis of HOPDA and pNPB were conducted via elution using similar gradients: (i) 10 to 30% B from 0 to 20 min, (ii) 30 to 60% B from 20 to 30 min, and (iii) 60 to 100% B from 30 to 32 min. Because of the relatively low solubility of the ester, reaction volumes were increased to 1 mL and mixtures contained 4 μM pNPB. Moreover, 500 μL was injected to compensate for the reduced substrate and/or product concentration.

2.6.2 Standard protocol for EI GC/MS analysis

All samples analyzed by EI GC/MS were solubilized in pyridine and derivatized using an equal volume of BSTFA + TMCS (99:1) for at least 10 min. EI GC/MS was carried out using an HP 6890 series GC system fitted with an HP 5973 mass selective detector and an HP 5 ms column (30 m × 250 μm). The operating conditions were: TGC (injector) 280 °C; TMS (ion source) 230 °C; oven program time $T_{0\ min}$ 80 °C, $T_{60\ min}$ 290 °C, $T_{0\ min}$ 80 °C

(heating rate 5 °C min^{-1}).

2.6.2.1 $BphD_{LB400}$-mediated hydrolysis in $H_2{}^{18}O$

For solvent exchange experiments, 20 μM $BphD_{LB400}$ was incubated with 200 μM benzoate for 300 min or used to cleave 200 μM HOPDA over 20 min in 50 μL of KPi (*I* = 0.1 M), pH 7.5, in 92% $H_2{}^{18}O$ (v/v). Benzoate samples were prepared in acetone, applied to microfuge tubes, and allowed to evaporate to dryness before incubation in ^{18}O-buffer with or without enzyme. Quantified samples of HOPDA in KPi (I = 0.1 M), pH 7.5, were lyophilized before resuspension in $H_2{}^{18}O$ with or without enzyme. In some instances, HOPDA was pre-incubated with the ^{18}O-buffer for either 5 or 20 min prior to the addition of enzyme. The enzyme was prepared in natural abundance buffer. This buffer was also added to samples that did not contain enzyme in order to account for the dilution of $H_2{}^{18}O$ to 92% (v/v). After incubation (20 or 300 min), samples were acidified to pH 2.3 with acetic acid (5% final v/v) and extracted with 2 volumes (100 μL) of ethyl acetate. The organic fraction was dried under vacuum.

The average distribution of fragment ions observed in H_2O was used to estimate the amount of ^{18}O incorporation by fitting the data in $H_2{}^{18}O$ to two distinct models accounting for (i) a single ^{18}O incorporation event, and (ii) low level of incorporation of a second ^{18}O equivalent into benzoate. The root-mean-square error is reported for each fit. The relative abundance of fragment ions is reported as the percentage of a single species and the error between two replicated is reported as a standard deviation.

2.7 Characterization of ES^{red}

2.7.1 NMR of DxnB2 S105A complexes

NMR spectra were recorded at 25 °C using either a Bruker Avance 500 or 600 MHz

spectrometer equipped with cryogenic probes. ^{19}F chemical shifts were referenced to a 10% solution of trifluoroacetic acid (TFA). Binary complexes of 400 μM DxnB2 S105A with either 200 μM 8-F or 5,8-diF HOPDA were prepared in KPi (I = 0.1 M), pH 7.5. ^{19}F NMR spectra of standards, including 200 μM 8-F HOPDA, 200 μM 5,8-diF HOPDA, and saturated solutions of 2-fluorophenylpropanone and 2-flourophenylprop-2-eneone in KPi (I = 0.1 M), pH 7.5, were also recorded. ^{1}H ^{13}C HSQC spectra were recorded for ^{13}C-HOPDA and a DxnB2 S105A:^{13}C-HOPDA binary complex (1 mM S105A to 500 μM ^{13}C-HOPDA) in KPi (I = 0.1 M), pH 7.5. For comparison, an HSQC spectrum of 5 mM unlabeled HOPDA in acetone-d_6 was also recorded. The spectra were processed and analyzed using Bruker Topspin 3.0 software.

2.7.2 Sensitivity of ES^{red} to molecular oxygen

The half-life ($t_{1/2}$) of the ES^{red} species resulting from the DxnB2 S105A:HOPDA binary complex was measured spectrophotometrically at 25 °C in KPi (I = 0.1 M), pH 7.5 at each of three concentrations of O_2. First, a sample was prepared under ambient conditions, 280 μM. Second, a solution was prepared at 650 μM O_2 by bubbling oxygen into a pre-formed solution of ES^{red}. For the samples containing excess O_2, the concentration dissolved into each system was measured using a Clark-type Oxygen electrode (Hansatech Instrument Ltd., Norfolk, UK). Finally, oxygen-free samples were prepared using degassed buffers that were equilibrated in an Mbraun Labmaster glovebox operating at < 5 ppm O_2. Each 1 mL sample was sealed in a screw cap cuvette topped with a silicone rubber septum. Visible spectra were recorded at 5-20 minute intervals, and a $t_{1/2}$ for each sample was determined by fitting a single exponential decay to the data using Origin 8.0.

Product analysis of ES^{red} samples were performed by comparing the DxnB2

S105A:9-Cl HOPDA decay products to those from the non-enzymatic process. EI GC/MS was performed as described for the ^{18}O-exchange experiments.

2.8 Structural comparison of MCP hydrolases

Superposition of MCP hydrolase structures was performed using the STAMP algorithm implemented in Multiseq, a plugin available in VMD[105-107]. Tools available in COOT[108] were also routinely used for superposition and manual inspection of the aligned proteins. The common names, biological sources and PDB codes of the aligned enzymes are: $BphD_{LB400}$ from *B. xenovorans* LB400 (2OG1, chain A)[81], $BphD_{RHA1}$ from *Rhodococcus jostii* RHA1 (1C4X)[109], CarC from *Janthinobacterium* sp. strain J3 (1J1I)[110], CumD from *Pseudomonas fluorescens* IP01 (1IUP)[70], DxnB2 from *Sphingomonas witichii* RW1 (coordinates provided by Shiva Bhowmik and Jeffrey T. Bolin, Purdue University, IN, USA), HsaD (2VF2, chain A)[68], and MhpC (1U2E, chain B)[69].

Chapter 3: RESULTS

3.1 Mechanistic analysis of $BphD_{LB400}$

At the outset of these studies a general base mechanism of catalysis by the MCP hydrolases was prevailing in the literature[87]. In spite of the apparently defined reaction mechanism, continued efforts to more precisely define the chemical mechanism of the MCP hydrolases stimulated the generation of a $BphD_{LB400}$ H265Q variant. In collaboration with the Bolin Lab at Purdue University, $BphD_{LB400}$ H265Q was crystallized and incubated with HOPDA, yielding a covalent Ser112-benzoyl adduct. The observation of an acyl-enzyme in $BphD_{LB400}$ H265Q (PDB ID: 3V1N) represented the first experimental demonstration of a possible reaction intermediate on the MCP hydrolase reaction pathway. These results contradicted previous attempts to trap or identify an acyl-enzyme intermediate during MCP hydrolase catalysis in solution[64,83], and prompted further study.

3.1.1 A pre-steady-state kinetic burst of HPD formation from $BphD_{LB400}$

A previously proposed two-conformation model of catalysis predicts the existence of a pre-steady-state burst of HPD formation during the hydrolysis HOPDA[81], which is also in line with a covalent mechanism of catalysis in which $k_{acylation} > k_{deacylation}$. Thus, to further investigate the chemical and kinetic mechanism of the MCP hydrolases, pre-steady-state kinetic studies of the turnover of HOPDA by $BphD_{LB400}$ were performed using stopped-flow spectrophotometry. Multiple turnover reactions were performed using 1, 2 or 4 μM $BphD_{LB400}$ and 20 μM HOPDA in KPi (I = 0.1 M), pH 7.5 at 25 °C. The reactions were monitored at 270 nm and the resulting pre-steady-state kinetic burst (Figure 19) was ascribed to HPD formation, as previously described[111]. The values derived from fitting the spectrophotometric measurements with a burst equation are summarized in Table 2. The pre-

steady burst rate constant, k_{burst} ~55 s^{-1}, is in agreement with that observed, $1/\tau_2$ ~50 s^{-1}, and provisionally assigned to acylation under single turnover conditions[81]. Interestingly, the magnitude of the burst accounted for only half of the enzyme used in each assay, consistent with the two-conformation model and the proposal that $BphD_{LB400}$ and other MCP hydrolases are half-site reactive enzymes.

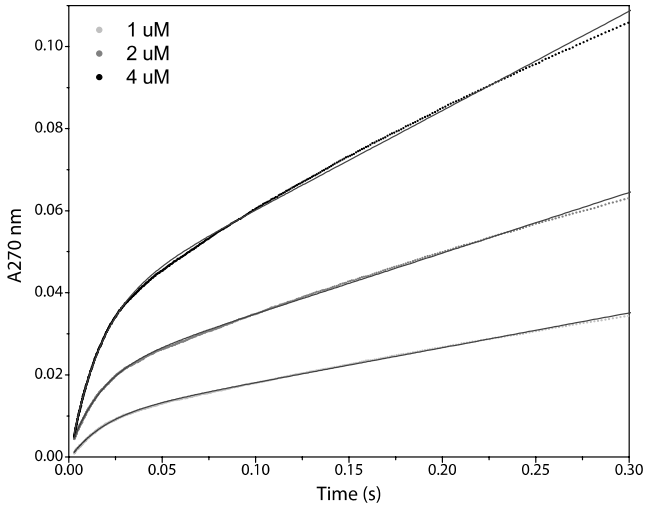

Figure 19. Representative stopped-flow experiments demonstrating a pre-steady-state burst of HPD formation by $BphD_{LB400}$ in KPi (I = 0.1 M), pH 7.5 at 25 °C. Enzyme concentrations are indicated. The data has been normalized to account for the combined starting absorbance of the enzyme and substrate.

The measured steady-state rate constants, k_{ss}, were slightly slower than the previously determined k_{cat} values of 4.2[37] or 6.5 s^{-1}[81], and the burst equation could not account for data beyond 0.25 s at higher enzyme concentrations. This slight divergence from linearity in the kinetic traces can be explained by substrate depletion, which was ~20% after 0.3 s at 4 μM enzyme. Concomitant product accumulation and inhibition (K_{ic} HPD ~80 μM, K_{iu} HPD ~120 μM and K_{ic} benzoate ~160 μM[81]) as well as a combination of non-enzymatic and enzymatic ketonization of HPD, which is associated with a decay of the signal at 270 nm are likely to contribute to the apparent reduction in the observed k_{ss}. This is supported by the decrease in k_{ss} with increasing enzyme concentration. Thus, while the experiment allowed the

definition of a pre-steady-state burst of product formation, it did not afford an accurate determination of k_{cat}.

Table 2. Pre-steady-state kinetic parameters derived from monitoring HPD formation[a]

[E] (μM)	k_{burst} (s^{-1})	Amp_{burst} (ΔA_{270nm})	$[P]_{burst}$ (μM)	v_{ss} (ΔA_{270nm} s^{-1})	k_{ss} (s^{-1})
1	52 ± 5	0.0098 ± 0.0007	0.51 ± 0.04	0.081 ± 0.007	4.2 ± 0.4
2	55 ± 5	0.0199 ± 0.0008	1.04 ± 0.04	0.150 ± 0.003	3.91 ± 0.08
4	62 ± 1	0.0376 ± 0.0007	1.96 ± 0.04	0.243 ± 0.004	3.16 ± 0.05

[a] $\varepsilon_{270\ nm\ HPD} = 19.7\ mM^{-1}cm^{-1}$[111]

3.1.2 Single turnover of HOPDA by $BphD_{LB400}$ His265Q

The measured half-site reactivity helps to account for the biphasic HPD formation observed during the single turnover of HOPDA by $BphD_{LB400}$ WT[81]. However, hydrolysis was readily observed in the H265A variant[66]. Moreover, the aforementioned crystalline acyl-enzyme was observed in the H265Q variant[112]. In contrast, mutation of the catalytic His in serine hydrolases results in the abrogation of enzyme activity[73]. His265 was also proposed to play a critical role in substrate tautomerization in $BphD_{LB400}$[66,81]. Thus, to complement the crystallographic studies, single turnover experiments were performed to evaluate the kinetic behaviour of the H265Q variant and the ability of the S112A/H265Q variant to accumulate an electronically perturbed intermediate.

In $BphD_{LB400}$ WT, ES^{red} is rapidly formed, exceeding the detection limit of the stopped-flow instrument, $1/\tau_1 > 500\ s^{-1}$. Next, ES^{red} decays in a biphasic manner, which is mirrored by an increase in absorbance at 270 nm, ascribed to HPD formation (Table 3). Under identical conditions, the reaction of 8.1 μM H265Q and 4 μM HOPDA in KPi (I = 0.1 M), pH 7.5 at 25 °C, could also be described by three discrete transient kinetic phases. Instead of ES^{red} formation, a small hyper- and hypsochromic shift to 430 nm was observed during a single catalytic cycle of H265Q, monitored using a PDA detector. The hyper- and 4

nm hypsochromically-shifted spectrum was consistent with the presence of a dianionic enolate substrate at the active site. This ES species then decayed in two phases. The first decay phase, $1/\tau_2$, proceeded at 10.3 s^{-1}, approximately 5-fold slower than that of ES^{red} decay in the WT and 8-fold faster than the enolate decay observed in the H265A variant. This phase was provisionally assigned to acylation based on monitoring HPD formation at 270 nm, for which a rate constant of 10.8 s^{-1} was determined. The second phase of enolate decay in H265Q, $1/\tau_3$ of 0.022 s^{-1} was similar to an observable relaxation at 270 nm, occurring at 0.08 s^{-1}. Interestingly, in the His265 variants, the slowest processes observed under single turnover conditions do not match the k_{obs} values measured in the presence of excess substrate, which in the case of H265Q is reduced by 10^6-fold (Table 3).

Table 3. Kinetic data for wild-type $BphD_{LB400}$ and its His265 variants[a]

Enzyme	λ (nm)	$1/\tau_1$ (s^{-1}) [%Amp]	$1/\tau_2$ (s^{-1}) [%Amp]	$1/\tau_3$ (s^{-1}) [%Amp][a]	k_{cat} (s^{-1})[b]
WT[c]	270		50 ± 10 [89]	8.3 ± 0.7 [11]	6.5
	492	~500	54 ± 3 [64]	5.8 ± 0.9 [32]	
H265A[d]	434	78 [82]	1.3 [18]		0.0058
H265Q	270		10.8 ± 0.6 [28]	0.08 ± 0.02 [72]	
	434	130 ± 10 [16]	10.3 ± 0.1 [21]	0.022 ± 0.001 [64]	3×10^{-5}

[a]Values in square brackets indicate the % change of the total signal amplitude associated with each rate constant [b]k_{cat} for H265Q was determined from the turnover of 50 μM HOPDA with 2 or 4 μM enzyme [c,d]Data was taken from [81] and [66], respectively.

The assignment of a dianonic species at the active site of the H265Q variant was supported by the observation of triphasic ES complex formation between HOPDA and the S112A/H265Q variant ($1/\tau_1$ = 114 ± 8 s^{-1}, $1/\tau_2$ = 32 ± 2 s^{-1} and $1/\tau_3$ = 0.78 ± 0.02 s^{-1}). The resulting stable S112A/H265Q:HOPDA complex was also hyperchromically shifted by ~125% ($\varepsilon_{434\,nm}$ = 32.1 ± 0.2 $mM^{-1}cm^{-1}$) and possessed a half-life of 31 hours. Curiously, the hyperchromic shift accounted for only half of that expected for the complete conversion to an all enolate sample ($\varepsilon_{434\,nm}$ = 40.1 $mM^{-1}cm^{-1}$). Incubation of HOPDA with a two-fold excess

of S112A/H265Q in Na-CHES (I = 0.1 M), pH 9.5 at 25 °C, shifted the enolate band to 432 nm without a significant change in absorptivity.

3.1.3 Identification of an acyl-enzyme intermediate in variant and WT enzymes

The observation of pre-steady-state kinetic burst and HPD production from the single turnover of HOPDA by $BphD_{LB400}$ H265Q with a measured rate constant comparable to the WT enzyme stimulated further investigation of catalytically relevant intermediates. Specifically, chemical quench experiments were performed during turnover of 20 μM HOPDA by 4 μM WT or the H265Q variant in KPi (I = 0.1 M), pH 7.5 at 25 ºC. The quench times were selected based on the observed k_{cat} value for the WT or after $1/\tau_2$ for the H265Q variant. LC ESI/MS analyses of the acetic acid quenched reactions (5% v/v final) indicated that ~40% of the H265Q variant (Figure 20A) was benzoylated (M+104) after 600 ms while ~45% of the WT was benzoylated after 200 ms (Figure 20B). The signals for the unmodified WT and H265Q variant were observed at 31898 and 31889 m/z, respectively, which corresponded exactly to the theoretical values for $BphD_{LB400}$ enzymes missing their N-terminal methionine. In WT-catalyzed reactions, the proportion of benzoylated enzyme dropped to ~30% after 1 s (Figure 20C), and no acylated enzyme was detected after 10 s (Figure 20D). The later obviated the possibility of a non-enzymatic acid-catalyzed process leading to the sub-stoichiometric acylation. Indeed, the observed decay of the M+104 species in WT $BphD_{LB400}$ was consistent with the k_{ss} measured in kinetic burst experiments under similar conditions. Interestingly, the rapid acylation of $BphD_{LB400}$ H265Q indicated that this process, and accordingly, nucleophile activation was His265-independent, and allowed for the assignment of $1/\tau_2$ and $1/\tau_3$ to acylation events.

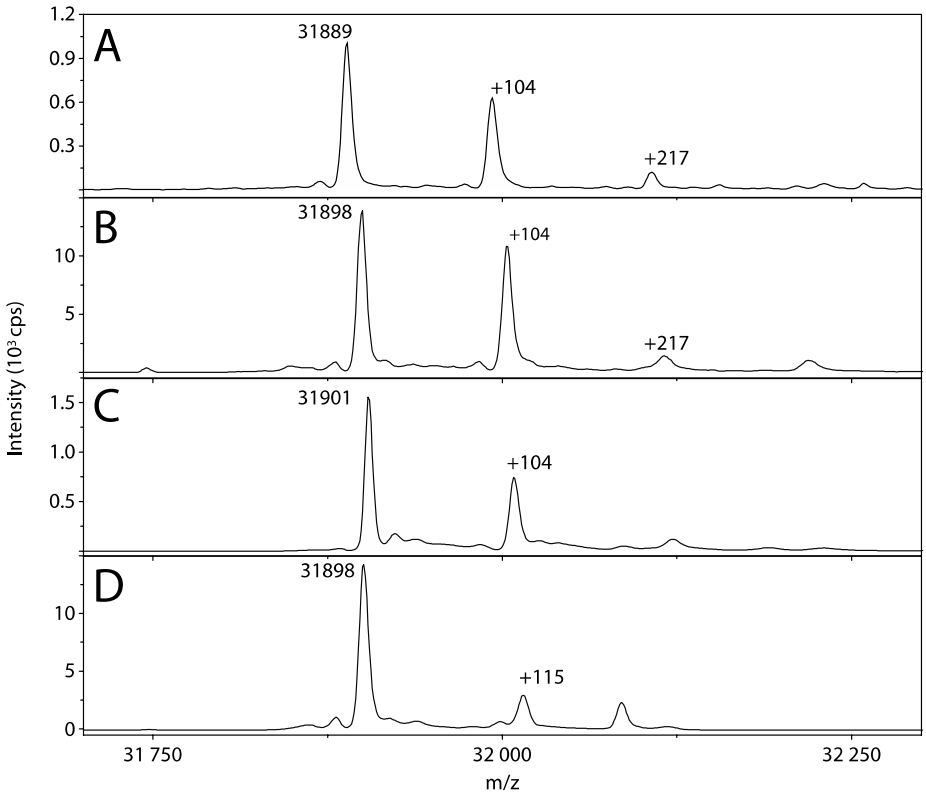

Figure 20. Whole protein LC ESI/MS analysis of $BphD_{LB400}$ reacted with HOPDA. Reactions contained 4 μM enzyme and 20 μM HOPDA in KPi (I = 0.1 M), pH 7.5 at 25 °C. (A) An H265Q-catalyzed reaction was quenched after 600 ms. The WT-catalyzed reactions were quenched after (B) 200 ms, (C) 1 s and (D) 10 s. The additional peak observed at M+115 is consistent with a non-covalent WT:HPD adduct and the M+217 peak is consistent with either a non-covalent WT:HOPDA complex or a benzoylated enzyme:HPD complex.

Peptide matching from LC ESI/MS/MS of pepsin-digested reaction mixtures was used to umabiguously identify the site of enzyme modification. The benzoylation of Ser112 was confirmed from a hydrophobic peptide identified in samples from WT and H265Q reactions with HOPDA that were allowed to age 200 and 600 ms, respectively, before quenching with 5% acetic acid (v/v). The peptide spanned residues 102-120 (DIDRAHLVGNSMGGATALNF), containing several missed pepsin cleavage sites. Peptide fragment ions, matched in both the WT and H265Q samples, indicated modification of Ser112. In total, 15 ion fragments from the WT reaction mixture and 6 ion fragments from the H265Q sample were matched to *b*-series ions that could be explained only by

benzoylation at Ser112 (Figure 21, Table 23 in Appendix II). Both modified and unmodified peptides could be identified from each reaction mixture and their apparent stoichiometry was consistent with the amount of benzoylation observed in the intact enzyme samples.

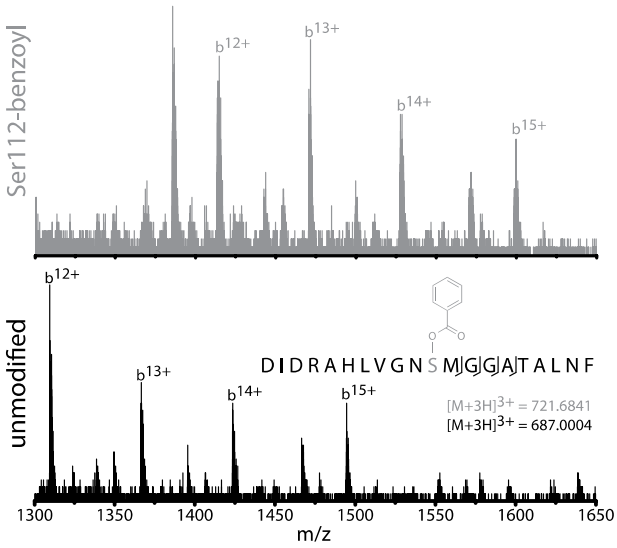

Figure 21. ESI/MS/MS of a modified and an unmodified peptide isolated from $BphD_{LB400}$ WT. For simplicity, the high m/z range is shown to highlight the differences in large *b*-series ions.

3.1.4 Stoichiometric incorporation of ^{18}O into benzoic acid from reactions in $H_2{}^{18}O$

Identification of an acyl-enzyme intermediate during the catalytic cycle of $BphD_{LB400}$ conflicted with reports on the stoichiometry of ^{18}O incorporation into the succinic acid product of the MhpC-catalyzed hydrolysis of 2-hydroxy-6-oxo-nona-2,4-diene-1,9-dioic acid. Importantly, these experiments were the impetus for the proposed general base mechanism in the MCP hydrolases[64]. To test whether $BphD_{LB400}$ behaves similarly, 200 μM HOPDA was hydrolyzed using 20 μM $BphD_{LB400}$ in KPi (I = 0.1 M), pH 7.5 at 92% $H_2{}^{18}O$ (v/v) and the resulting benzoic acid product was analyzed using EI/GC/MS. The observed distribution of ion fragments reflected both the extent of ^{18}O incorporation and the isotopic abundance of silicon in the derivatization agent. Therefore, the average distribution

of ion fragments observed in control reactions performed using H_2O was used to calculate the extent of ^{18}O incorporation into benzoic acid observed from the reactions performed in $H_2{}^{18}O$ (Figure 22). In these calculations, two models were fit to the observed fragment ion distributions: (i) a two-species model, representing a single ^{18}O incorporation event, and (ii) a three species model, representing single and double incorporation event (Table 22, Appendix II). In turnover experiments performed using $H_2{}^{18}O$, the two-species model best fit the data. The result for the most abundant fragment, summarized in Table 4, indicates 85 ± 1% incorporation of a single ^{18}O equivalent. Similar results were observed in all other oxygen-containing fragments of benzoic acid (Table 23, Appendix II). This experiment provided no evidence for the enzymatic incorporation of a second ^{18}O equivalent into the benzoic product: in no case were ions at M+6 and M+7 observed, and modeling incorporation of a second ^{18}O equivalent into even a small percentage of the benzoate increased the error associated with the overall relative abundance of the singly exchanged species. For example, using the data presented in Table 4, modeling the incorporation of a second ^{18}O equivalent into just 3% of the product increased the error associated with the overall relative abundance of the single exchanged species by 5-fold. Moreover, the enzyme did not catalyze any detectable solvent exchange into benzoic acid, even over 300 min (Table 4). However, non-enzymatic ^{18}O exchange from the solvent into HOPDA was observed at 18% over 20 min (Table 4). The pre-incubation of HOPDA in ^{18}O-buffer for up to 20 min did not increase the stoichiometry of incorporation observed into the benzoic acid product. This result indicated that exchange occurred exclusively at the C2-substituent (Figure 22), suggesting that HOPDA exists predominantly as a 2-oxo-6-oxido-3,5-dienoate in solution at pH 7.5. Overall, the results are consistent with the occurrence of an acyl-enzyme intermediate and argue

against the non-productive release of a tautomerized substrate from $BphD_{LB400}$.

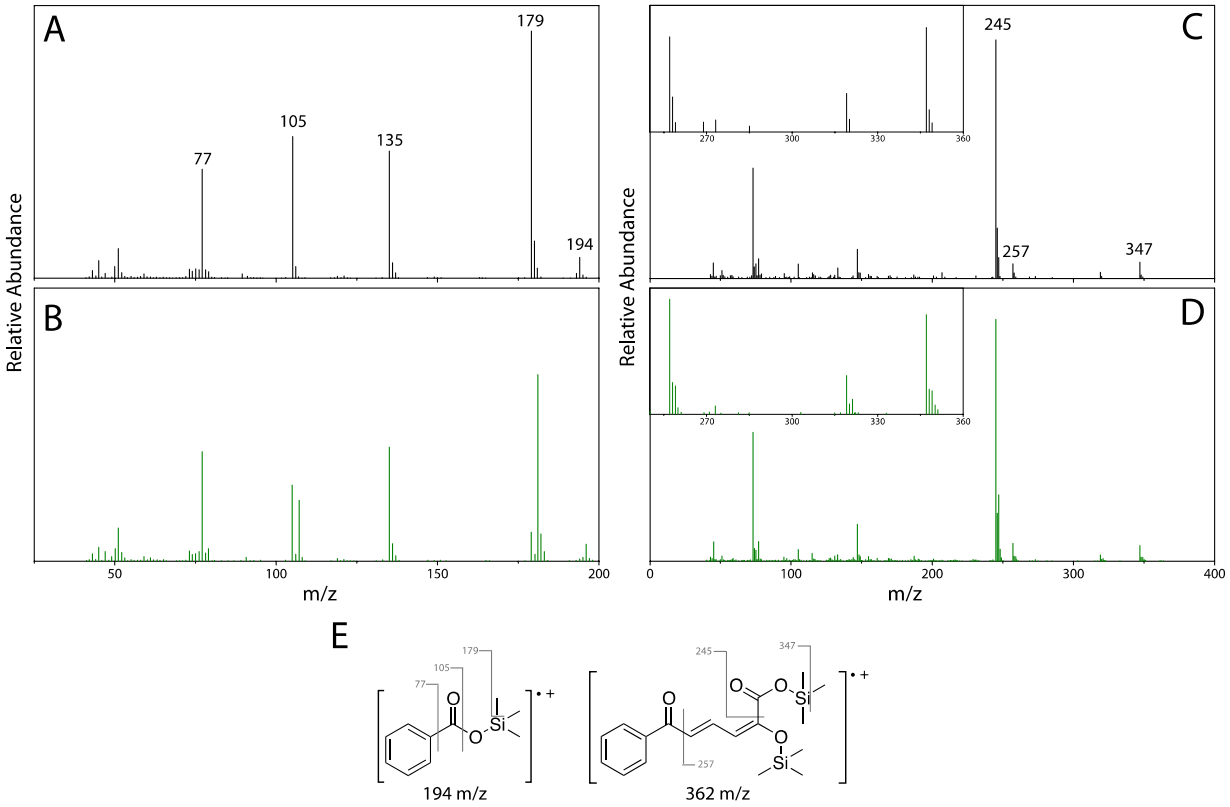

Figure 22. Results from representative EI/GC/MS analysis of (A) benzoate in H_2O, (B) benzoate derived from $BphD_{LB400}$-mediated hydrolysis of HOPDA in $H_2{}^{18}O$, (C) HOPDA in H_2O, and (D) HOPDA in $H_2{}^{18}O$. Inset panels (C and D) highlight the lower intensity HOPDA ion fragments. (E) Parent ions and predicted fragments.

Table 4. Incorporation of ^{18}O from $H_2{}^{18}O$ into benzoate and HOPDA[a]

Sample	Time (min)	Relative abundance (%) of benzoate base peak ions (m/z) 179 [M]	180 [M+1]	181 [M+2]	182 [M+3]	183 [M+4]	184 [M+5]	^{18}O incorporation
Benzoate in H_2O		83.2	12.9	3.4	0.44			
WT + benzoate in $H_2{}^{18}O$	300	83	12.3	4.3	0.4			ND
WT + HOPDA in $H_2{}^{18}O$	20	12	2.7	71	10.7	3.6	0.3	85 ± 1%
WT + HOPDA in $H_2{}^{18}O$	20 *PI*[b]	16.7	3.3	65	10	4	0.5	79 ± 2%
		Relative abundance (%) of HOPDA base peak ions (m/z)						
		245 [M]	246 [M+1]	247 [M+2]	248 [M+3]	249 [M+4]	250 [M+5]	
HOPDA in H_2O	20	78	16	5	0.5			
HOPDA in $H_2{}^{18}O$	20	65	12.7	17.9	3.2	1.0	0.12	18 ± 1%

[a]The errors reported for ^{18}O incorporation represent the root mean square deviation from fitting the experimentally observed data to a single ^{18}O incorporation event [b]*PI*: HOPDA was pre-incubated in ^{18}O-buffer for 20 min prior to initiating the reaction.

3.1.5 Insight into $BphD_{LB400}$ deacylation from nucleophile partitioning

The methanol-dependent steady-state kinetic turnover of HOPDA by $BphD_{LB400}$ was initially reported as indirect evidence for acylation. Partitioning of an acyl-enzyme with water or methanol thus produced benzoate or methyl-benzoate, and a simple kinetic model of nucleophilic catalysis accounted for the observed methanol-dependent increase in k_{cat} and K_m and the independence of k_{cat}/K_m[101]. Accordingly, a more extensive number of alcohols were employed in order to identify the rate-limiting step during the hydrolysis of HOPDA by $BphD_{LB400}$. The effect on initial reaction velocities (v_0) and the partitioning between water and short primary alcohols were assessed. It was rationalized that the effect of distinct alcohols on the steady-state rate of C-C bond cleavage could allow for the dissection of the chemical and physical events that have been correlated to k_{cat}[81]. More specifically, these experiments exploit differences in the pK_a of the small alkoxides from water to provide insight into the deacylation event.

The effects of several alcohols on the v_0 of $BphD_{LB400}$-catalyzed turnover of 10 μM HOPDA were measured. In the absence of alcohol, v_0 was 25 ± 1 μM s^{-1} (Table 5). Alcohol concentration-dependent increases in v_0 were apparent upon the addition of either methanol, ethanol, or 1-propanol. The observed effects ranged from an approximate 3.2-fold increase in the presence of 100 mM methanol to a more modest 1.2-fold increase at the same concentration of 1-propanol. Inspection of the series indicates that the increase in v_0 reflect the lower pK_a of the substituting alkoxide. Importantly, v_0 was not significantly affected by the addition of 25 or 100 mM 2-propanol, suggesting that the tested alcohols compete to replace the nucleophilic water and do not contribute any allosteric effects that accelerate the reaction. The possible inhibitory effects of each alcohol were not tested in light of the

observed rate accelerations. In addition to the observed kinetic phenomena, HPLC analysis of the reaction products was used to correlate these observed accelerations in v_0 directly to alcohol utilization by $BphD_{LB400}$ (Table 5).

Table 5. The effect of alcohol on $BphD_{LB400}$-mediated HOPDA hydrolysis[a]

	[Alcohol] (mM)	v_0 ($\mu M\ s^{-1}$)	Product ratio acid:ester
	0	25 ± 1	
methanol	25	45.8 ± 0.7	1.06 ± 0.01
	100	76 ± 1	0.24 ± 0.01
ethanol	25	29.4 ± 0.9	3.78 ± 0.05
	100	45.9 ± 0.7	0.95 ± 0.02
1-propanol	25	26.0 ± 0.6	42.8 ± 0.8
	100	29 ± 1	3.57 ± 0.07
2-propanol	25	25.8 ± 0.6	ND
	100	25.5 ± 0.3	ND

[a]Spectrophotometric determination of v_0 and HPLC determination of product ratios were performed at 10 μM and 40 μM HOPDA, respectively.

Partitioning between the hydrolytic and alcoholytic reaction pathways could be linked to common v_0 measurements. For instance, using either 25 mM methanol or 100 mM ethanol, the acid:ester ratio was ~1 and v_0 ~46 $\mu M\ s^{-1}$. Similarly, the same v_0 was observed using 25 mM ethanol and 100 mM 1-propanol (~29 $\mu M\ s^{-1}$), and the acid:ester product ratio was ~3.6. Taken together, the results suggest that hydrolysis of the acyl-enzyme is the rate-limiting step in catalysis by $BphD_{LB400}$.

3.1.6 Proposal of a substrate-assisted mechanism of nucleophile activation

The His265-independent acylation of $BphD_{L400}$ argues for a novel mechanism of nucleophile activation in this Ser-His-Asp containing enzyme. Instead of using the canonical His-Asp dependent mechanism of serinate formation described for the serine hydrolases, a substrate-assisted mechanism of nucleophile activation (Figure 23) could account for the observed kinetic and chemical quench data. In the proposed mechanism, the highly-

conserved MCP hydrolase active site acts allows the dianionic substrate to act as a general base for the activation of the nucleophilic Ser. In turn, a proton transfer from the serine hydroxyl to C5 of the substrate completes the requisite substrate ketonization. The following sections were aimed to investigate this mechanism.

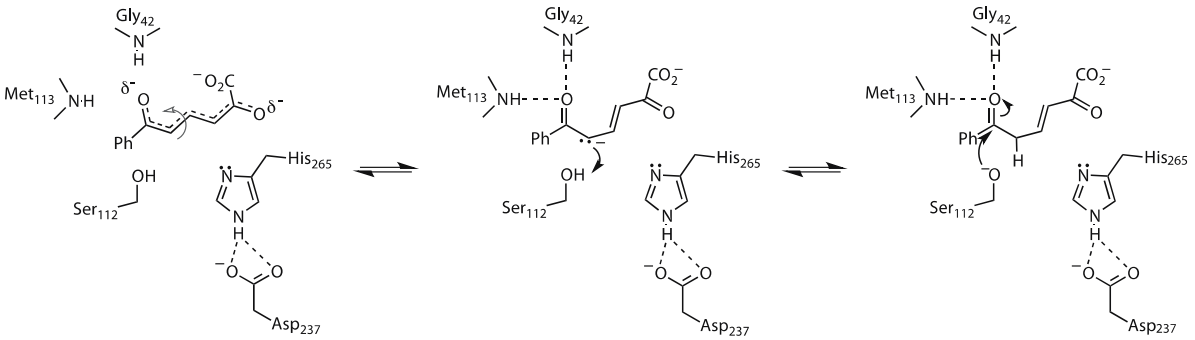

Figure 23. The proposed substrate-assisted mechanism of nucleophile activation. In the first panel, no formal charge is drawn on the dieneoate moiety of the HOPDA dianion and a grey arrow indicates rotation about the C4-C5 bond. The second panel shows a formal charge at C5 that is rationalized by the pre-requisite proton transfer reaction that occurs at this position. In the third panel, only the transferred proton is drawn on C5 to highlight this reaction.

3.2 Characterization of BphD$_{LB400}$ esterase activity

3.2.1 Methanol-dependent esterase activity

The *in vitro* MCP hydrolase esterase activity is well-documented[93,113-115]. A common k_{cat} value of ~6.5 s^{-1} was determined for the steady-state hydrolysis of HOPDA and pNPB by BphD$_{LB400}$. In the presence of 25 mM methanol, equal partitioning of the benzoyl-containing products was also observed for both C-C and C-O bond cleavage reactions[101]. The commonalities between the cleavage of pNPB and HOPDA represent indirect evidence for a shared benzoyl-enzyme intermediate, challenging the proposed general base mechanism for C-O bond cleavage[93]. To further investigate the mechanism of C-O bond cleavage by the MCP hydrolases, the methanol-dependent turnover of pNPB by BphD$_{LB400}$ was measured by monitoring pNP formation at 400 nm (Table 6). The reactions were conducted at 25 °C in

KPi (I = 0.1 M), pH 7.5 supplemented with 0.2% acetone (v/v) to facilitate the solubilization of pNPB. Unfortunately, the relatively low solubility of pNPB precluded reliable determination of steady-state kinetic parameters in the presence of methanol. Despite this limitation, the rate of BphD-catalyzed C-O bond cleavage at 2 and 4 μM pNPB provided some mechanistic insight. As was observed for the transformation of HOPDA[101], the rate of pNPB turnover increased with methanol concentration. However, the k_{obs} value also decreased at methanol concentrations greater than 250 mM. This apparent decrease in activity likely reflects an increase in the K_m pNPB similar to the previously observed methanol-dependent increase in $K_{m\ HOPDA}$. At lower methanol concentrations, the concentration of pNPB is assumed to be saturating, and the k_{obs} values for turnover were within error of the k_{cat} values determined for the cleavage of HOPDA.

The methanol-dependent product formation for the $BphD_{LB400}$-mediated of 4 μM pNPB cleavage was measured by HPLC and correlated well with the observed acceleration to the rates of bond cleavage. In order to compare nucleophile partitioning for C-O and C-C bond cleavage, methanol-dependent product formation from steady-state HOPDA turnover was also measured by HPLC. As for the pNPB reactions, 4 nM $BphD_{LB400}$ was used to cleave 40 μM HOPDA at varying concentrations of methanol. The partitioning ratio, reported as the percent of benzoic acid produced, was the same for the two reactions (Table 6). Furthermore, these studies helped to definitively link the observed kinetic phenomenon to a simple nucleophilic model of catalysis, which accurately predicted the partitioning ratios[101].

Table 6. Observed rates of methanol-dependent pNPB and HOPDA cleavage[a,b]

[MeOH]	2 μM pNPB	4 μM pNPB		HOPDA		
(mM)	k_{obs} (s^{-1})	k_{obs} (s^{-1})	% acid[c]	k_{cat} (s^{-1})[a]	K_m (μM)[a]	% acid[c]
0	6.4 ± 0.3	6.5 ± 0 .1	100 ± 1	6.5 ± 0.5	0.2 ± 0.05	100 ± 2
25	9.9 ± 0.5	10.7 ± 0.5	49 ± 1	9.4 ± 0.5	0.4 ± 0.1	48 ± 2
62	12.8 ± 0.2	14.6 ± 0.3	29 ± 1	13	0.6	27 ± 2
124	16 ± 1	18.4 ± 0.1	20 ± 1	16	0.83	17 ± 1
247	17 ± 2	21 ± 1	14.4 ± 0.7	21 ± 4	0.8 ± 0.2	20 ± 1
618	14 ± 1	20.1 ± 0.8	5.7 ± 0.3	21 ± 5	0.99 ± 0.07	4.9 ± 0.3
1240	11 ± 1	17.0 ± 0.4	3.7 ± 0.2	28 ± 4	2.0 ± 0.4	3.0 ± 0.2

[a]Data taken from [101] [b]$k_{obs} = v_0/[E]_T$ [c]% benzoic acid observed relative to a hydrolytic reaction.

3.2.2 Activation of the Serine nucleophile for C-O bond hydrolysis

While the methanol-dependent steady-state kinetic data and HPLC analysis of the corresponding nucleophile partitioning suggest that both the C-O and C-C hydrolytic reactions proceed through an acyl-enzyme intermediate, they do not establish the mechanism of nucleophile activation. The ester substrate lacks the requisite electron rich system proposed to facilitate serinate formation in the substrate-assisted mechanism for C-C bond cleavage. Accordingly, ester bond hydrolysis was further probed using stopped-flow spectrophotometry to monitor the hydrolysis of pNPB by $BphD_{LB400}$ WT and three catalytic triad variants: S112A, H265A and H265Q. The turnover of 2 μM pNPB by 1 or 2 equivalents of WT enzyme resulted in the biphasic production of pNP (Table 7), reminiscent of HPD formation during HOPDA turnover[81]. However, even at equal reactant concentrations, the second phase of pNP production, k_2 ~41 s^{-1}, was approximately 7-fold faster than k_{cat}, suggesting that an additional process, downstream of pNP release, is rate-determining but cannot be directly observed at 400 nm. Again, these results are consistent with the rate-limiting deacylation during $BphD_{LB400}$-catalyzed C-O bond cleavage.

Table 7. Single turnover kinetic data for pNPB turnover by $BphD_{LB400}$ and catalytic variants[a]

[E]:[pNPB]	k_1 (s^{-1}) [%Amp]		k_2 (s^{-1}) [%Amp]	
1 WT	210 ± 40	[18]	41 ± 5	[82]
2 WT	170 ± 10	[38]	74 ± 2	[62]
4 WT	206 ± 5			
4 H265A[b]	0.06			
4 H265Q	0.014 ± 0.002			
4 S112A	0.00016 ± 0.00002			

[a]The error associated with each amplitudes was < 10% [b]value from a single experiment

Turnover of pNPB by a 4-fold excess of WT enzyme resulted in monophasic formation of pNP at 210 s^{-1}. Subsequently, experiments with $BphD_{LB400}$ variants were performed using a 4-fold excess of enzyme (8 μM) to pNPB (2 μM). Substitution of Ser112 with alanine resulted in the near abrogation of C-O cleavage with pNP production occurring on an hour timescale, 0.58 h^{-1}. The rate constant for ester bond hydrolysis by the His265 variants were reduced by at least 3 orders of magnitude (Figure 24). Specifically, the H265A and H265Q variants cleaved pNPB at 0.06 and 0.014 s^{-1}, respectively. As compared to the modest reduction to the rate constant for acylation in the H265Q variant when reacting with HOPDA, the magnitude of the reduction in esterase activity argues for canonical Ser-His-Asp triad chemistry for C-O bond cleavage (Figure 25).

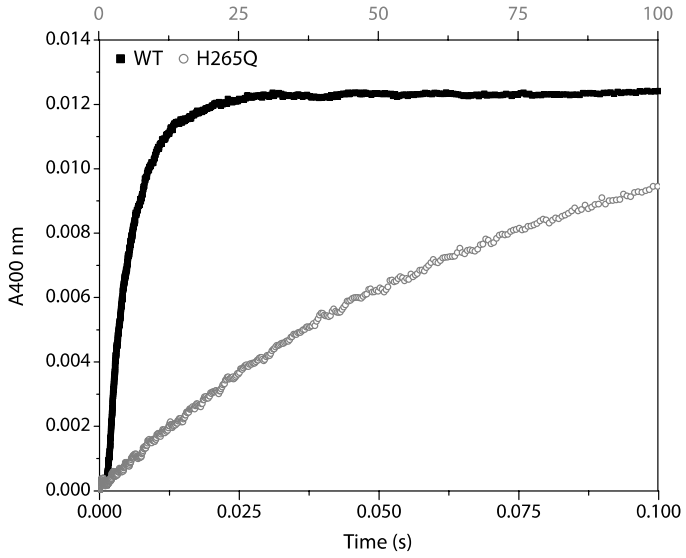

Figure 24. Results from representative stopped-flow experiments demonstrating the single turnover of 2 μM pNPB by 8 μM $BphD_{LB400}$ WT (black) and H265Q (grey) at 400 nm. The timescales for the WT and H265Q reactions are indicated on the bottom and top of the plot, respectively.

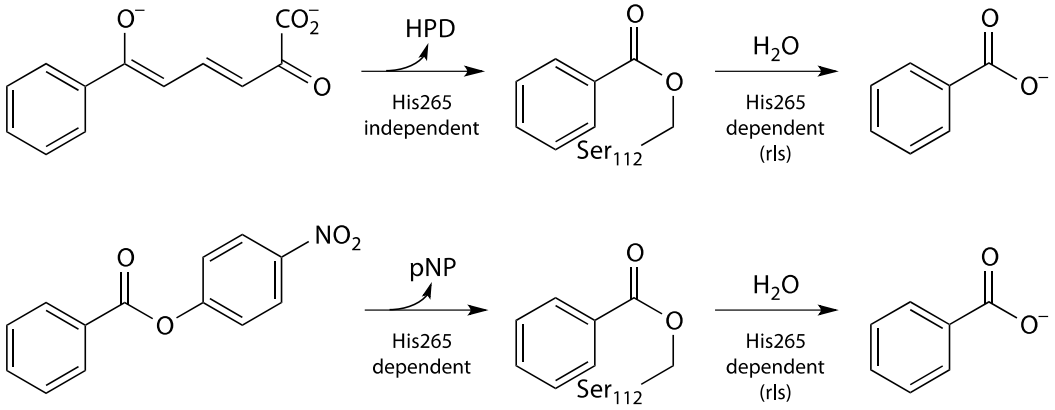

Figure 25. Proposed roles for His265 during the hydrolysis of C-C and C-O bonds by $BphD_{LB400}$. The rate-limiting step (rls) is indicated for the WT enzyme.

3.2.3 Biphasic pre-steady-state formation of pNP

To further investigate the biphasic product release observed during single turnover experiments, we monitored the turnover of 4-, 8-, and 20-fold excesses of pNPB by $BphD_{LB400}$. In contrast to previous reports[93], the kinetic traces from multiple pNPB turnovers were biphasic (Figure 26) and could be modeled by either burst or double-exponential equations (Table 8). Fitting a burst equation to the data revealed that the rate

constants for pNP formation during the burst phase (k_{burst} ~42 s^{-1}) and the steady-state phase (k_{ss} ~8 s^{-1}) were independent of enzyme concentration. These values were also consistent with k_2 observed at a 1E:1S ratio and the k_{cat}, respectively. The amount of pNP formed during the burst phase corresponded to ~70% of the enzyme present in the assay. Similarly, analysis using a double-exponential equation implied that ~60% of the enzyme was active during the pre-steady-state phase (k_1 ~50^{-1}). Values of k_2 from the fit of a double-exponential equation to the multiple-turnover data ranged from 0.8 to 2.8 s^{-1}, demonstrating a dependence on enzyme concentration. These values were also significantly lower than the experimentally determined k_{cat} ~6.3 s^{-1}.

The magnitude of the pre-steady-state burst of pNP was sub-stoichiometric but differed significantly from the value of 50% predicted from the two-conformation model proposed for C-C bond hydrolysis. While quantification of the pre-steady-state burst was helpful in defining the mechanism of HOPDA hydrolysis by $BphD_{LB400}$, the observation of 60-70% activity in the first catalytic cycle for ester bond hydrolysis most likely reflects the unusual reaction of a non-cognate enzyme-substrate pair. Nevertheless, the "burst-like" kinetic behaviour further supports the observation of rate-limiting deacylation in $BphD_{LB400}$.

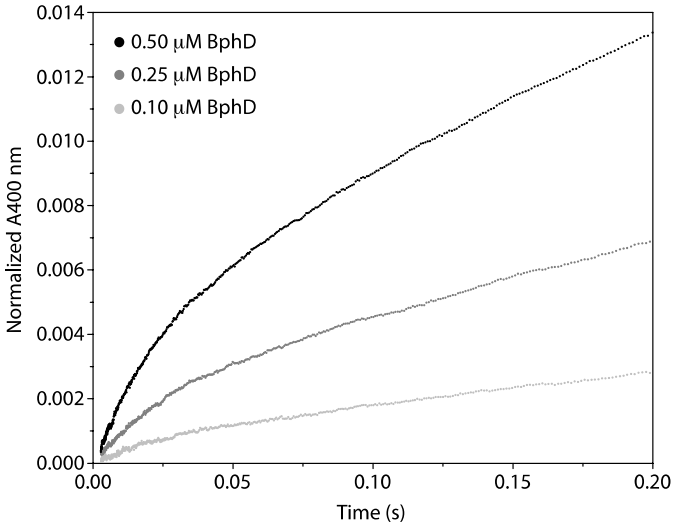

Figure 26. Results from representative stopped-flow experiments demonstrating the pre-steady-state formation of pNP by $BphD_{LB400}$ in KPi (I = 0.1 M), 0.2% acetone (v/v), pH 7.5 at 25 °C. The hydrolysis of 2 μM pNPB by 0.1 (light grey), 0.25 (dark grey) and 0.5 μM $BphD_{LB400}$ (black) was monitored.

Table 8. Pre-steady-state kinetic parameters derived from monitoring pNB formation[a]

Fits to a burst equation					
[E] (μM)	k_{burst} (s^{-1})	Amp_{burst} (ΔA_{400nm})	$[pNP]_{burst}$ (μM)	v_{ss} (ΔA_{400nm} s^{-1})	k_{ss} (s^{-1})
0.10	42 ± 3	0.00077 ± 0.00004	0.060 ± 0.003	0.0101 ± 0.0005	7.9 ± 0.4
0.25	41 ± 4	0.0022 ± 0.0001	0.17 ± 0.01	0.024 ± 0.001	7.4 ± 0.4
0.50	44 ± 5	0.0044 ± 0.0003	0.35 ± 0.02	0.046 ± 0.001	7.1 ± 0.2

Fits to a double exponential equation						
	k_1 (s^{-1})	[% Amp]	$[pNP]_{k1}$ (μM)	k_2 (s^{-1})	[% Amp]	$[pNP]_{total}$ (μM)[b]
0.10	44 ± 2	[5]	0.059 ± 0.004	0.8 ± 0.1	[90]	1.2 ± 0.2
0.25	47 ± 6	[8]	0.152 ± 0.007	1.4 ± 0.1	[92]	1.8 ± 0.1
0.50	60 ± 10	[12]	0.27 ± 0.02	2.8 ± 0.4	[88]	2.2 ± 0.3

[a]all errors associated with amplitudes were ≤ 12% [b]$[pNP]_{total}$ was calculated from ΔA400 nm

3.3 Mechanistic analysis of DxnB2

3.3.1 The oligomeric state of $BphD_{LB400}$ and DxnB2 are different

$BphD_{LB400}$ and DxnB2 share ~23% amino acid sequence identity and have been classified into phylogenetically distinct MCP hydrolase subfamilies. $BphD_{LB400}$ belongs to the well-studied class I subfamily, which also includes MhpC and HsaD whereas DxnB2 groups with class III enzymes[39]. As the reported oligomeric state differs for class I and III

MCP hydrolases, the quaternary structure of DxnB2 was compared to that of $BphD_{LB400}$ and HsaD in solution. Specifically, experiments were performed using enzyme samples at a concentration of 1.5 to 2.5 mg/ml in 20 mM HEPES, pH 7.5. SEC-MALS analysis indicated that DxnB2 exists as a dimer with a molecular weight of 58 ± 2 KDa (Figure 27). The tetrameric assemblies of $BphD_{LB400}$ and HsaD, which measured 132 ± 2 KDa and 121 ± 1 KDa were also confirmed by SEC-MALS.

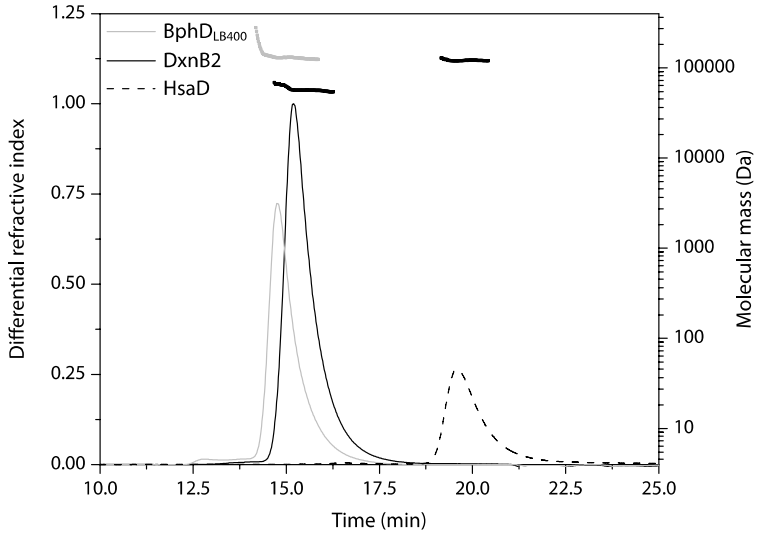

Figure 27. Superposition of chromatograms from SEC-MALS analysis of $BphD_{LB400}$ (grey), DxnB2 (black), and HsaD (dashed line). The data used for molecular mass determination has been overlaid on the chromatogram.

3.3.2 Evidence that DxnB2 also utilizes a nucleophilic mechanism of catalysis

3.3.2.1 A pre-steady-state kinetic burst of HPD formation

While previous steady-state kinetic analyses revealed that DxnB2 catalyzes the efficient (k_{cat}/K_m ~10^7 $M^{-1}s^{-1}$) hydrolysis of HOPDAs[39], no mechanistic information can be directly inferred from these studies. To further investigate the mechanism of catalysis by DxnB2, the pre-steady-state kinetic behaviour of the enzyme was probed using stopped-flow spectrophotometry. The hydrolysis of 20 μM HOPDA by 1 or 2.5 μM DxnB2 WT and 9-Cl HOPDA by 2.5 μM enzyme was measured in KPi (I = 0.1 M), pH 7.5 at 25 °C. These

substrates were selected on the basis of distinct steady-state kinetic behaviour: k_{cat} values measured for the DxnB2-mediated hydrolysis of HOPDA and all other tested monochlorinated substrates ranged between 0.13 and 0.88 s^{-1} with the exception of 9-Cl HOPDA for which k_{cat} was determined to be 5.1 s^{-1}[39]. As in $BphD_{LB400}$, reactions were monitored at 270 nm to follow the progress of HPD formation (Figure 28), and the values derived from fitting the stopped-flow measurements to a burst equation are summarized in Table 9. For HOPDA, a pre-steady-state burst occurred at ~62 s^{-1}. Quantification of the amount of HPD produced during each burst phase indicated that hydrolysis was 1:1 with enzyme concentration, suggesting that half-site reactivity may not be a universal feature of the MCP hydrolases. The observed steady-state rate constant for the hydrolysis (k_{ss}) was ~0.4 s^{-1}, similar to the previously reported value for k_{cat} ~0.47 s^{-1}[39].

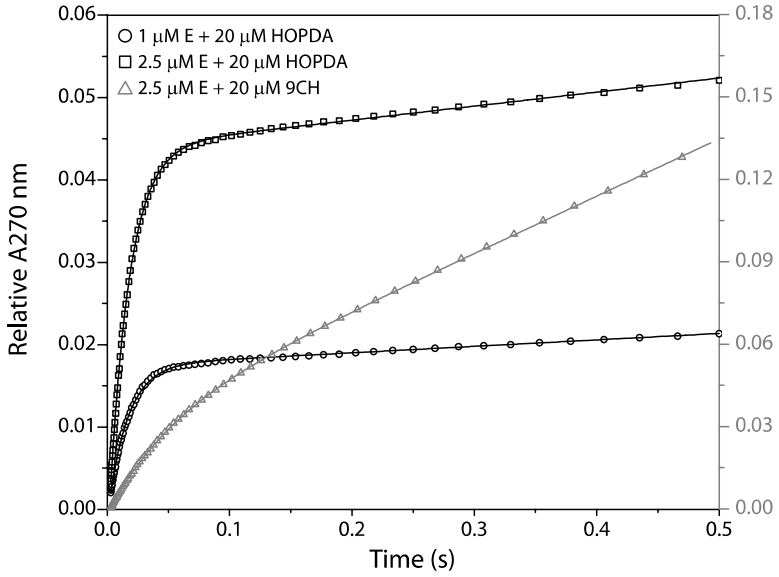

Figure 28. Representative stopped-flow experiments demonstrating the pre-steady-state kinetic burst of HPD formation from HOPDA (black) and 9-Cl HOPDA (grey) by DxnB2. For clarity, 1/10 data points are shown and distinct *y*-axes are shown.

Table 9. Pre-steady-state kinetic parameters derived from monitoring HPD formation

[E] (μM)	Substrate	k_{burst} (s^{-1})	Amp_{burst} (ΔA_{270nm})	$[P]_{burst}$ (μM)	v_{ss} (ΔA_{270nm} s^{-1})	k_{ss} (s^{-1})
1	HOPDA	63± 1	0.019± 0.002	1.01± 0.09	0.0079± 0.0002	0.41± 0.01
2.5	HOPDA	61.7± 0.7	0.048± 0.002	2.5± 0.1	0.0173± 0.0009	0.36± 0.02
2.5	9CH	20.0± 0.5	0.032± 0.004	1.67± 0.02	0.208± 0.003	4.34± 0.06

In contrast to HOPDA, quantification of HPD formed during the burst from the first turnover of 9-Cl HOPDA suggested that only ~67% of the enzyme was active. The observation of significant substrate inhibition during the reaction of DxnB2 and 9-Cl HOPDA, K_{si} ~6 μM, may account for this observed reactivity. Alternatively, the 9-Cl substituent may provide an additional structural determinant required to invoke the half-site reactive kinetic behaviour observed in $BphD_{LB400}$ or reflect the context of non-cognate substrate turnover by DxnB2. Finally, the quantification may also be less accurate for the turnover of 9-Cl HOPDA due to the comparable pre- and steady-state rates, k_{burst} and k_{ss}, which differ by less than 5-fold. Despite the unexplained nature of the burst of HPD from the hydrolysis of 9-Cl HOPDA, the observation of pre-steady-state kinetic bursts for both HOPDA and 9-Cl HOPDA is consistent with a proposal that DxnB2 utilizes a covalent mechanism of catalysis in which $k_{acylation} > k_{deacylation}$.

3.3.2.2 Identification of an acyl-enzyme intermediate in DxnB2 by LC ESI/MS

Similar to the manner in which an acyl-enzyme was initially identified in $BphD_{LB400}$, chemical quench experiments were performed on whole protein samples recovered from the turnover of a 5-fold excess of HOPDA or 9-Cl HOPDA by DxnB2. Reactions of 4 μM DxnB2 and 20 μM HOPDA or 9-Cl HOPDA were allowed to age for 10 or 1 s before quenching with a final volume of 5% acetic acid (v/v). LC ESI/MS analyses of the reaction mixtures revealed acylation of DxnB2 in both cases (Figure 29). The observed mass of

DxnB2 was 30198 ± 7 Da (~220 ppm) was within error of that predicted based on the protein sequence, 30194 Da. Additional peaks with masses shifted by 104 or 138 Da were taken to correspond to benzoylation or 3-chlorobenzoylation of DxnB2. Beyond acylation, peaks were observed that were tentatively assigned to non-covalent adducts. Based on the shift in m/z, these additional peaks included (i) an acyl-enzyme in complex with an additional substrate molecule, M+324 and M+388, for the reaction with HOPDA and 9-Cl HOPDA, respectively, (ii) a non-covalent DxnB2:9-Cl HOPDA adduct or 3-benzoylated enzyme:HPD binary complex with M+250, and (iii) an M+640 peak in the 9-Cl HOPDA sample, which may consist of a 3-chlorobenzoylated enzyme with two additional substrate molecules adventitiously bound. The observation of additional non-covalent complexes is unusual, but may reflect preservation of active sites throughout the experimental treatment and the observed micromolar K_{si} values for each substrate[39]. Moreover, the quenched reaction mixtures were concentrated to approximately 40 μM DxnB2 prior to analysis by LC ESI/MS. Interestingly, ~85% of DxnB2 was acylated based on estimating the area of each of the three distinct species observed from the reaction with HOPDA. This observation is more consistent with the 1:1 reactivity determined from the pre-steady-state kinetic burst experiments than the expected half-site reactivity that has been reported or inferred for other MCP hydrolases.

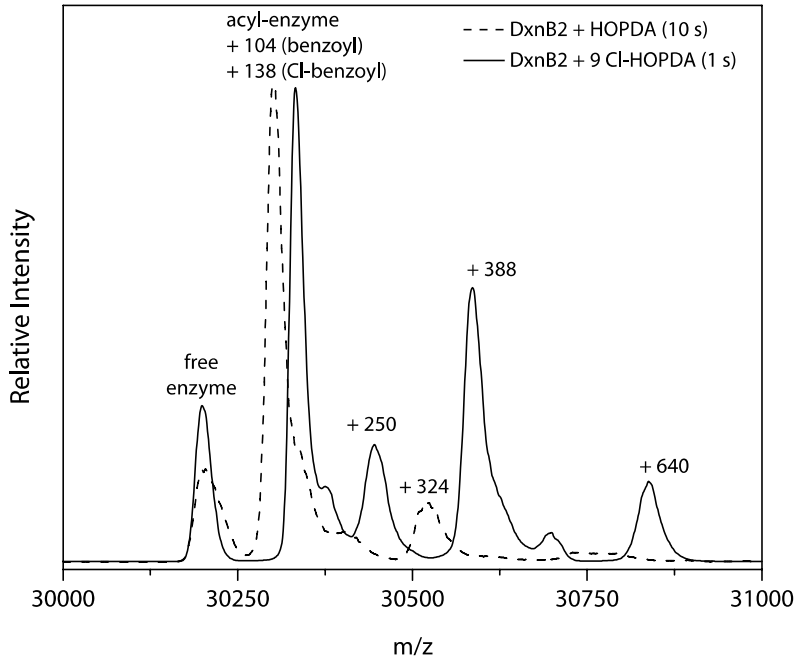

Figure 29. Whole protein LC ESI/MS analysis of DxnB2 reacted with HOPDA for 10 s (dashed line) or 9-Cl HOPDA for 1 s (solid line).

3.3.3 Single turnover of HOPDA by DxnB2

To further evaluate the kinetic mechanism of DxnB2, single turnover experiments were performed using 16 μM DxnB2 and 4 μM HOPDA in KPi (I = 0.1 M), pH 7.5 at 25 °C (Figure 30). A stopped-flow instrument outfitted with a PDA detector was utilized to identify any intermediates along the reaction pathway whereas a monochromator was employed to monitor reactions at a single wavelength. To distinguish intra- and intermolecular events, additional reactions were performed in the presence of a viscogen, either 30% sucrose (w/v) or 30% glycerol (v/v).

The hydrolysis of HOPDA by DxnB2 was biphasic. In this instance, ES^{red} was characterized by a λ_{max} at 487 nm and formed within the dead-time of the instrument ($1/\tau_1 >$ 500 s^{-1}). Subsequently, the red-shifted intermediate decayed at ~69 s^{-1}, which was mirrored by an increase in absorbance at 270 nm (Table 10). Following the hydrolysis of HOPDA, a relaxation attributed to HPD rebinding was also observed in the visible region, accounting for

~1% of the total change in amplitude (Figure 55, Appendix III). Likewise, the ketonization of HPD was also detectable at 270 nm (see section 3.3.5), a post-catalytic event that was previously reported for $BphD_{LB400}$[81]. Again, DxnB2 revealed no trace of half-site reactivity with respect to the hydrolysis of HOPDA, and the slowest rate constant determined from these experiments was ~150-fold faster than k_{cat}, consistent with a mechanism in which deacylation is rate-limiting.

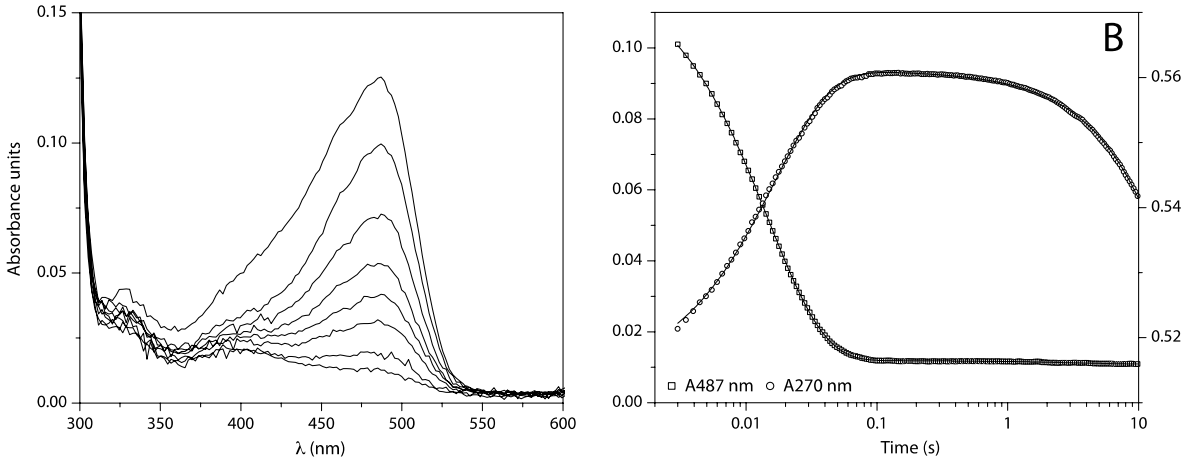

Figure 30. Results from representative stopped-flow experiments showing the single turnover of 4 μM HOPDA by 16 μM DxnB2. (A) Reaction monitored using a PDA detector. (B) Reaction monitored at single wavelengths: ES^{red} decay at 487 nm and HPD formation at 270 nm. For simplicity 1/10 data points are shown.

Interestingly, the addition of sucrose or glycerol to the reaction media did not affect $1/\tau_2$, measured as either the dissipation of ES^{red} or increase in absorbance at 270 nm (Table 10). In $BphD_{LB400}$, this transient kinetic phase was sensitive to both temperature and a viscogen, arguing for a dependence on product release, which in the two-conformation model is thought to precedes conformational changes that allow the second set of active sites to react[81]. The insensitivity of $1/\tau_2$ to viscogens in DxnB2 allows the provisional assignment of this transient kinetic phase to acylation, an on-enzyme event. While the data provide

accurate rate constants for acylation, an explicit assignment of the determinant(s) thereof cannot be inferred from a viscosity effect alone.

Table 10. Solvent viscosity effects on a single turnover of HOPDA by DxnB2

Buffer composition	λ (nm)	$1/\tau_2$ (s^{-1})
No viscogen	270	69 ± 2
	487	68 ± 1
30% sucrose (w/v)	270	67 ± 5
	487	69 ± 1
30% glycerol (v/v)	270	64 ± 5
	487	72.7 ± 0.5

3.3.4 Transient state solvent kinetic isotope effect (SKIE) for HOPDA hydrolysis

In contrast to $BphD_{LB400}$, the DxnB2-mediated cleavage of HOPDA was monophasic and impervious to solvent viscosity. Thus, it was rationalized that the measurement of a single turnover in deuterated reaction media could be employed to resolve the chemical step associated with ES^{red} decay. The presence of an SKIE on $1/\tau_2$ would argue for a rate-determining proton transfer, ultimately affording the explicit assignment of this observable kinetic phase to substrate ketonization or acylation in DxnB2.

Single turnover experiments were performed using 8.2 μM DxnB2 and 4 μM HOPDA in KPi (I = 0.1 M), pH or pD 7.5 at 25 °C (Figure 31). The isotopically enriched buffer contained 95% D_2O (v/v), and pre-incubation of HOPDA resulted in solvent exchange into the dienoate (Figure 56, Appendix III). As in H_2O, ES^{red} decay was monophasic and matched by an increase in absorbance at 270 nm. Despite using approximately half of the concentration of enzyme, $1/\tau_2$ was within error to that observed at 4E:1S (Table 11). Upon measuring the reaction in deuterated buffer, an SKIE of ~2.5 was observed, indicating that a proton transfer limited this observable transient kinetic phase. Therefore, $1/\tau_2$ could be assigned to substrate ketonization in DxnB2. Thus, acylation of DxnB2 is determined by

substrate protonation, which is linked to nucleophile activation in the substrate-assisted mechanism proposed for the MCP hydrolases.

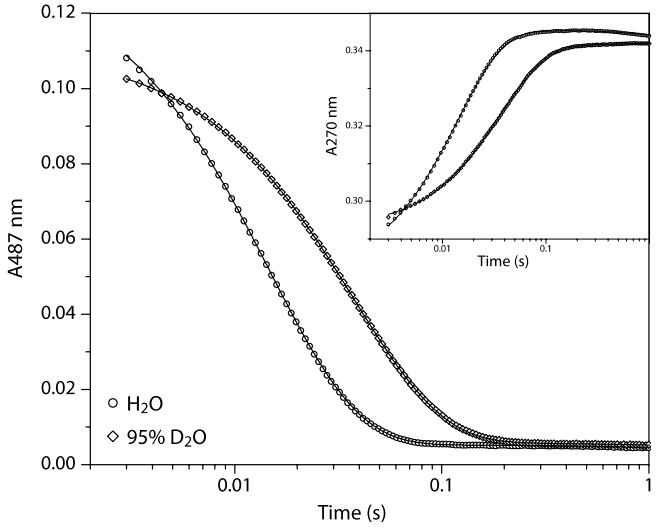

Figure 31. Representative stopped-flow experiments demonstrating a transient state SKIE on the rate of DxnB2-mediated HOPDA cleavage.

Table 11. Pre-steady-state solvent kinetic isotope effect on DxnB2 hydrolysis of HOPDA

	H_2O	95% D_2O (v/v)	
λ (nm)	$1/\tau_2$ (s^{-1})	$1/\tau_2$ (s^{-1})	SKIE
270	71 ± 2	28 ± 1	2.5 ± 0.2
487	67.7 ± 0.7	27.0 ± 0.3	2.50 ± 0.05

3.3.5 An extended Brønsted analysis of substrate ketonization

Confident assignment of an observable transient kinetic phase to substrate ketonization in DxnB2 facilitated a more robust investigation of this enzymatic process. The DxnB2-mediated hydrolysis of a series of substituted HOPDAs with varying basicity was measured by stopped-flow using a similar experimental approach described for the unsubstituted substrate. Additional reactions between 16 μM DxnB2 and 4 μM 5-Cl , 5,8-diF, 8-Cl or 9-Cl HOPDA were performed in KPi (I = 0.1 M), pH 7.5 at 25 °C (Table 12).

As previously described for HOPDA, the hydrolysis of 5-Cl HOPDA was biphasic.

Table 12. Kinetic data for the DxnB2-mediated hydrolysis of substituted HOPDAs

Substrate	λ (nm)	$1/\tau_1$ (s^{-1}) [% Amp]	$1/\tau_2$ (s^{-1}) [% Amp]	$1/\tau_3$ (s^{-1}) [% Amp]	$1/\tau_4$ (s^{-1}) [% Amp][a]
HOPDA	270		69 ± 2 [26 ± 0.2]		0.014 ± 0.001 [74 ± 5]
	487	> 500	68 ± 1 [98.9 ± 0.1]		0.6 ± 0.3 [1.1 ± 0.1]
5-Cl	270		2.9 ± 0.2 [23.9 ± 0.2]		0.05 ± 0.02 [80 ± 30]
	472	312 ± 5 [43 ± 1]	2.72 ± 0.01		
5,8-diF	270			0.132 ± 0.002 [20.6 ± 0.3]	0.0018 ± 0.0001 [79 ± 2]
	485	520 ± 20 [46 ± 4]	2.3 ± 0.3 [2.6 ± 0.6]	0.126 ± 0.001 [51.0 ± 0.5]	
8-Cl	270		4.3 ± 0.1 [43.9 ± 0.6]	1.0 ± 0.2 [52 ± 1]	0.039 ± 0.001 [52 ± 1]
	472	> 500	5.0 ± 0.1 [73 ± 1]	1.76 ± 0.08 [24 ± 1]	
9-Cl	270		20 ± 1 [52 ± 7]	7 ± 1 [10 ± 5]	0.07 ± 0.02 [40 ± 10]
	494	> 500	18.6 ± 0.5 [91 ± 5]	6 ± 2 [9 ± 4]	
+ 30% sucrose	270		17.4 ± 0.9 [43 ± 6]	8 ± 3 [6 ± 5]	0.060 ± 0.005 [52 ± 4]
	494	> 500	17.8 ± 0.6 [91 ± 6]	6 ± 3 [8 ± 6]	

[a] $1/\tau_4$ is a measure of post-cleavage processes: HPD rebinding at 487 nm (see Appendix III) or enzymatic and non-enzymatic HPD ketonization at 270 nm. Note that there is a considerable amount of uncertainty in these measurements (reflected in the standard deviation between measurements) as the experiments were designed to investigate the pre-steady-state catalytic events

ES^{red} was characterized by a λ_{max} at 472 nm and a rate constant of ~312 s^{-1} was measured (Figure 32A and E). Subsequently, the ketonization reaction occurred at ~2.8 s^{-1}, which was apparent from the kinetic traces at both 472 and 270 nm. For the remaining substrates, an additional relaxation event was observed after formation of ES^{red}. The red-shifted intermediates, which all accumulated within or near the dead-time of the instrument ($1/\tau_1 \geq$ 500 s^{-1}) were defined by λ_{max} values at 485, 472 and 494 nm for 5,8-diF, 8-Cl and 9-Cl HOPDA, respectively (Figure 32B-D).

For 5,8-diF HOPDA, biphasic decay of ES^{red} was not coupled to a biphasic increase in the absorbance at 270 nm (Figure 32F). Instead, a small decrease in the signal at 485 nm, accounting for only 2.3% of the total change in amplitude suggested that the two initial relaxation processes corresponded to substrate destabilization. The final observable phase, $1/\tau_3$ ~0.13 s^{-1} at 270 nm, matched the k_{cat} value, indicating that ketonization rather than deacylation limited the hydrolysis of 5,8-diF HOPDA.

The turnover of 8-Cl and 9-Cl HOPDA was also triphasic (Figure 32G and E), including the biphasic decay of ES^{red} accompanied by HPD formation, reminiscent of the two distinct acylation events proposed for $BphD_{LB400}$[81]. Thus, ketonization of 8-Cl HOPDA proceeded at 4.3 and 1.0 s^{-1} ($1/\tau_2$ and $1/\tau_3$) whereas deacylation occurred at ~0.48 s^{-1} [39]. The corresponding rate constants associated with ketonization of 9-Cl HOPDA were faster, 20 s^{-1} and 7 s^{-1}, and considering that $1/\tau_3$ was commensurate with k_{cat}, the results suggested that this process may be rate-limiting even for more basic substrates. The assignment of the final observable phase to a chemical event was supported by repetition of the reaction of DxnB2 and 9-Cl HOPDA in the presence of 30% sucrose (w/v). The viscogen did not perturb the reaction under single turnover conditions. Finally, the biphasic nature of ES^{red} decay and

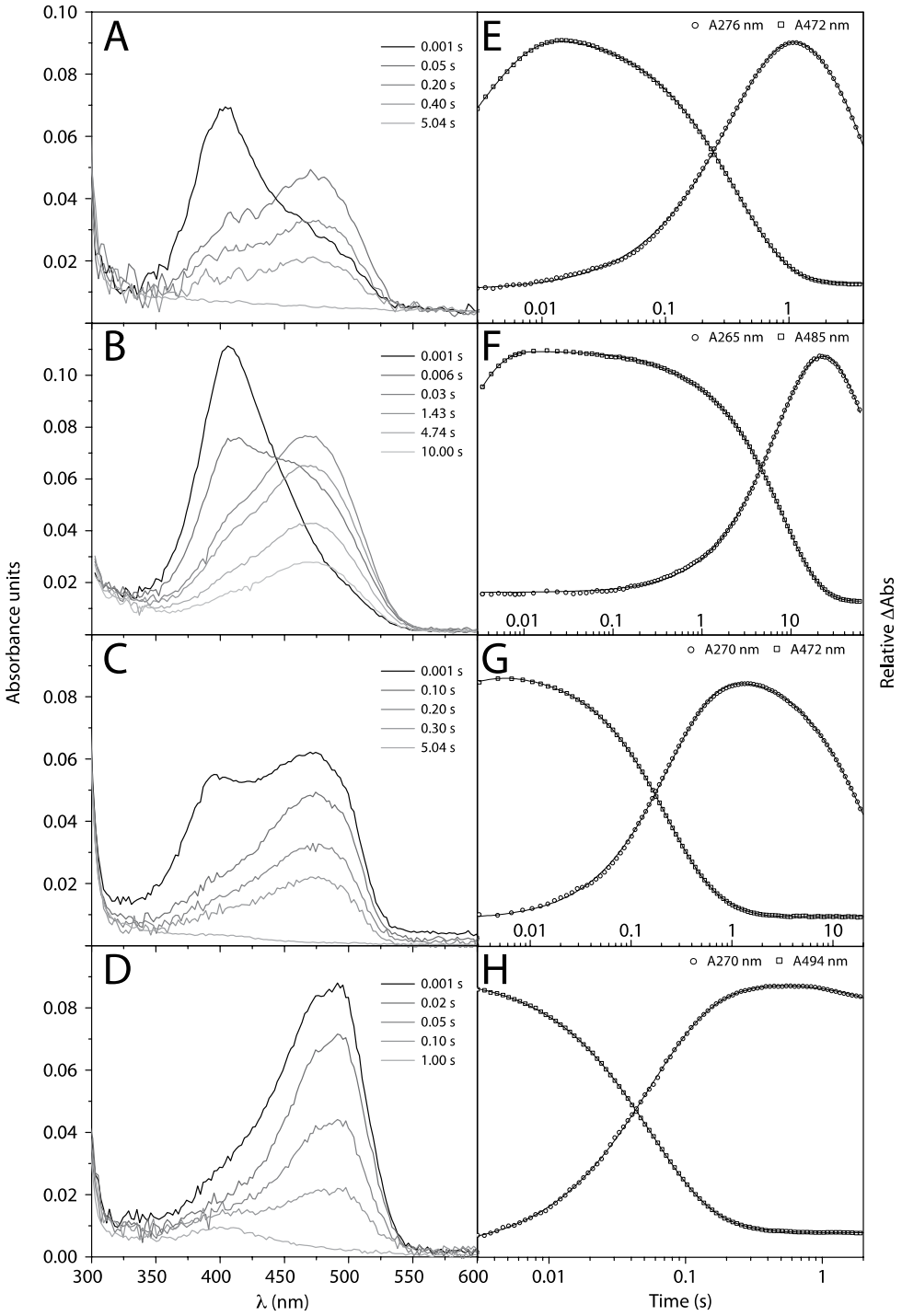

Figure 32. Representative stopped-flow experiments monitoring the turnover of 4 μM substrate by 16 μM DxnB2: (A/E) 5-Cl , (B/F) 5,8-diF , (C/G) 8-Cl and (D/H) 9-Cl HOPDA.

the sub-stiochiometric burst of product formation from 9-Cl HOPDA prompted the hypothesis that the ring-substituents may be determinants that invoke half-site reactivity in DxnB2.

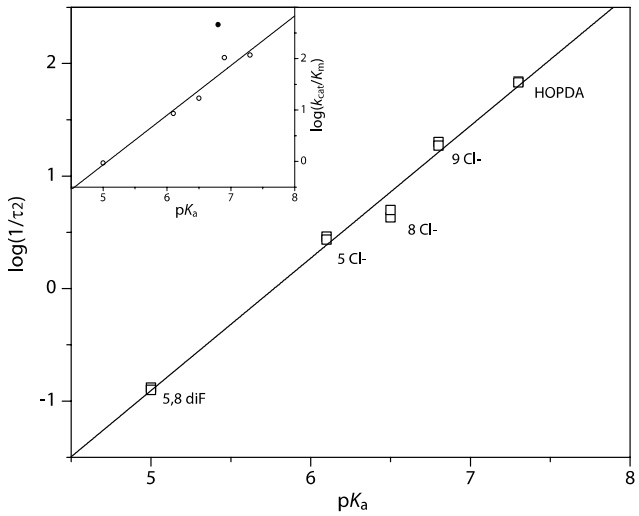

Figure 33. Extended Brønsted relationship of substrate basicity and $1/\tau_2$ or k_{cat}/K_m (*inset*; k_{cat}/K_m values were reported in [39], including 10-Cl HOPDA, which was not investigated in this work).

A plot of the experimentally observed pK_{a2} values of each substrate against the $\log(1/\tau_2)$, demonstrated a positive linear correlation ($R^2 = 0.97$). Thus, the extended Brønsted analysis revealed that the ketonization reaction was sensitive to the nucleophilicity of the substrate, $\beta_{nuc} = 1.17 \pm 0.06$ (Figure 33). Similarly, analysis of the steady-state specificity constants (k_{cat}/K_m) for the DxnB2 hydrolysis of substituted HOPDAs showed a positive correlation ($R^2 = 0.96$) and $\beta_{nuc} = 1.0 \pm 0.1$. 9-Cl HOPDA was excluded from the latter analysis since the C9-substitutent provided an additional substrate specificity determinant compared to all other tested substrates. The sensitivity of the reaction to the basicity of the substrate is consistent with the proposed substrate-assisted mechanism of nucleophile activation in the MCP hydrolases. Considering only the analysis on $1/\tau_2$, the more basic

substrates are more reactive towards an incipient proton and, therefore, are more readily ketonized. Along these lines, the more acidic substrates are better suited to stabilize the negative charge on the enzyme-bound dianionic dienoate moiety of ES^{red}. For 5,8-diF HOPDA, the most extreme case reported herein, the rate of substrate ketonization is rate-determining, a consequence of the stability of ES^{red}.

3.3.6 Probing the electronic nature of ES^{red} by NMR

Despite the relevance of ES^{red} to catalysis, the identity of this intermediate is unknown. In an attempt to characterize ES^{red}, a uniformly labeled ^{13}C-HOPDA was generated by enzymatic transformation of ^{13}C-biphenyl by BphAEFG, BphB and BphC. The identities of individual carbons in the DxnB2 S105A:HOPDA complex were not assigned. Overall, the signals originating from HOPDA, whether free in solution or in complex to DxnB2 S105A, were observed over a similar chemical shift range (Figure 56, Appendix IV). Unfortunately, most of these broad signals occur within 1 ppm and 10 ppm in the ^{1}H and ^{13}C dimension, respectively. Instead, the ability of DxnB2 to hydrolyze fluorinated HOPDAs in a manner that resembled turnover of the unsubstituted substrate provided an opportunity to probe the electronic nature of this intermediate via the ^{19}F nuclei. Moreover, the ^{19}F signals could be definitively assigned through comparing the NMR spectra of 8-F and 5,8-diF HOPDA. Accordingly, 8-F and 5,8-diF HOPDAs were prepared and complexed to DxnB2 S105A. ^{19}F NMR spectra of the solutions containing 400 μM DxnB2 and 200 μM 8-F or 5,8-diF HOPDA were compared to those of the free substrates (Figure 34) and model fluorine-containing compounds (Table 13). Interestingly, the ^{19}F nuclei of 5,8-diF HOPDA were degenerate in solution whereas binding to DxnB2 S105A resulted in the appearance of a second signal at -157.71 ppm. The latter was assigned to C5-F based on the signal observed

from S105A:8-F HOPDA binary complex. For 8-F HOPDA, the enzyme effectively inverted the population of the major and minor species in solution. Relative to the model 2-fluorophenyl ketones, the observed -40.6 ppm shift of C5-F placed the observed species closer to the sp^3- than the sp^2-hybridized analog. In spite of this, a definitive assignment of the hybridization state of C5 in the S105A:5,8-diF HOPDA is not possible considering the broad and overlapping range of ^{19}F chemical shifts associated with atoms connected to sp^2 and sp^3-hydbrized carbon centers and the sensitivity of the ^{19}F to distinct environments.

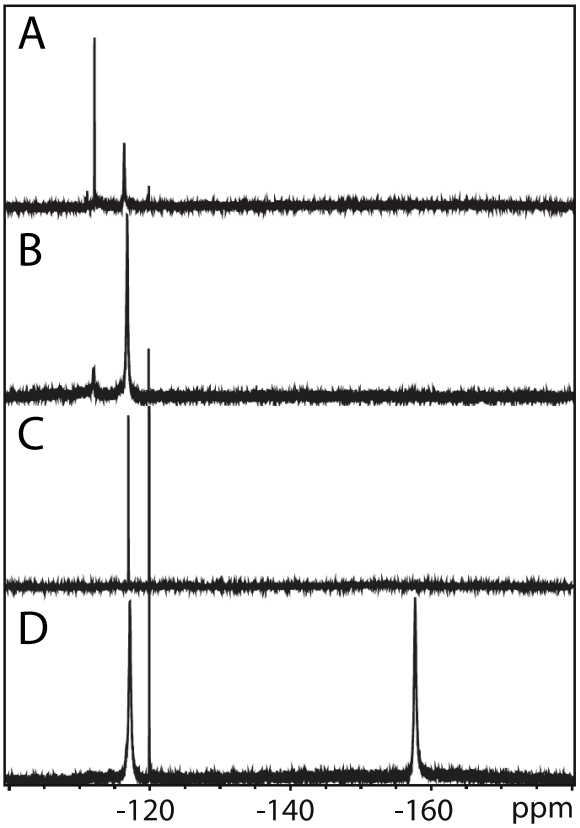

Figure 34. ^{19}F NMR spectra of (A) 200 μM 8-F HOPDA, (B) 200 μM 8-F HOPDA in complex with 400 μM DxnB2 S105A, (C) 200 μM 5,8-diF HOPDA and (D) 200 μM 5,8-diF HOPDA in complex with 400 μM DxnB2 S105A in KPi (I = 0.1 M), pH 7.5 at 25 °C.

Table 13. ^{19}F chemical shifts observed in KPi (I = 0.1 M), pH 7.5 at 25 °C.

Sample	^{19}F chemical shift (ppm)
2-fluorophenylpropanone	-184.32 (minor) and -185.13 (major)
2-fluorophenylprop-2-enone	-111.73 (major), -116.46 (minor), -111.00 (minor)
8-F HOPDA	-116.86 (minor), -111.00 (major)
S105A:8-F HOPDA	-116.79 (major), -112.04 (minor)
5,8-diF HOPDA	-116.96
S105A:5,8-diF HOPDA	-117.17 and -157.71

3.3.7 Probing the reactivity of ES^{red} with molecular oxygen

Enzymes that mediate carbanion chemistry must protect their reactive species in order to prevent non-specific catalysis. In particular, the reaction media almost always contains undesired electrophiles such as molecular oxygen. Accordingly, the relative ability of enzymes to protect their carbanionic intermediates can be surveyed by monitoring O_2-consuming side-reactions[116]. In light of the substrate-assisted proposal for nucleophile activation and the extended lifetime of ES^{red} in the catalytic serine variants, the O_2-sensitivity of a DxnB2 S105A:HOPDA binary complex was tested. The half-life ($t_{1/2}$) of ES^{red} was measured spectrophotometrically as a function of O_2 concentration. Binary complexes were prepared at 650 μM, 280 μM or ~0.5 μM O_2 (≤ 5 ppm) in KPi (I = 0.1 M), pH 7.5 at 25 °C. Interestingly, added O_2 resulted in a 3.4-fold decrease in the $t_{1/2}$ of ES^{red}, which was measured to be 1.8 ± 0.2 and 6.2 ± 0.1 h at 650 and 280 μM O_2, respectively. In the absence of oxygen, the $t_{1/2}$ of ES^{red} could not be modeled by a single exponential decay function. Instead, the $t_{1/2}$ was estimated to be 26 ± 2 h based on a single time point at which three quarters of starting absorbance remained.

To further assess the reactivity of O_2 with ES^{red}, the benzoyl-containing ES^{red} decay products were analyzed by EI GC/MS. Benzoate was observed as the major decay product of

ES^{red} after incubation overnight at ambient O_2. Next, the products from the decay of 9-Cl HOPDA or a DxnB2 S105A:9-Cl HOPDA binary complex in a solution of KPi (I = 0.1 M), pH 7.5, saturated with O_2 (~1 mM) were analyzed by EI GC/MS. It was rationalized that the natural abundance of the ^{35}Cl and ^{37}Cl isotopes could be used to guide the tentative assignment of any minor ES^{red} or 9-Cl HOPDA decay products. Inspection of the chromatograms from the decay of ES^{red} to that of a sample of 9-Cl HOPDA alone, revealed an additional DxnB2 S105A-associated product. This 3-chlorobenzoyl-containing product was defined by an R_t of 21.8 minutes and an m/z value of 241 (Figure 35). Strikingly, the 241 m/z product was produced at a 1:8 ratio to 3-chlorobenzoate (R_t 17.8 min; 228 m/z), which constituted the major decay product from the S105A:9-Cl HOPDA complex. The observed mass relative to 3-chlorobenzoate, M+13, is consistent with a compound possessing an additional C atom and H atom. This product has been provisionally assigned as 1-(3-chlorophenyl)-2-hydroxyethanone, which may result from an O_2-consuming side reaction. Nevertheless, $^{18}O_2$ and $H_2{}^{18}O$ isotope studies are required to identify the source of the oxygen atoms in the observed products and higher resolution experiments are required for the unambiguous assignment of the atomic mass for the newly identified 241 m/z product.

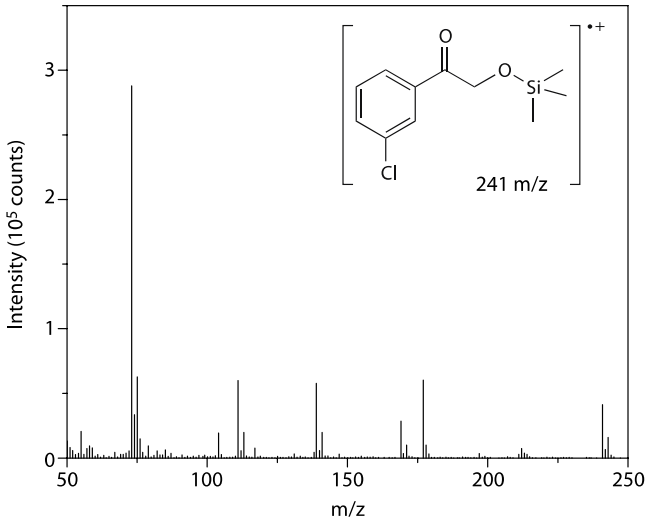

Figure 35. Mass spectrum of the O_2-dependent ES^{red} breakdown product. The chemical structure of a compound with a theoretical m/z value of 241 m/z is inset.

3.4 Characterization of DxnB2 P-subsite and His255 variants

3.4.1 Steady-state kinetic analysis of P-subsite and His255 variants

To help elucidate the role of the P-subsite and His255 in catalysis, a series of DxnB2 variants were generated that covered a relatively broad range of steric and electronic substitutions: Asn43 was substituted with each of Ala, Asp and His; Arg180 was replaced with each of Gln, Lys and Met; and His255 with each of Ala, Asp and Gln. P-subsite variants were characterized by a relatively wide range of steady-state kinetic parameters. In contrast, the His variants resembled those observed in other MCP hydrolases; the substitution of His255 in DxnB2 to Ala, Gln or Glu resulted in severely compromised enzymes. Steady-state turnover rate constants ($v_0/[E]_T$) estimated from v_0 measurements of the turnover of 20 μM HOPDA or 9-Cl HOPDA by each His255 variant ranged between 0.0001 and 0.002 s^{-1} (Table 14).

Table 14. The hydrolytic activity of DxnB2 His255 variants

Enzyme	20 μM HOPDA $v_0/[E]_t$ (s^{-1})	20 μM 9-Cl HOPDA $v_0/[E]_t$ (s^{-1})
H265A	0.00019 ± 0.00002	0.00032 ± 0.00007
H255E	0.00066 ± 0.00006	0.0015 ± 0.0004
H255Q	0.00011 ± 0.00003	0.00026 ± 0.00009

For the P-subsite variants, v_0 data was measured by varying the concentration of HOPDA or 9-Cl HOPDA from 0.5 to 50 μM or from 10 to 200 μM, depending on the enzyme under investigation. Steady-state kinetic parameters were obtained from plots of v_0 versus substrate concentration fit with either the Michaelis-Menten or substrate inhibition equation (Appendix V). As summarized in Table 15, all of the variant possessed greater specificity for 9-Cl HOPDA, a characteristic shared with the WT enzyme. However, the variants showed one of two kinetic behaviours. The first group, N43A, N43H and R180K, was similar to the WT in that each was subject to substrate inhibition. Nevertheless, the observed inhibition was lesser in variants and for substituted HOPDAs. For example, the N43H variant was inhibited by HOPDA but not 9-Cl HOPDA, and the effects of the N43A, N43H and R180K substitutions on K_{si} varied between a 1.7 to 50-fold relative to the WT. Along with sharing kinetic behaviour with the WT enzyme, these variants were the most active towards the substrates with k_{cat}/K_m values determined between 10^4 and 10^5 $M^{-1}s^{-1}$.

The second group of variants, N43D, R180M and R180Q, were defined by the lack of substrate inhibition and significantly greater K_m values (> 100-fold). Remarkably, for both HOPDA and 9-Cl HOPDA the K_m increased by up to three orders of magnitude whereas the k_{cat} values were typically within an order of magnitude the WT-catalyzed reaction. Taken together, these steady-state kinetic results emphasize the importance of the P-subsite for catalysis and implicate the P-subsite as a determinant for substrate inhibition in DxnB2.

Table 15. Steady-state kinetic parameters of DxnB2 P-subsite variants for HOPDA and 9-Cl HOPDA[a,b]

	HOPDA				9-Cl HOPDA			
	k_{cat} (s^{-1})	K_m (μM)	k_{cat}/K_m ($10^5\ M^{-1}\ s^{-1}$)	K_{si} (μM)	k_{cat} (s^{-1})	K_m (μM)	k_{cat}/K_m ($10^5\ M^{-1}\ s^{-1}$)	K_{si} (μM)
WT[c]	0.47 ± 0.02	0.039 ± 0.006	120 ± 40	37 ± 8	5.1 ± 0.6	0.11 ± 0.04	500 ± 100	6 ± 2
N43A	0.12 ± 0.01	0.25 ± 0.03	4.9 ± 0.5	63 ± 7	0.85 ± 0.02	0.19 ± 0.03	46 ± 6	190 ± 40
N43D	0.045 ± 0.002	57 ± 4	0.0079 ± 0.0003	NA	0.45 ± 0.01	39 ± 4	0.115 ± 0.007	NA
N43H	0.023 ± 0.001	1.00 ± 0.07	0.23 ± 0.01	90 ± 10	0.077 ± 0.001	0.28 ± 0.03	2.8 ± 0.3	NA
R180K	0.31 ± 0.01	1.26 ± 0.09	2.5 ± 0.1	130 ± 20	2.36 ± 0.05	0.37 ± 0.03	63 ± 5	280 ± 8
R180M	0.022 ± 0.001	76 ± 9	0.0029 ± 0.0002	NA	0.98 ± 0.01	190 ± 30	0.053 ± 0.003	NA
R180Q	0.035 ± 0.001	64 ± 4	0.0054 ± 0.0002	NA	1.17 ± 0.04	94 ± 7	0.124 ± 0.006	NA

[a]Apparent K_m and k_{cat}/K_m values for enzymes in which K_m < 1 μM [b]The complete set of steady-state kinetic curves for the P-subsite variants are available in Appedix V. [c]Values for the WT enzyme were taken from [39].

3.4.2 Investigating the ability of P-subsite and His255 variants to accumulate ES^{red}

While sequence conservation and steady-state kinetic data have implicated the P-subsite in catalysis, the specific roles of these residues remain unknown. To study the role of Asn43, Arg180 and His255 in substrate binding and destabilization (ES^{red} formation), each residue was mutated in a DxnB2 S105A background. The electronic absorption spectra of ES complexes were measured in KPi (I = 0.1 M), pH 7.5 at 25 °C. Both HOPDA and 9-Cl HOPDA were examined (Figure 36). In nearly all the complexes, at least a small population of ES^{red} was observed. The replacement of Arg180 with a neutral amino acid appeared to have the most deleterious effect on substrate destabilization. For HOPDA, no red-shifted species was observed at 4E:1S, and only a very small population was observed for 9-Cl HOPDA in solution with the S105A/R180M and S105A/R180Q variants. Moreover, these variants appeared to stabilize the enol form of the substrates, possessing a maximal absorbance near 340 and 350 nm for HOPDA and 9-Cl HOPDA, respectively. Finally, an unidentified species characterized by a λ_{max} between 400 to 420 nm was observed for 9-Cl HOPDA in complex with the S105A/R180M, S105A/R180Q and S105A/H255E variants. Although the electronic nature of this species is unknown, absorption at wavelengths greater than 390 nm is typically associated with dianionic HOPDA isomers (Appendix I). The ability of each P-subsite variant to at least partially stabilize some red-shifted species suggests that each residue contributes to substrate destabilization.

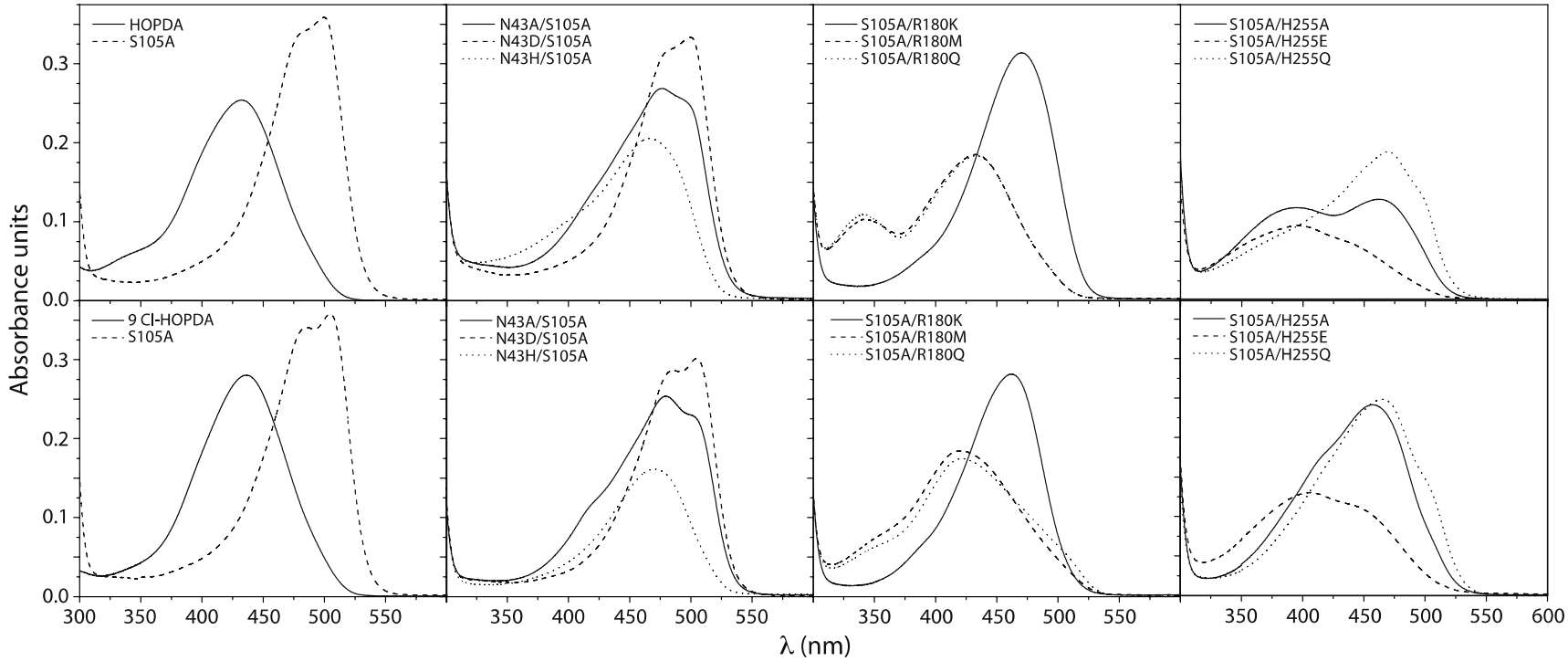

Figure 36. Perturbations to the electronic absorption spectra observed upon mixing 40 μM enzyme with 10 μM HOPDA (top) or 10 μM 9-Cl HOPDA (bottom)

3.4.3 K_d Determinations

The observed spectral perturbations observed at 4E:1S was further exploited to determine dissociation constants for HOPDA and 9-Cl HOPDA to key DxnB2 variants. The enzymes with high K_m values, N43D/S105A, S105A/R180M and S105A/R180Q were of particular interest in order to delineate the deleterious effects associated with altered substrate binding or chemistry. Thus, enzymes were titrated into a solution of either 4 μM HOPDA or 3 mM 9-Cl HOPDA in KPi (I= 0.1 M), pH 7.5 at 25 °C. Electronic absorption spectra were recorded upon each successive addition of enzyme, and difference spectra were used to determine the dissociation constants from fitting either hyperbolic or quadratic binding equations to plots of ΔAbs versus enzyme concentration (Appendix V). The assay was not sensitive enough to determine $K_{d\ HOPDA}$ or $K_{d\ 9\text{-}Cl\ HOPDA}$ from the N43D/S105A variant. An upper bound for the K_d in both cases was set at 20 nM (Figure 59, Appendix V), suggesting that the high K_m value determined for the N43D variant reflected a deficiency in chemistry rather than affinity for the substrates. Alternatively, the dissociation constants for S105A/R180Q and especially S105A/R180M indicated that poor substrate binding contributed significantly to the reduced hydrolytic activity of the R180M and R180Q variants (Table 16 and Figure 37). At least two distinct species were observed from complexes of HOPDA and S105A/R180M or S105A/R180Q (Figure 19D). Up to four electronic transitions were observed from complexes of 9-Cl HOPDA and S105A/R180M or S105A/R180Q (Figure 19C). For HOPDA, the variants perturbed the enol:enolate equilibrium with a prominent species at ~340 nm appearing with the addition of enzymes. For the 9-Cl HOPDA complexes, a blue-shifted species possessing the highest absorptivity was centered between 400 and 410 nm, and an enol form of the substrate was also apparent

(λ_{max} ~350 nm). Interestingly, despite the replacement of Arg180 with uncharged residues, a small population of ES^{red} was still observed.

Table 16. K_d for DxnB2 S105A/R180M and S105A/R180Q:HOPDA complexes

Enzyme	Δλ (nm)	K_d HOPDA (μM)	Δλ (nm)	K_d 9-Cl HOPDA (μM)
S105A/R180M	337	140 ± 20	350	180 ± 30
S105A/R180Q	337	52 ± 2	512	14 ± 2

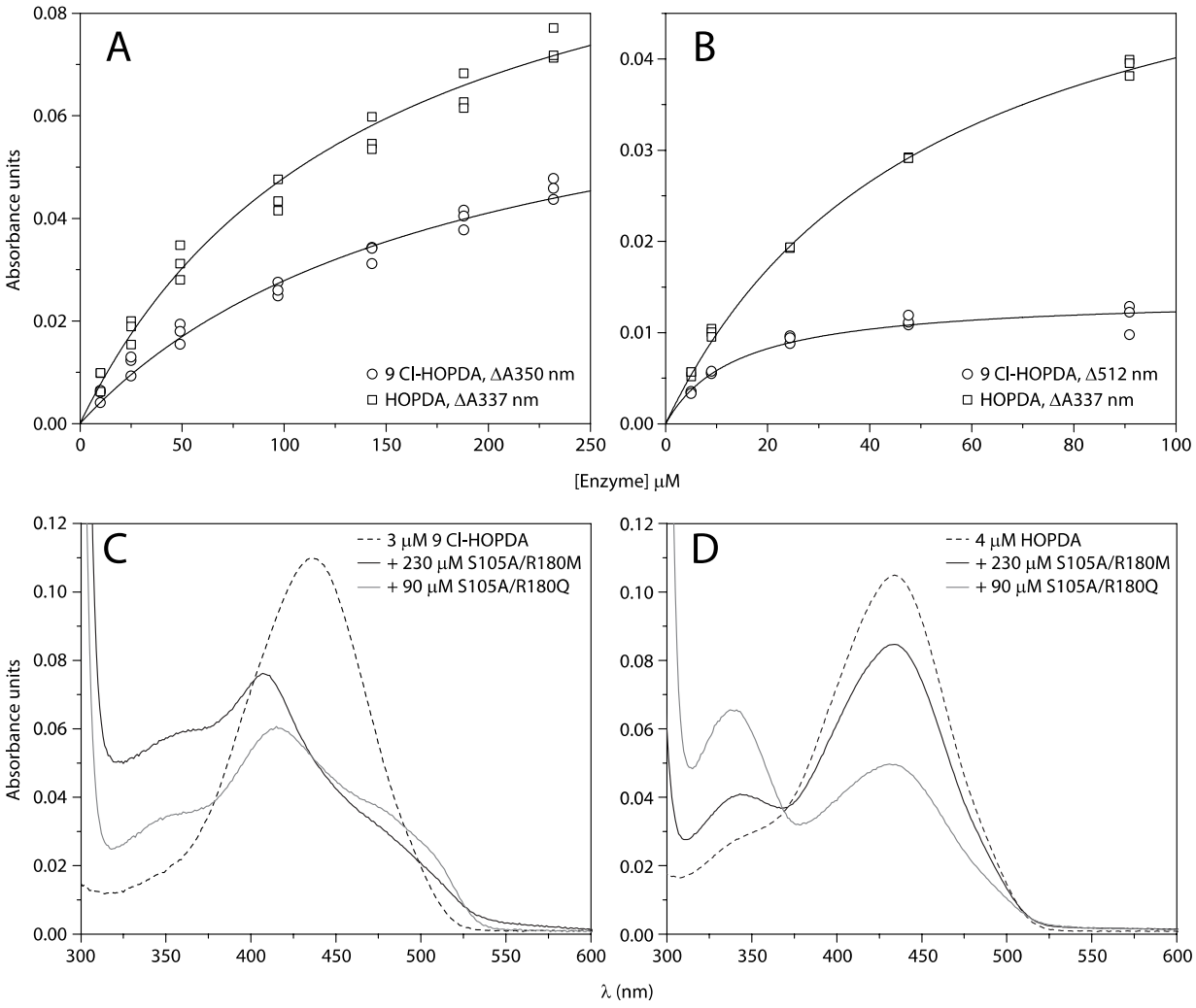

Figure 37. Titration of 4 μM HOPDA or 3 μM 9-Cl HOPDA with (A) DxnB2 S105A/R180M and (B) S105A/R180Q. (C) The spectra of 3 μM 9-Cl HOPDA (dashed lines) before and after titration with DxnB2 S105A/R180M (black) or S105A/R180Q (grey). (D) The spectra of 4 μM HOPDA before and after titration with DxnB2 S105A/R180M or S105A/R180Q.

3.4.4 Single turnover of HOPDA and 9-Cl HOPDA by P-subsite variants

Each of the P-subsite variants perturbed the substrate in a distinct manner. In order to determine the catalytic relevance of these perturbations, the single turnover of HOPDA and 9-Cl HOPDA by each variant was examined. DxnB2 R180M and R180Q were excluded from this analysis since the corresponding variants in the S105A background possessed significantly reduced substrate affinity. Reactions of 16 μM enzyme with 4 μM substrate in KPi (I = 0.1 M), pH 7.5 at 25 °C, were first monitored using a PDA detector in order to identify relevant intermediates (Figure 38 and 39A-D). In contrast to the observations in the S105A/P-subsite double variants, a red-shifted intermediate was only detected during turnover by DxnB2 N43H.

Following the detection of catalytic intermediates, reactions were monitored at 270 nm and the λ_{max} of the enolate or, in the case of N43H, a red-shifted wavelength, 453 and 455 nm for the turnover of HOPDA and 9-Cl HOPDA, respectively (Figures 38 and 39 E-H; Table 17). For some reactions, a small and rapid spectral perturbation, $1/\tau_1$ ranging from 6 to 150 s^{-1}, preceded enolate decay assigned here to substrate ketonization based on the ability to monitored changes at both stated wavelengths. A third, post-reaction relaxation, associated with HPD ketonization could also be observed at 270 nm. However, the accuracy in defining this phase was almost always limited by the timescale of the experiments (designed to capture early catalytic events). Notably, the rate constants for substrate ketonization, $1/\tau_2$, matched the k_{cat} values determined for the N43H variant as well as that for the R180K turnover of 9-Cl HOPDA. Under single turnover conditions, the N43D enzymes were consistently 4-fold slower than under steady-state conditions. The rate constant for ES^{red} decay rather than formation limited substrate ketonization in the N43H variant. Indeed, the

most common effect of perturbing the P-subsite was the generation of an enzyme in which ES^{red} formation was rate-limiting, characterized by its absence from kinetic traces, as previously described for the $BphD_{LB400}$-mediated turnover of recalcitrant PCB metabolites[86] or the activity associated with the His265 variants[66].

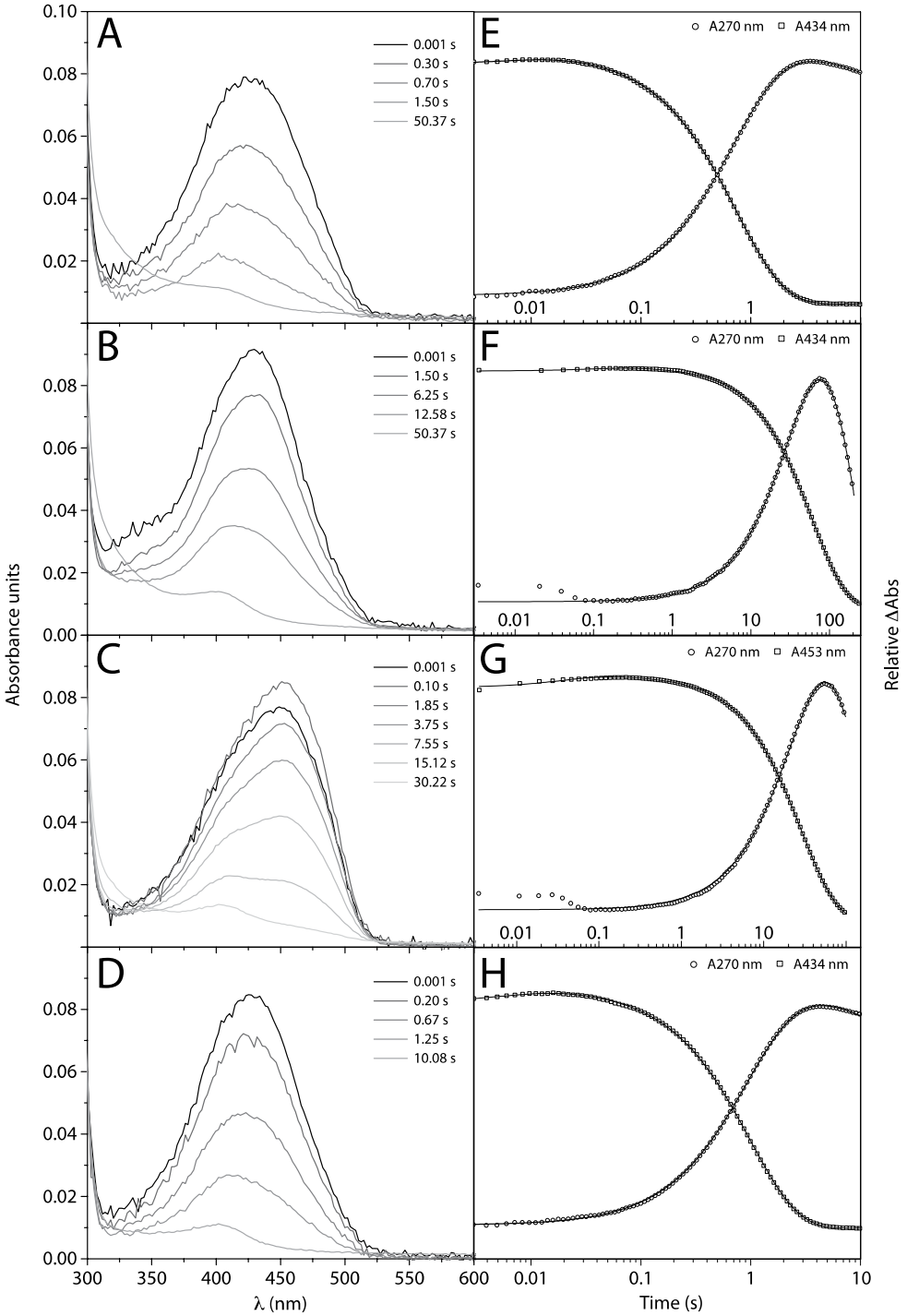

Figure 38. Results from representative stopped-flow experiments demonstrating the turnover of 4 μM HOPDA by 16 μM DxnB2 P-subsite variant: (A/E) N43A, (B/F) N34D, (C/G) N43H and (D/H) R180K. (A/E) N43A, (B/F) N34D, (C/G) N43H and (D/H) R180K. For clarity, selected traces showing the progress of the reaction between 300 and 600 nm are shown, and 1/10 data points are shown in the plots of relative ΔAbs versus time.

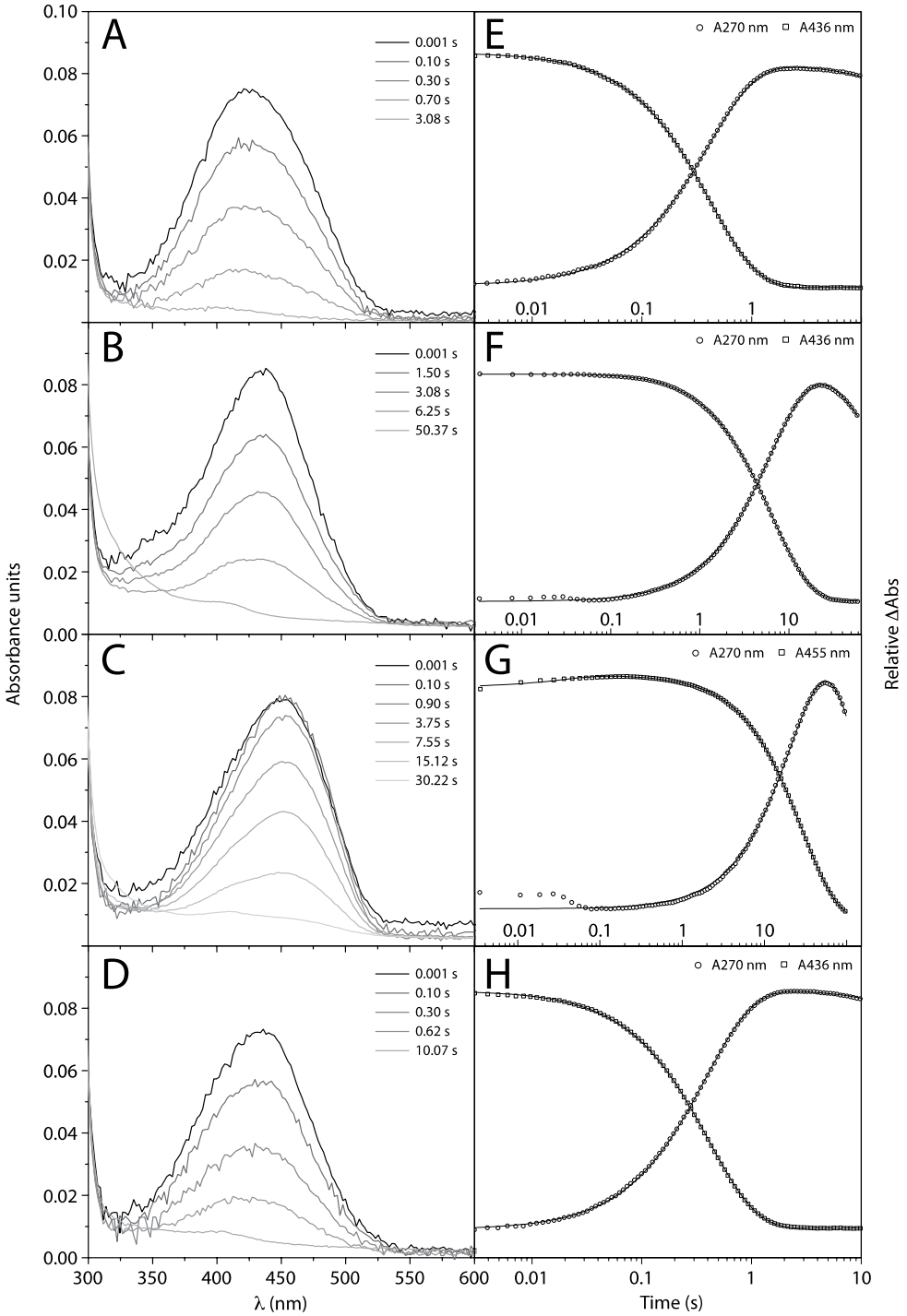

Figure 39. Results from representative stopped-flow experiments demonstrating the turnover of 4 μM 9-Cl HOPDA by 16 μM DxnB2 P-subsite variant: (A/E) N43A, (B/F) N34D, (C/G) N43H and (D/H) R180K. (A/E) N43A, (B/F) N34D, (C/G) N43H and (D/H) R180K. For clarity, selected traces showing the progress of the reaction between 300 and 600 nm are shown, and 1/10 data points are shown in the plots of relative ΔAbs versus time

Table 17. Kinetic data for HOPDA and 9-Cl HOPDA turnover by P-subsite variants

	λ	HOPDA					
DxnB2	(nm)	$1/\tau_1$ (s^{-1})	[%Amp]	$1/\tau_2$ (s^{-1})	[%Amp]	$1/\tau_3$ (s^{-1})	[%Amp]
N43A	270			1.3 ± 0.1	[79 ± 5]	0.3 ± 0.2	[29 ± 9]
	434	120 ± 20	[4.6 ± 0.1]	1.33 ± 0.01	[95 ± 1]		
N43D	270			0.019 ± 0.001	[45 ± 3]	0.08 ± 0.01	[55 ± 1]
	434	6 ± 2	[1.2 ± 5]	0.017 ± 0.001	[99 ± 1]		
N43H	270			0.026 ± 0.001	[50 ± 10]	0.013 ± 0.002	[50 ± 10]
	453	29 ± 4	[4.9 ± 0.2]	0.035 ± 0.001	[95 ± 1]		
R180K	270			1.09 ± 0.04			
	434	110 ± 40	[5.7 ± 0.3]	1.01 ± 0.02			
				9-Cl HOPDA			
N43A	270			2.40 ± 0.07			
	436			2.38 ± 0.02			
N43D	270			0.149 ± 0.004	[49 ± 1]	0.006 ± 0.004	[50 ± 20]
	436	9 ± 1	[2.2 ± 0.4]	0.152 ± 0.002	[97 ± 1]		
N43H	270			0.062 ± 0.004	[56 ± 5]	0.011 ± 0.004	[44 ± 1]
	455	150 ± 50	[6.1 ± 0.2]	0.069 ± 0.001	[94 ± 1]		
R180K	270			2.53 ± 0.08			
	436			2.42 ± 0.02			

3.4.5 Single turnover of HOPDA and 9-Cl HOPDA by the His255 variants

The accumulation of red-shifted intermediates in DxnB2 S105A/H255 variants contrasts with what was reported for $BphD_{LB400}$ S112A/H265 variants, which stabilized the HOPDA enolate dianion in an apparently planar conformation[66]. Stopped-flow experiments were used to measure the rate of a single turnover of HOPDA or 9-Cl HOPDA by the DxnB2 His255 variants in KPi (I = 0.1 M), pH 7.5 at 25 °C. Detection of reaction intermediates using a PDA indicated that only the H255A and H255Q variants accumulated detectable quantities of a red-shifted species (Figure 40 and 41A-C). Although the rate constants for the turnover of the substrates by each enzyme were similar (Table 18), the spectroscopic changes that were observed during the turnover of 9-Cl HOPDA were more pronounced, again reflecting the additional determinant of specificity carried by the

substitution at C9.

The spectra of the HOPDA species observed during the H255A-mediated turnover were bathochromically-shifted by up to 40 nm. For both substrates, the electronic absorption spectrum was complex, containing at least three spectroscopically distinct species throughout the single turnover. For HOPDA, the λ_{max} of ES^{red} was near 450 nm. However, a series of overlapping bands gave rise to a relatively broad signal between 375 to 525 nm. For 9-Cl HOPDA, the ES^{red} λ_{max} was better defined at 457 nm. Upon formation of ES^{red}, the signal decayed at 0.5 and 0.2 s^{-1} for HOPDA and 9-Cl HOPDA, respectively, with a concomitant increase in the absorbance at 270 nm. In either case, this represented an ~100-fold reduction compared to the WT enzymes but was ~1000-fold faster than the steady-state rate constant for H255A turnover, ~0.0002 or ~0.0003 s^{-1} of HOPDA or 9-Cl HOPDA, respectively.

The absence of ES^{red} from the kinetic traces of H255E-catalyzed reactions indicated that the formation of this intermediate limits the rate of ketonization and acylation in this enzyme. Moreover, the rate of ES^{red} formation likely contributes to the steady-state rate of hydrolysis by this enzyme, which differed by only 16- or 6-fold from the measured $1/\tau_4$ values for HOPDA or 9-Cl HOPDA. Along with the absence of ES^{red}, the H255E variant apparently shifted the enol:enolate equilibrium from that observed free in solution. A detectable quantity of the enol, absorbing at ~340 nm, accumulated during the turnover of both substrates.

Among the three His255 variants, the single turnover kinetic behaviour of H255Q was the most complex, and as in the WT the two distinct substrates were hydrolyzed in a different number of observable kinetic phases. The enzyme appeared to bind a protonated form of the substrate, indicated by the first recorded spectrum, which possessed bands at 340

and 370 nm. Next, a small population of ES^{red} accumulated at 100 or 50 s^{-1} ($1/\tau_1$), which was coupled to a decrease in the absorbance attributed to the bound enol species. The latter was measured at 340 nm for HOPDA and at both 345 and 370 nm for 9-Cl HOPDA. The ES^{red} of HOPDA and 9-Cl HOPDA decayed in a mono and biphasic fashion, respectively. Nevertheless, the ketonization reaction could be modeled by single exponential process yielding rate constants of 0.036 ($1/\tau_3$) or 0.0017 s^{-1} ($1/\tau_4$) for HOPDA or 9-Cl HOPDA.

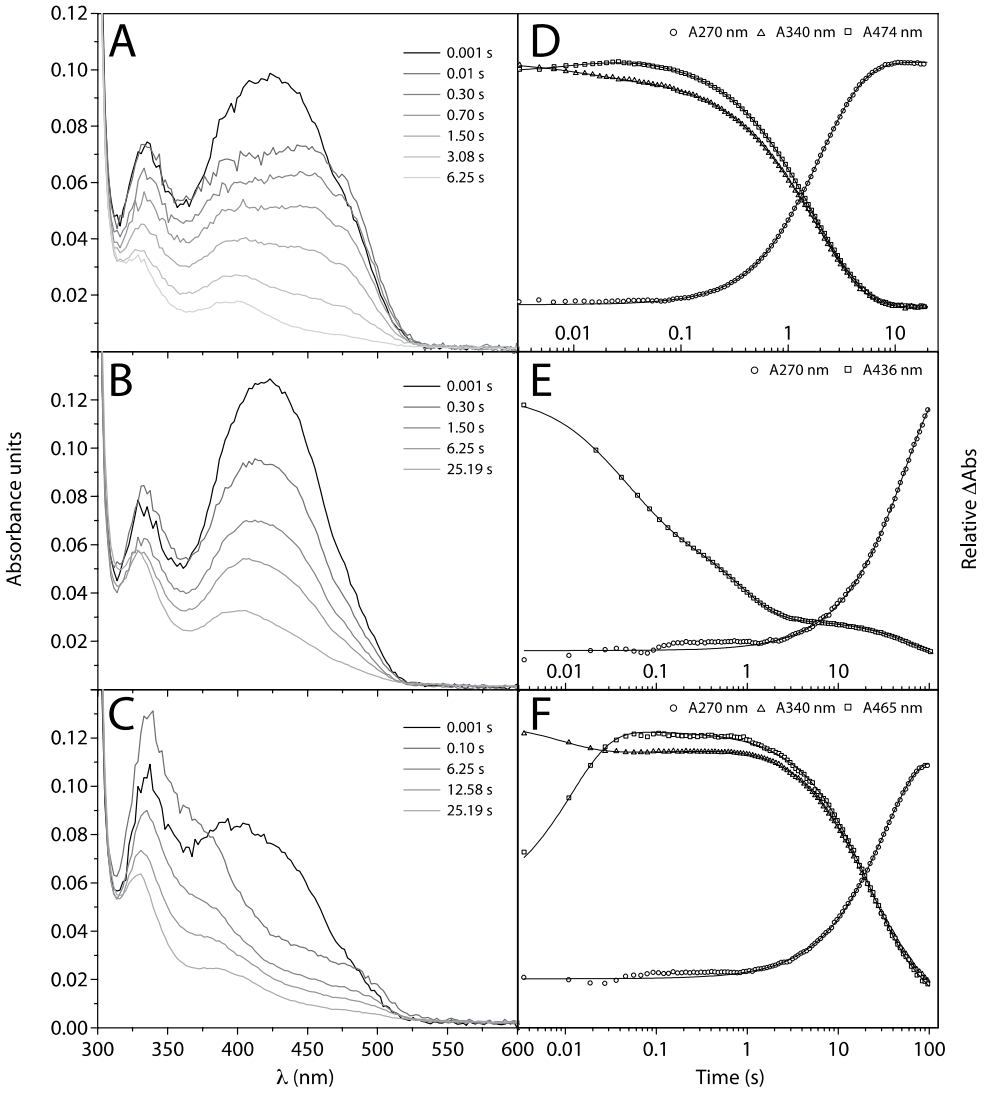

Figure 40**.** Results from representative stopped-flow experiments demonstrating the turnover of 4 μM HOPDA by 16 μM DxnB2 His255 variants: (A/D) H255A, (B/E) H255E, (C/F) H255Q. For clarity, selected traces showing the progress of the reaction between 300 and 600 nm are shown and 1/10 data points are shown in the plots of relative ΔAbs versus time.

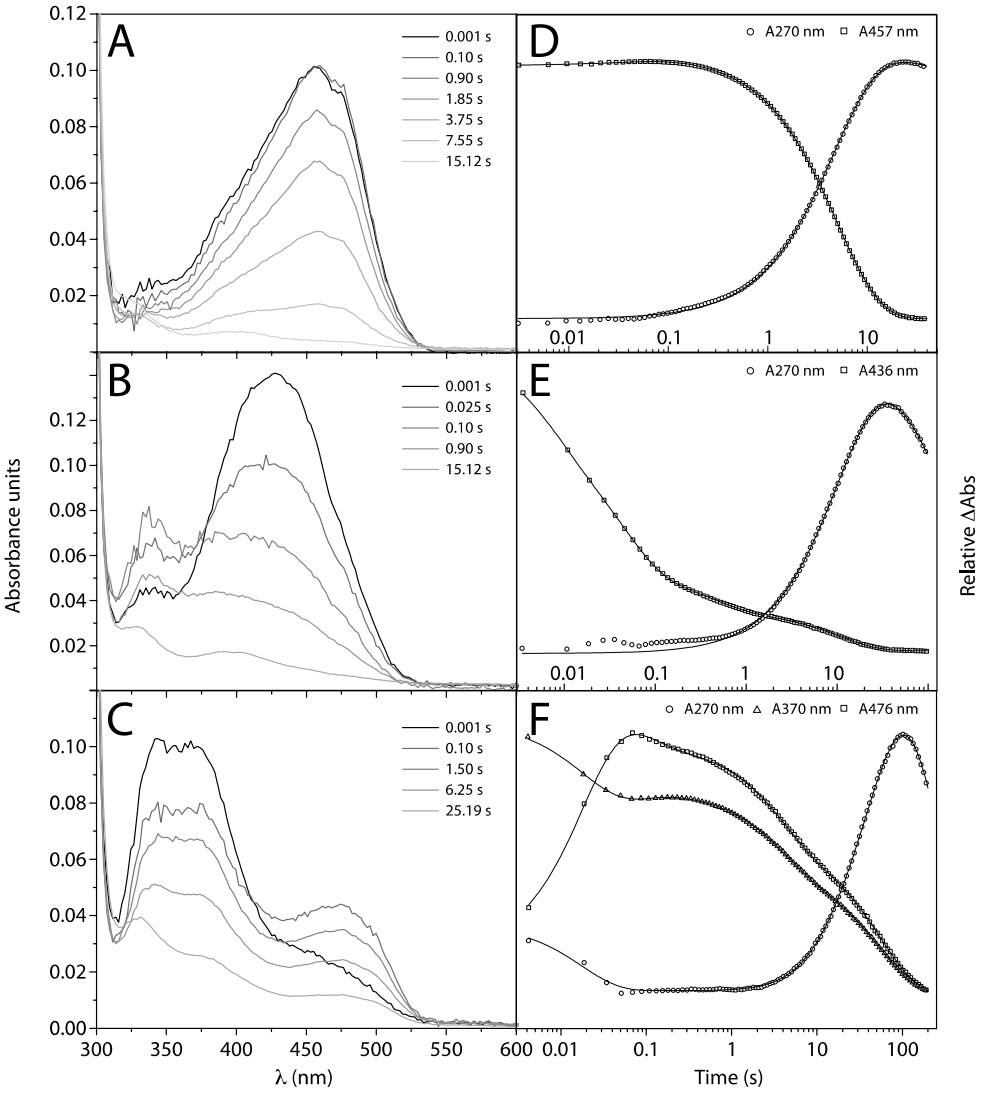

Figure 41. Results from representative stopped-flow experiments demonstrating the turnover of 4 μM 9-Cl HOPDA by 16 μM DxnB2 His255 variants: (A/D) H255A, (B/E) H255E, (C/F) H255Q. For clarity, selected traces showing the progress of the reaction between 300 and 600 nm are shown and 1/10 data points are shown in the plots of relative ΔAbs versus time.

.

Table 18. Kinetic data for HOPDA and 9-Cl HOPDA turnover by DxnB2 His255 variants[a]

DxnB2	λ (nm)	$1/\tau_1$ (s^{-1}) [%Amp]		$1/\tau_2$ (s^{-1}) [%Amp]		$1/\tau_3$ (s^{-1}) [%Amp]		$1/\tau_4$ (s^{-1}) [%Amp]	
					HOPDA				
H255A	270					0.49 ± 0.01	[79 ± 2]		
	340	120 ± 40	[7 ± 1]	1.8 ± 0.4	[12 ± 4]	0.49 ± 0.02	[81 ± 5]		
	474	70 ± 20	[6.2 ± 0.1]	1.7 ± 0.2	[13 ± 2]	0.50 ± 0.01	[81 ± 2]		
H255E	270							0.0128 ± 0.0006	[54 ± 5]
	434	70 ± 20	[19 ± 9]	14 ± 4	[30 ± 9]	1.19 ± 0.05	[37 ± 7]	0.0108 ± 0.0005	[17 ± 2]
H255Q	270					0.036 ± 0.002	[61 ± 1]		
	340	102 ± 7	[10.3 ± 0.1]	1.9 ± 0.2	[3.9 ± 0.1]	0.063 ± 0.04	[48 ± 5]	0.019 ± 0.003	[35 ± 5]
	464	90 ± 6	[35.4 ± 0.8]			0.053 ± 0.001	[59 ± 6]	0.006 ± 0.001	[25 ± 3]
					9-Cl HOPDA				
H255A	270					0.204 ± 0.005	[79 ± 2]		
	436	19 ± 2	[5.1 ± 0.7]			0.202 ± 0.002	[95 ± 1]		
	457	18 ± 3	[3.5 ± 0.3]			0.203 ± 0.003	[96.5 ± 0.3]		
	474	17 ± 4	[2.8 ± 0.6]			0.203 ± 0.001	[97 ± 1]		
H255E	270							0.0088 ± 0.006	[51 ± 1]
	436	140 ± 30	[32 ± 4]	21 ± 2	[42 ± 6]	2.2 ± 0.3	[13 ± 1]	0.096 ± 0.003	[13.1 ± 0.3]
H255Q	270	40 ± 10	[4.4 ± 0.8]			0.33 ± 0.02	[1.4 ± 0.2]	0.016 ± 0.001	[50.1 ± 0.7]
	345	49 ± 2	[29 ± 2]	15 ± 2	[9 ± 1]	0.259 ± 0.003	[23.7 ± 0.5]	0.0174 ± 0.003	[39 ± 1]
	370	48.3 ± 0.8	[30 ± 2]	18 ± 3	[9 ± 2]	0.264 ± 0.005	[23 ±1]	0.0176 ± 0.001	[37 ± 1]
	476	49 ± 3	[45 ± 3]	10 ± 5	[7 ± 2]	0.29 ± 0.02	[19 ± 1]	0.018 ± 0.002	[28.3 ± 0.4]

[a]For the H255E and H255Q variants, the combined enzymatic and non-enzymatic rates of HPD ketonization (based on a decrease in A270 nm) were 0.004 and 0.008 s^{-1}, respectively. For H255A, the rate was not accurately determined due to the decreased timescale of the experiment.

Interestingly, despite the accumulation of ES^{red} in the H255A and H255Q variants, the rate constants associated with ketonization were reduced from ~100 to > 1000-fold for HOPDA and 9-Cl HOPDA. For H255E, in which ES^{red} formation is rate-determining, the timescale for the ketonization reaction was > 2000-fold slower than in the WT enzyme. The disparity between the ability to generate ES^{red} and the measured rate of HPD formation observed at 270 nm in the DxnB2 His255 variants has thus implicated this residue in the ketonization reaction. The specific role of His255 remains unclear since the effect of His255 substitution in DxnB2 was one to two orders of magnitude greater than the effects observed in $BphD_{LB400}$, in which acylation (HPD formation) occurred at rates that were 5 to 40-fold slower than the WT.

3.5 DxnB2-mediated cleavage of 3-Cl HOPDAs

3.5.1 DxnB2:3-Cl HOPDAs complexes do not reveal substrate destabilization

Although this work has emphasized DxnB2 as a model system for the study of substrate ketonization by the MCP hydrolases, the enzyme was initially characterized due to its remarkable ability to catalyze the hydrolysis of 3-Cl HOPDAs[39]. To better understand the manner in which DxnB2 hydrolyzes these recalcitrant PCB metabolites, the S105A variant was employed to investigate substrate destabilization of 3-Cl and 3,9,11 tri-Cl HOPDA, a model and biologically relevant PCB metabolite, respectively. The electronic absorption spectra of 3-Cl and 3,9,11 tri-Cl HOPDA were measured in the presence and absence of DxnB2 S105A (Figure 42). Binding of 3-Cl HOPDA to DxnB2 S105A resulted in a hyperchromically-shifted spectrum whereas the DxnB2 S105A:3,9,11 tri-Cl HOPDA complex revealed a 21 nm hypsochromic shift from 438 to 417 nm. Neither ES complex accumulated a detectable population of a red-shifted species, suggesting that the HOPDA

molecules are bound in a planar, non-productive conformation. Indeed, a planar binding mode was directly observed in an S105A:3-Cl HOPDA binary complex[117].

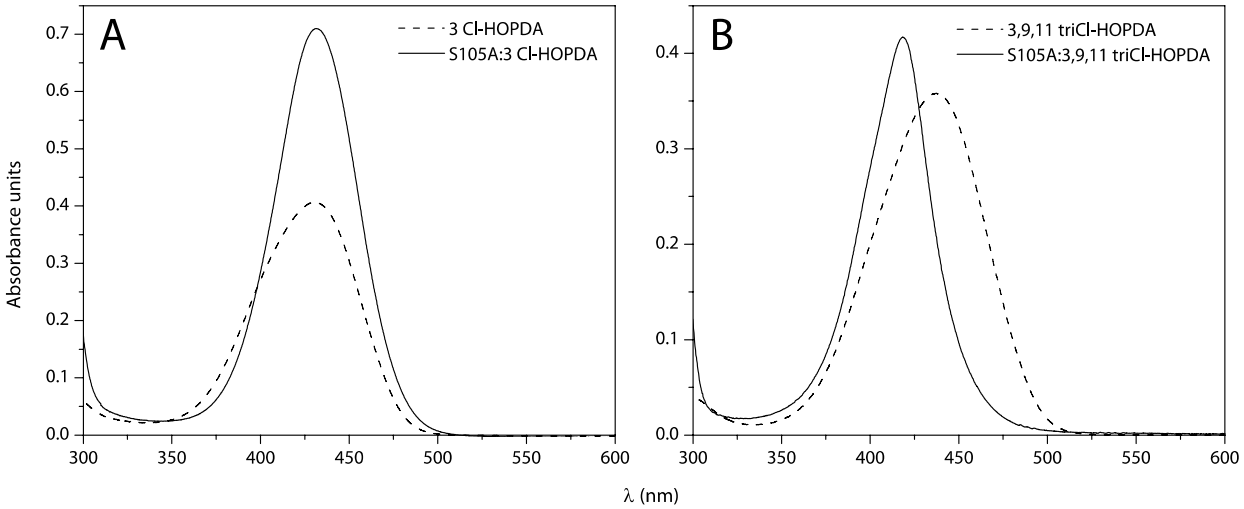

Figure 42. Electronic absorption spectra of 10 μM (A) 3-Cl HOPDA or (B) 3,9,11 tri-Cl HOPDA in solution or complexed to 40 μM DxnB2 S105A in KPi (I = 0.1 M), pH 7.5 at 25 °C.

3.5.2 DxnB2 is able to access ES^{red} faster than $BphD_{LB400}$.

In order to gain kinetic insight into the ability of DxnB2 to overcome the apparent inhibitory or stabilizing effect attributed to the 3-chloro substituent, hydrolysis of 3-Cl and 3,9,11 tri-Cl HOPDA was monitored under single turnover conditions, as described for other substrates. A PDA detector was utilized for the identification of intermediates (Figure 43, *inset*). For more accurate rate constant determination, reactions were monitored at single wavelengths. While decay of the HOPDA enolates (λ_{max} 432 or 438 nm) were readily monitored, the formation of 3-Cl HPD (λ_{max} ~244 nm) could not be distinguished from other underlying processes and the resulting multiphasic kinetic traces could not be reliably interpreted. To distinguish intra- and intermolecular events, additional reactions were performed in the presence of a viscogen, 30% sucrose (w/v).

The hydrolysis of both substrates by DxnB2 was biphasic (Figure 43 and Table 19). The first observable kinetic phase was attributed to ES complex formation, which occurred at 220 and 26 s^{-1} for the mono- and trichlorinated substrate, respectively. In both cases, the presence of sucrose slowed this bimolecular event by 1.3 to 2-fold. For 3-Cl HOPDA, ES

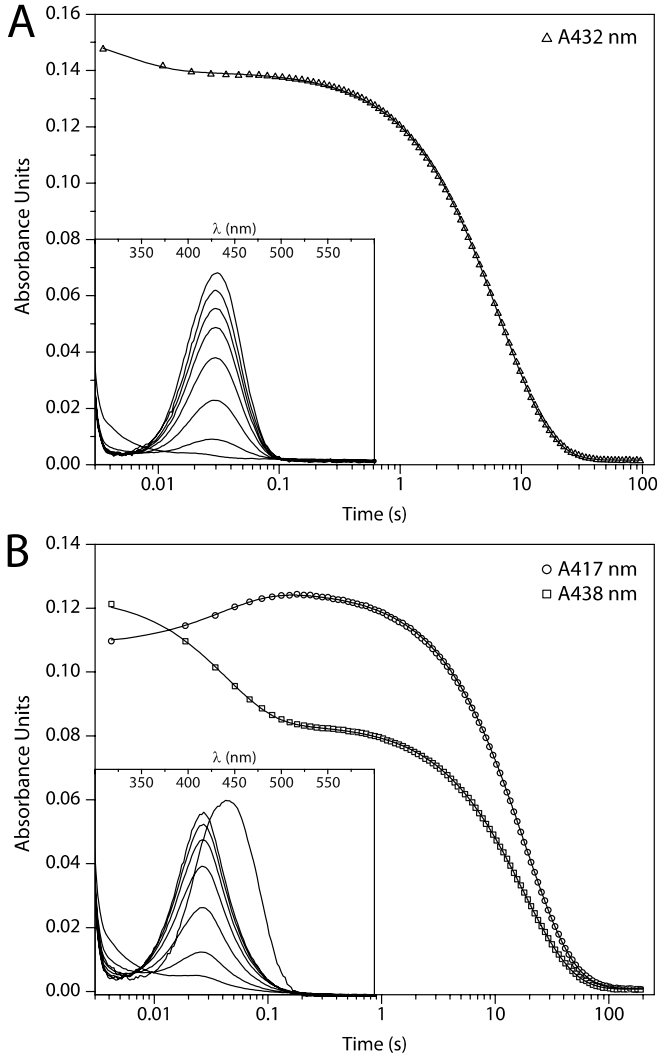

Figure 43. Results from representative stopped-flow experiments demonstrating the turnover of 4 μM 3-Cl HOPDAs by 16 μM DxnB2 (A) Hydrolysis of 3-Cl HOPDA monitored at 432 nm. (B) Hydrolysis of 3,9,11 tri-Cl HOPDA monitored at 417 and 438 nm. For each substrate, the time-dependent changes to the visible spectrum from 300 to 600 nm are inset. For clarity, 1/10 data points are shown.

Table 19. Kinetic values for the DxnB2-mediated hydrolysis of 3-Cl HOPDAs

Substrate	λ (nm)	k_1 (s^{-1}) [Amp (%)]		k_2 (s^{-1}) [Amp (%)]		k_{cat} [a]
3-Cl	432	220 ± 20	[11.5 ± 0.3]	0.152 ± 0.001	[88 ± 2]	0.25 ± 0.1
+ 30% sucrose	432	100 ± 10	[7.4 ± 0.3]	0.152 ± 0.001	[92.6 ± 0.7]	
3,9,11-triCl	417	26 ± 1	[12.2 ± 0.6]	0.056 ± 0.001	[88 ± 2]	
	438	22 ± 2	[32 ± 1]	0.056 ± 0.001	[68 ± 1]	0.13 ± 0.1
+ 30% sucrose	417	18 ± 2	[12 ± 1]	0.054 ± 0.001	[88 ± 2]	
	438	16.9 ± 0.2	[32.9 ± 0.8]	0.054 ± 0.001	[67 ± 2]	
$BphD_{LB400}$ + 3-Cl [b]	432	15	[19]	0.0077	[81]	0.0089

[a]data from [39]. [b]data from[86].

complex formation was accompanied by a small hypochromic perturbation whereas the spectrum of 3,9,11-tri-Cl HOPDA was hypsochromically-shifted by 21 nm as in the stable S105A complex. Following accumulation of the spectrophotometrically distinct ES complexes, the respective signals decayed and rate constants of 0.152 and 0.056 s^{-1} were modeled using exponential equations The observed insensitivity of $1/\tau_2$ to sucrose and the relatively large loss in amplitude (~90%), corresponding to the dissipation of the HOPDA enolate chromophore, support the assignment of this kinetic step to substrate ketonization as described for other substrates above. The absence of ES^{red} from the kinetic traces suggests that formation of this intermediate is rate-limiting to the hydrolysis of 3-Cl HOPDAs. The observed $1/\tau_2$ values differed by only 2-fold from the reported k_{cat} values[39], which may be explained by differences in the enzyme quantification methods employed. Nevertheless, substrate destabilization and ketonization still occur 20-fold faster than in $BphD_{LB400}$, accounting for the increased specificity of the DxnB2 for 3-Cl HOPDAs.

3.5.3 Comparison of the tertiary and quaternary structure of MCP hydrolases

To investigate the basis of the difference in oligomeric state and the possible link to substrate specificity, the seven structurally characterized MCP hydrolases were compared using a suite of bioinformatic tools. SEC-MALS analysis indicates DxnB2 is a dimer

whereas $BphD_{LB400}$ and HsaD are tetramers (Figure 27). CumD, CarC, and MhpC have also been described as dimers. However, the crystal structure of MhpC displays a tetrameric assembly of the same form as $BphD_{LB400}$ and HsaD. $BphD_{RHA1}$ purified as an octamer. To investigate the basis of the differences in oligomeric state, the seven structurally characterized MCP hydrolases were superposed and a structure-based sequence alignment was established (Figure 44). As noted previously for $BphD_{LB400}$[81], all of the crystal structures present a two-fold symmetric dimer mediated in part by anti-parallel β-interactions between edge strands (β8) of the monomer's core domains; the associated protein surfaces are defined as elements as the dimeric interface, the A-B interface identified for $BphD_{LB400}$. Of interest here are the distinctions in sequence and structure that mediate assembly of the $BphD_{LB400}$, HsaD, and MphC tetramers through additional interfaces that have been labeled as such: the tetrameric A-B' and A-A' interfaces.

The protein segment that connects the α/β-hydrolase core and the N-terminus of the lid domain is referred to as the NC-loop in other enzyme families[46,118]. Prior to the NC-loop, a conserved LMG sequence (DxnB2 127-9) completes the β6 strand in all known structures. The glycine residue, at position *i*, has a left-handed α conformation, which creates a sharp turn as the backbone departs from the core. The next highly conserved sequence positions are a pair of branched non-polar residues at positions *j* and *j*+3 (DxnB2 residues 146 and 149); the length of the protein segment between *i* and *j* varies between 12 and 17 residues in the known structures. In all structures except that of CarC (wherein these residues are disordered and not defined by the electron density maps), the side chains of residues *j* and *j*+3 project from a helical segment of the lid domain into the NP-substrate binding subsite. Importantly, the residues between positions *i* and *j* are prominent at the tetrameric interfaces,

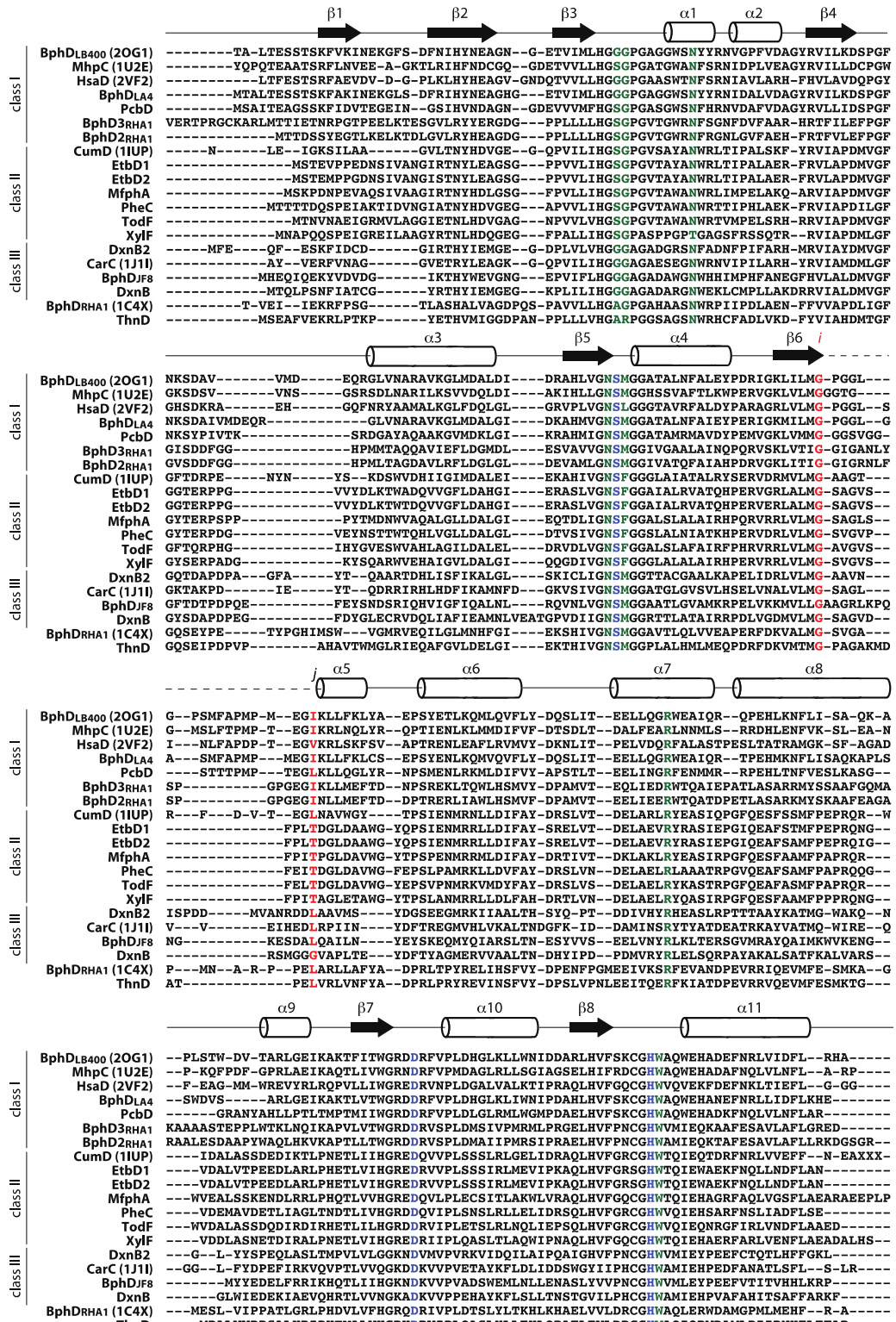

Figure 44. Sequence alignment resulting from the structural superposition of seven MCP hydrolases. The NC-loop is indicated by a dashed line. Secondary structural elements are numbered. The catalytic triad is coloured blue whereas the P-subsite and 'oxyanion hole' residues appear in green. The residues defined as i and j are coloured red. The helix labeled 11 might also be considered a pair of shorter helices joined by a turn.

and the sequences and structures of BphD$_{LB400}$, HsaD, and MhpC present features distinguishing them from the dimeric MCP hydrolases (Figure 45).

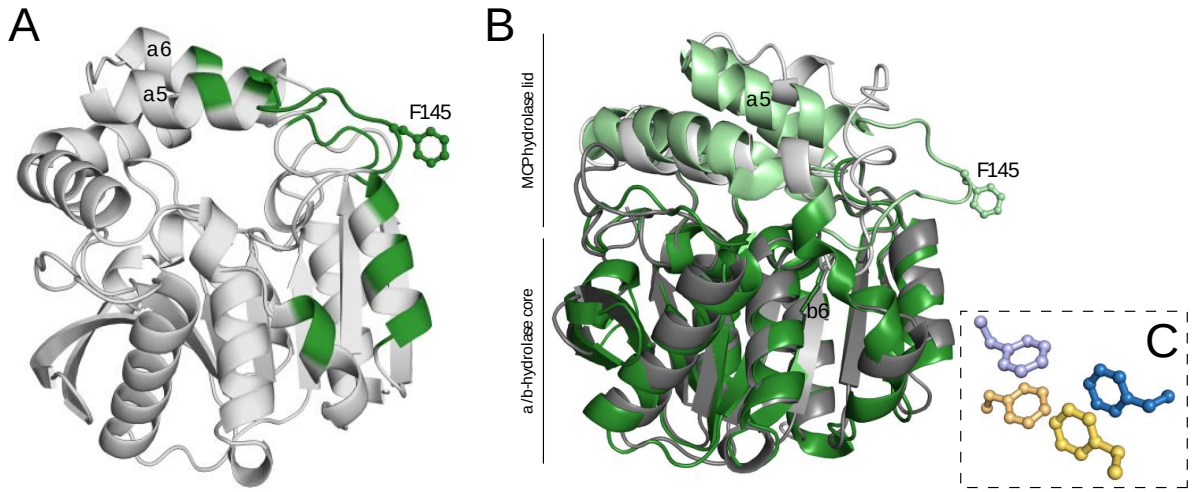

Figure 45. (A) Ribbon drawings of the BphDLB400 protomer (PDB ID: 2OG1, chain A). The regions that are involved either the A-B' and/or A-A' tetrameric interfaces, which include the NC-loop and lid domain helices, are colored green. (B) Superposition of the DxnB2 S105A:3-Cl HOPDA binary complex and BphDLB400 demonstrating differences in the NC-loop. (C) The apolar phenylalanine cluster conserved among MCP hydrolase tetramers. The dimer pairs (A-B pairs) are color coded blue and yellow.

In particular, the tetrameric MCP hydrolases of known crystal structure all share an F-X-P-X-P motif that begins at position *i*+9 and contributes to the tetrameric interface that associates a pair of lid domains, the A-B′ interface. In fact, F$_{i+9}$ makes a visually striking contribution to both tetrameric interfaces as illustrated in Figure 45. Thus F$_{i+9}$ lies at the apex of a loop that protrudes away from the hydrolase and lid domains, and F$_{i+9}$ residues from all four monomers cluster to form a buried apolar core at the junction of the A-B' and A-A' interfaces. Residues immediately preceding F$_{i+9}$ as well as residues in the linker and the helix (α9) that follows the triad Asp also contribute to tetramer formation, but they do not belong to sequence motifs that distinguish dimers and tetramers. BphD$_{LB400}$, HsaD, and MhpC belong to the same class, class I, on the basis of amino acid sequences**(10)**. The sequences of other homologs in this class such as PcbD from *Pseudomonas strain* sp. DJ12 and Ro09014

from *R. jostii* RHA1 show variations at the first position of the F-X-P-X-P motif. However, the oligomeric states are not known.

In contrast to the protruding structure observed for the tetramers, the first few residues of the NC-loop in DxnB2 associate with helix α10 of the hydrolase core domain as well as residues just prior to helix α9 via several hydrogen bonds. The NC-loop of CumD is five residues shorter than that of DxnB2 and, while it follows a similar path, is not involved in the same suite of H-bonding interactions. However, CumD and several other class II enzymes share an F-P-XP-Q-X$_4$-D motif that disrupts helix α8 in CumD and places the Gln side chain from this motif in position to hydrogen bond with the backbone carbonyl and amide of NC-loop *i*+6 and *i*+8 residues, respectively. Indeed, class-specific lid domain architecture was apparent upon superposition (Figure 46).

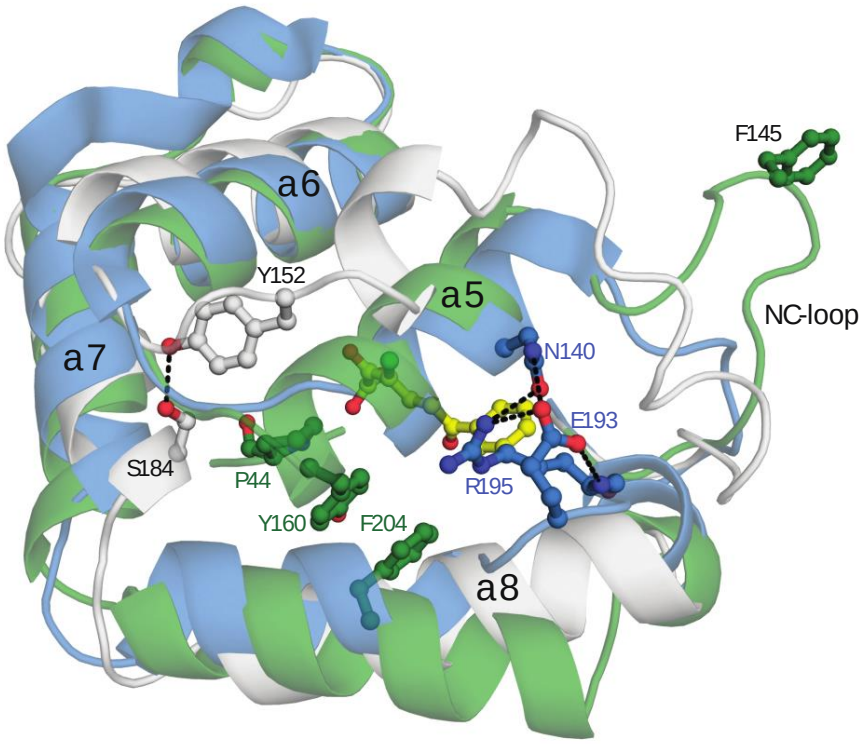

Figure 46. Superposition of MCP hydrolase lid domains from BphD$_{LB400}$ (class I; green), CumD (class II; blue) and DxnB2 (class III; white). Some of the relevant helix-helix interactions are shown.

In general, the beginning and end of the lid show greatest variability among the known MCP hydrolase crystal structures (Figure 44). Thus in many pair-wise or multi-protein comparisons it can be difficult to structurally align residues from the NC-loop and α5 and/or residues within α8 and the segment that links α9 to α10. In addition, the NC-loop and α5 are prone to disorder and are sensitive to the occupancy of ligands in the active site. These uncertainties should be considered in evaluating sequence alignments, including those based on structures. By contrast, the segment of the lid spanning helices α6 and α7, residues 155-186 of DxnB2 and residues 164-196 of $BphD_{LB400}$, is more readily superposed and aligned.

The position of the helix α5 is particular interesting when considering the observed differences in the rates of 3-Cl HOPDA hydrolysis by DxnB2 and $BphD_{LB400}$. Accordingly, the lid domain architecture of all available DxnB2 S105A:MCP binary complexes was also compared by structural superposition. Despite the conserved interaction between helix α5 and helix α6 in all DxnB2 structures, mediated in part by the H-bonding interaction between Tyr152 and Ser184, the orientation of the N-terminus of the former helix is variable (Figure 47). More specifically, the lid domain in the S105A:3-Cl HOPDA binary complex appeared to adopt a more "open" conformation than those observed in the S105A:HOPDA or S105A:5,8-diF HOPDA complexes[117,119]. Indeed, the different lid conformations were also reflected by two distinct substrate binding modes: a planar, and apparently non-productive binding mode was observed for 3-Cl HOPDA, whereas non-planar dienoate binding modes, which could be correlated to ES^{red} by single crystal spectroscopy, were observed for HOPDA and 5,8-diF HOPDA[112,117]. Together, the analysis suggests that lid dynamics help to mitigate the hydrolysis of recalcitrant PCB metabolites.

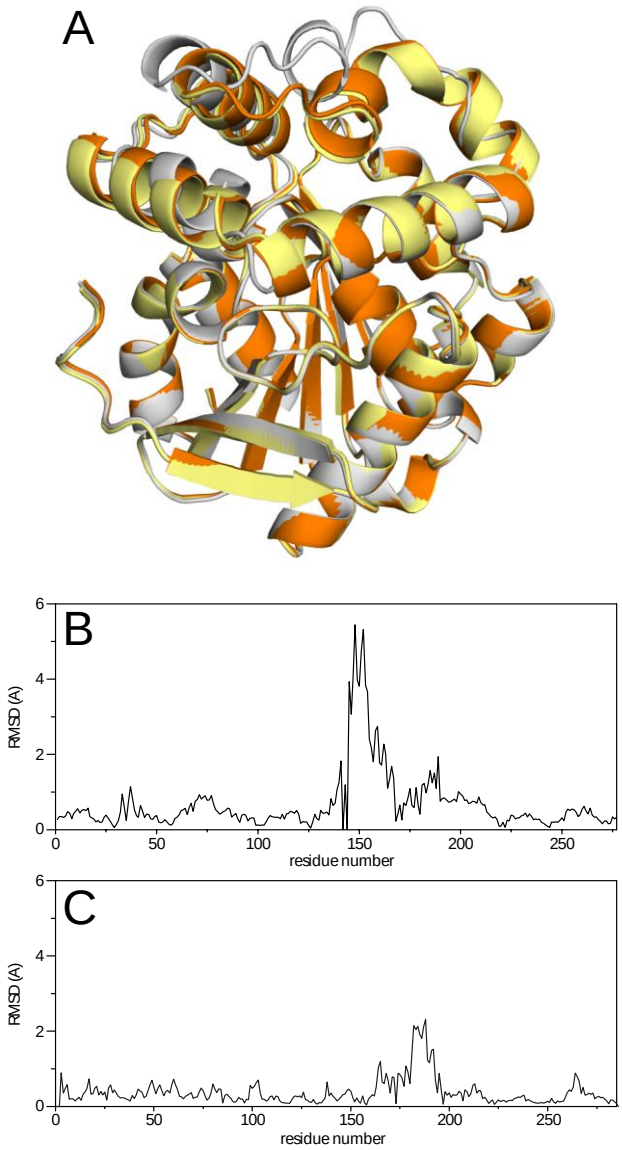

Figure 47. Differences in the position of DxnB2 helix α5. (A) Structural superposition of DxnB2 S105A in complex with 3-Cl HOPDA (white), HOPDA (yellow) and 5,8-diF HOPDA (orange). The difference in the positioning of helix α5 is highlighted at the top. (B) Root mean square distance (RMSD) in Å between the Cα atoms of DxnB2 S105A:3-Cl HOPDA and S105A:HOPDA binary complexes. The 5,8-diF HOPDA complex is nearly isomorphous with the latter. (C) RMSD in Å between chain A and B of a crystalline dimeric assembly of $BphD_{LB400}$ (PDB ID: 2OG1). The largest observed differences are in helix α9, which can be partially explained by uncertainties in Cα position.

Chapter 4: DISCUSSION

4.1 The chemical mechanism of the MCP hydrolases

This thesis describes the chemical mechanism of the MCP hydrolases using two phylogenetically distinct homologues that share less than 30% identity and have distinct oligomeric states. First, stopped-flow analysis and chemical quench experiments on $BphD_{LB400}$ provide evidence for an acyl-enzyme rather than a *gem*-diolate intermediate. Acylation was reproduced in DxnB2 using both HOPDA and 9-Cl HOPDA as substrates. These findings were complemented with a crystallographic study of $BphD_{LB400}$ in which electron density extending from the catalytic serine in the H265Q variant could be unambiguously modeled with a benzoyl moiety[119]. Stoichiometric incorporation of ^{18}O into benzoate from the $BphD_{LB400}$-mediated turnover of HOPDA also provided indirect support for a covalent mechanism of catalysis. Finally, comparison of the hydro- and methanolysis of HOPDA and pNPB by $BphD_{LB400}$ suggests that both C-C and C-O bond cleavage occurs via a covalent mechanism. Nevertheless, acylation during the former is histidine-independent, and a substrate-assisted mechanism of nucleophilic catalysis has been forwarded. Overall, the body of work overturned the paradigm for these enzymes in the literature.

The study of DxnB2 was particularly informative with respect to the mechanism of substrate ketonization by the MCP hydrolases. Solvent viscosity and isotope effects allowed for the identification of substrate ketonization as the rate-limiting step in the acylation reaction. Furthermore, the influence of the P-subsite on catalysis, specifically ES^{red} formation and substrate ketonization, was clarified using stopped-flow and other spectrophotometric assays of systems at equilibrium.

4.1.1 An updated substrate-assisted nucleophilic mechanism of catalysis

On the basis of the evidence presented herein, emphasizing the histidine-independent acylation, an updated mechanism of catalysis using $BphD_{LB400}$ as the prototypical MCP hydrolase is proposed (Figure 48). To begin, the active site architecture, observed binding phenomena and changes in the visible spectra suggest preferential binding of a dianionic HOPDA isomer. The pK_a of the catalytic histidine is unknown, although a possible interaction with Asn111 suggests that it may be protonated in the resting state. In this case, His265 may serve as a general acid to protonate the oxido group of a dianionic HPD produced during bond cleavage. Alternatively, a lone pair of electrons on the His265 $N^{\varepsilon 2}$ may help to favor localization of negative charge in the bound dianion near the 'oxyanion hole'. Importantly, a *gauche*+ conformation around the C4-C5 bond is required to maintain all interactions between the substrate and the NP- and P-subsites. Ultimately, the substrate destabilization, empirically observed as ES^{red}, is thought to be manifested as the increased reactivity at C5. Thus, the reactivity of ES^{red} towards protonation at C5 replaces the His-Asp dyad in the activation of Ser112, thereby completing ketonization via a proton transfer. After ketonization, which generates a requisite electron sink, the resulting serinate can attack the C6-carbonyl, forming the first tetrahedral oxyanion intermediate that collapses to a Ser112 benzoyl-ester and HPD. If His265 $N^{\varepsilon 2}$ were uncharged the lone pair may act to destabilize product binding, accelerating its release. Alternatively, it may act as general acid as described above. Nevertheless, upon binding of H_2O to the acyl-enzyme, the His-Asp dyad acts as a general base to activate it. Nucleophilic attack on the acyl-enzyme generates the second tetrahedral oxyanion intermediate, which ultimately leads to benzoate production. At the end of the catalytic cycle, protonation of Ser112 regenerates the resting state enzyme.

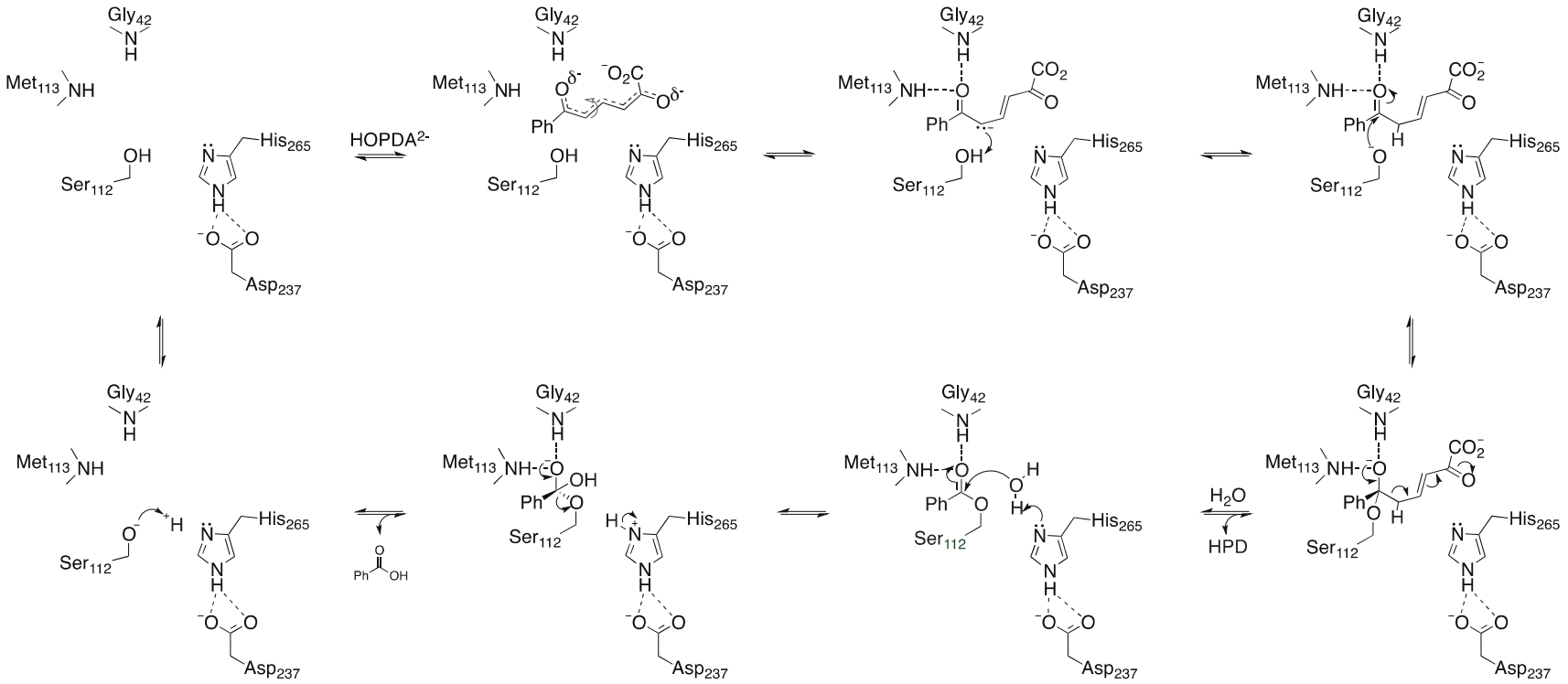

Figure 48. The proposed MCP hydrolase mechanism. Although the pK_a of His265 is unknown, it is drawn as neutral. P-subsite residues (not shown) play a critical role in the ketonization reaction. The top line of the mechanism can be considered as MCP hydrolase-specific chemistry whereas the bottom line represents chemistry shared by other α/β-hydrolases. The second equilibrium arrow bridging the second and third panels on the top line represents an enzyme-substrate complex equilibrium (the two HOPDA dianions drawn are resonance forms). This equilibrium (for example, a subtle change in the active site microenvironment to induce substrate destabilization or conformational dynamic of the MCP hydrolase lid domain, *vide infra*) is thought to result in the formation of ES^{red} and modulate it's reactivity. A grey arrow is drawn in the second panel to indicate rotation about the C4-C5 bond resulting in a *gauche*+ conformation at the active site.

For the MCP hydrolases studied herein, the turnover of HOPDA is typically limited by the deacylation reaction. Alcoholysis experiments suggest that this step is limited by the rate at which the His-Asp dyad activates water. Interestingly, the mechanistic investigations of DxnB2 and $BphD_{LB400}$ have also revealed that substrate destabilization and ketonization may be rate-limiting for the hydrolysis of environmentally relevant PCBs.

More specific to $BphD_{LB400}$ and other tetrameric homologues, which appear to be half-site reactive, a two-conformation model of catalysis can be inferred. The possibility that product release may limit acylation at the second set of active sites in these half-site reactive homologues remains unknown. Interestingly, two (F_o-F_c) difference electron density features approximately the size and shape of a phenylalanine side chain were observed in a nonpolar surface pocket bounded largely by the side chains of Ile153, Phe157, Phe204, and Leu205 near the periphery of the NP subsite in $BphD_{LB400}$[119]. These features approach within 5 and 7 Å of the active site HOPDA's phenyl group and may represent the phenyl groups of additional HOPDA molecules with disordered dienoate groups. Furthermore, an additional HOPDA density was observed at the opposite side of the active site in the $BphD_{LB400}$ H265Q:HOPDA structure. Thus, it appears that $BphD_{LB400}$ may have two routes for substrate/product entry/egress, which may also influence reactivity.

4.1.2 Evidence for a nucleophilic mechanism

This thesis presents three independent lines of evidence that support a nucleophilic mechanism of catalysis. First, an acyl-enzyme was observed by mass spectrometry in DxnB2, $BphD_{LB400}$ WT and H265Q. Complementary X-ray crystallography experiments also revealed the nature of the reported Ser112-benzoyl intermediate[119]. Second, a single equivalent of ^{18}O was incorporated into the benzoic acid product of HOPDA when

hydrolyzed by $BphD_{LB400}$ in $H_2{}^{18}O$. Finally, common k_{cat} values and equal nucleophilic partitioning ratios were observed for the methanol-dependent C-C and C-O bond cleavage of HOPDA and pNPB by $BphD_{LB400}$.

4.1.2.1 Direct evidence for an acyl-enzyme intermediate

The chemical quench data provide evidence for the occurrence of a covalent catalytic intermediate in a wild type MCP hydrolase. LC ESI/MS on intact protein samples of DxnB2 and $BphD_{LB400}$ revealed modifications that were consistent with acylation. Furthermore, peptide matching from LC ESI/MS/MS of pepsin-digested reaction mixtures of $BphD_{LB400}$ WT or H265Q and HOPDA substantiated the observations that were made on the intact protein samples. In both cases, benzoylation was uniquely identified as a modification to Ser112. LC ESI/MS on intact $BphD_{LB400}$ reactions mixtures of varied age indicated that the modification occurs on a timescale commensurate with turnover. These data represent the first unambiguous identification of a catalytic intermediate on the MCP hydrolase pathway. All other reports on possible reaction intermediates have relied on indirect methods and variant enzymes[64,89].

In line with the rapid acylation of $BphD_{LB400}$ H265Q, observed by MS, a Ser112-benzoyl species was trapped in a crystals of this variant upon exposure to HOPDA[119]. A 1.6 Å resolution crystal structure of H265Q incubated with HOPDA revealed clear electron density extending from the catalytic serine, which was unambiguously fit with a benzoyl moiety at full occupancy (Figure 48). The benzoyl-oxo formed H-bonds with the amides of each of the 'oxyanion hole' residues, Met113 and Gly42, highlighting a capacity to stabilize the formation of tetrahedral oxyanion intermediates during catalysis. The side chain of Gln265 was also oriented by polar contacts, including an H-bond between the Gln265 $N^{\varepsilon 2}$

and $O^{\delta 2}$ of Asp237 of the catalytic triad. The Gln-Asp effectively constitute a dyad, with no apparent interactions with the Ser-benzoyl moiety, which is located more than 4.5 Å from the $N^{\varepsilon 2}$ of Gln265. Additional H-bonding linking Gln265 $O^{\varepsilon 1}$ and Asn111 $N^{\delta 2}$ was also observed. The stability of the crystalline acyl-enzyme can be attributed to the inability of the H265Q variant to activate water for deacylation. This was observed in solution as the rate constant for acylation of the $BphD_{LB400}$ H265Q was ~10 s^{-1} although steady-state turnover or deacylation proceeded at only ~10^{-5} s^{-1}.

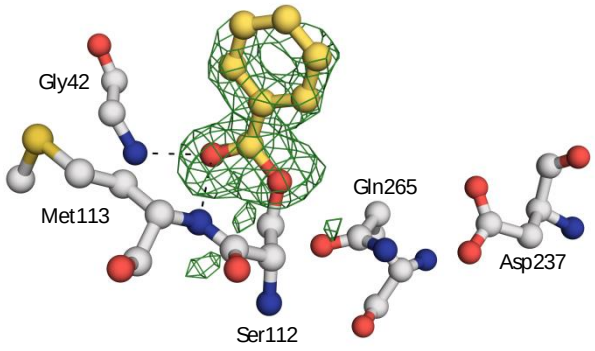

Figure 49. Ball-and-stick representation of the $BphD_{LB400}$ H265Q:HOPDA complex active site, including the unbiased $F_o - F_c$ density (green) for the benzoyl adduct, contoured at 3 σ. H-bonding is indicated between the 'oxyanion hole' residues and the benzoyl moiety.

The identification of an acyl-enzyme in $BphD_{LB400}$ and DxnB2 conflicts with previous reports on the mechanism of MhpC and $BphD_{LB400}$. Two major arguments against covalent catalysis were based on the inability to observe an acyl-enzyme in MhpC[64] and the assignment of a ^{13}C NMR signal to a *gem*-diolate species in both MhpC and $BphD_{LB400}$ variants[89]. First, the failure to trap an acyl-enzyme intermediate in MhpC may be explained by the reaction and quenching conditions that were used. In some cases, the quenching reagents appear to be insufficient to halt turnover. In other cases, the reaction time appears to be too long, leading to complete turnover prior to the addition of a proper quenching reagent.

The assignment of the ^{13}C NMR signal to a *gem*-diolate in samples of catalytically impaired hydrolase variants turning over HOPDA is weak for at least three reasons. In these studies, performed using [$^{13}C6$]-HOPDA and each of $BphD_{LB400}$ S112A, H265A or MhpC H114A[89], assignment of the signal at 128 ppm was based primarily on a predicted chemical shift value for a *gem*-diolate H-bonding to serine hydroxyl. However, the quality of the signal is compromised by the poor signal-to-noise ratio in the spectra. Moreover, a signal with the same chemical shift but having a sharper linewidth was present in the enzyme-free substrate sample (Figure 17) and was attributed to a hydrated γ-lactone, a HOPDA decay product. The authors did not rule out the presence of this decay product in the enzyme samples. Indeed, an enzyme:lactone complex would account for the observed increase in linewidths. Finally, the observation of a shared ^{13}C NMR signal in samples of $BphD_{LB400}$ S112A and H265A variants is inconsistent with the spectrophotometric evidence that each accumulates a distinct intermediate[66].

4.1.2.2 Evidence for an acyl-enzyme intermediate from isotope studies

The stoichiometric incorporation of ^{18}O from solvent into benzoate by $BphD_{LB400}$ contrasts to a study of MhpC, in which 3 to 6% of its succinic acid product contained two ^{18}O equivalents[64]. Unfortunately, the MhpC study did not report on the possibility of an enzyme-catalyzed ^{18}O incorporation into succinate. Significantly, both aspartic and serine proteases have been reported to exchange ^{18}O into their acid products despite using different catalytic mechanisms for hydrolysis have been reported[88,120,121]. While $BphD_{LB400}$ did not catalyze solvent exchange into benzoate, differences between the systems may account for the differential incorporation of ^{18}O into the respective reaction products. First, several distinct binding modes have been observed for succinate and malonate in complex with

MhpC H263A[65] and $BphD_{LB400}$[86], respectively. Along these lines, small diacids interact with the hydrolase active site differently than monoacids such as benzoate. Furthermore, MhpC contains an additional active site histidine, His114, which contributes to catalysis and coordinates succinate *in crystallo*[65,113]. This residue, which corresponds to Ala116 in $BphD_{LB400}$, may influence the reactivity of small diacids with MhpC. Interestingly, MhpC can activate hydroxylamine[114], and the rate of 5-carboxyvalero-hydroamic acid and ethanol formation from the reaction of ethanolamine and monoethyl adipate was ~50% slower in the H114A variant than in the WT. Finally, the resolution of the product detection method (GC/MS) cannot be used to define the position of the second ^{18}O-incorporation event. In particular, either carboxylate group of the succinic acid product may be susceptible to exchange. However, the proposal that an ^{18}O-incorporated *gem*-diolate could be misprocessed, released to the bulk solvent and dehydrated to form an ^{18}O-substrate implies that a single carboxylate is doubly incorporated[64].

4.1.2.3 Evidence for an acyl-enzyme from steady-state kinetic approaches

The detection of reaction intermediates by steady-state kinetics is indirect and relies on inference: relating results to direct observations and kinetic models of catalysis[95]. At a minimum, the detection of an intermediate from steady-state methods depends on: (i) the ability of an accumulated species to react with an acceptor whose concentration may be varied, and (ii) the generation of a common intermediate from substrates that share chemical substructure. Herein, water and methanol represent acceptors for a common Ser112-benzoyl intermediate produced during the turnover of HOPDA and pNPB. The similar methanol-dependent k_{cat} or k_{obs} values for HOPDA and pNPB hydrolysis, respectively, together with the common partitioning of these reactions between the hydro- and alcoholytic pathways

mirror what has been reported for other hydrolases that utilize a covalent mechanism of catalysis. Thus, constant partition ratios have been reported in serine proteases, such as chymotrypsin[122], and non-serine hydrolases, such as prostatic acid phosphatase[123], which are proposed to proceed via acyl-enzyme intermediates. For the $BphD_{LB400}$-mediated methanol-dependent turnover of HOPDA, a simple kinetic model for a nucleophilic mechanism correctly predicted the observed increase in k_{cat} and K_m as well as the independence of k_{cat}/K_m[101]. Furthermore, the experimentally determined product ratios from the turnover of both HOPDA and pNPB, respectively, also matched the values predicted by the nucleophilic model of catalysis. Collectively, the data suggest that C-C and C-O bond hydrolysis proceed through a shared Ser112-benzoyl intermediate.

This conclusion contradicts an earlier proposal that Ser112 acts as a hydrogen bond donor during C-O bond hydrolysis. This previously assigned role for Ser112 was deduced from a Hammet analysis using *para*-substituted pNPBs[93] and further supported using substrate docking experiments[115]. In particular, the Hammet plot was nonlinear, a feature that was attributed to a change in the rate-limiting step from ester bond cleavage to product release for substrates for which $\sigma \geq 0$. An alternative explanation for the nonlinearity is that the activation of water for nucleophilic attack on the Ser112-benzoyl ester may become rate-limiting for substrates for which $\sigma \geq 0$. This alternate explanation is consistent not only with the dependence of k_{cat} on alcohol but also with the presence of a SKIE during turnover of esters[93]. Moreover, the strikingly similar k_{cat} values observed for the DxnB2-mediated hydrolysis of several HOPDAs[39], supports a rate-limiting step that is independent of or shows little dependence on the MCP's identity.

4.1.3 Evidence for rate-limiting hydrolysis

The observed accelerations in the initial reaction velocities and the ability of $BphD_{LB400}$ to utilize longer alcohols, such as 2-propanol, is consistent with a covalent mechanism of catalysis. The crystal structure of $BphD_{LB400}$ S112A in complex with HOPDA reveals a complex suite of interactions[66,86], which is thought to reflect the high degree of active site residue conservation. Little residual volume is present within the substrate-occupied active site, suggesting that acylation and release of HPD precede the binding of additional nucleophiles such as water or alcohols. Indeed, product inhibition studies support a mechanism in which HPD is released before benzoate during turnover of HOPDA[81]. In contrast, significant movement of the MCP hydrolase lid domain would be required to bind additional molecules to a HOPDA-occupied active site. Considering the full suite of interactions within the enzyme-substrate complex, it is difficult to conceive how such lid movement would not disrupt productive substrate binding.

The alcohol-dependent acceleration of v_0 provides novel insight into the MCP hydrolase catalytic cycle by implicating deacylation as the rate-limiting catalytic step. To date, experiments in MhpC and $BphD_{LB400}$ have assigned k_{cat} to either release of the non-covalently bound product[83,93] or a conformational change associated with chemistry[81]. The observed increase in the rate of turnover in the presence of alternate acceptors suggests breakdown of the acyl-enzyme intermediate rather than product release limits catalysis. Indeed, the methanol-induced acceleration to k_{cat}, 28 s^{-1} versus 6.5 s^{-1}, is similar in magnitude to that reported for the turnover of an ester substrate by α-chymotrypsin, 482 s^{-1} versus 144 s^{-1}[122]. While the data do not unambiguously refute the possibility that product release is rate-determining, the observation of similar accelerations to v_0 by different alcohols suggests

that this scenario is unlikely. Specifically, the limiting of turnover by product release would imply that methyl, ethyl, and propyl benzoates are released from the active site at an equal rate that is faster than that of benzoic acid. By contrast, assigning a chemical dependence to k_{cat} is consistent with the presence of an SKIE during $BphD_{LB400}$-mediated ester bond hydrolysis[93]. Interestingly, the lack of a viscosity effect reported for the single turnover of HOPDA by $BphD_{LB400}$[81] implies that this rate-limiting deacylation at one set of active sites must precede acylation at the second set of active sites in the two-conformation model of catalysis.

4.1.4 The role of the catalytic histidine

The catalytic histidine is the only universally conserved catalytic residue in the α/β-hydrolase superfamily. As such, it has been implicated in both general base and nucleophilic mechanisms of catalysis. In the general base mechanisms proposed for the cofactor-less dioxygenases, the His-Asp dyad mediates a proton abstraction from a hydroxyl group on the substrate[63]. Cyanohydrin cleavage by the hydroxynitrile lyases is also initiated by a substrate deprotonation catalyzed by the triad residues[62]. In contrast, the generally accepted nucleophilic mechanism of catalysis posits a multifunctional role for the catalytic histidine, acting as (i) a general base for the activation of the serine nucleophile, (ii) a general acid for the protonation of the leaving heteroatom and (iii) a general base for the activation of water during the deacylation reaction.

The role of the catalytic histidine in the MCP hydrolases is more obscure. Histidine-independent acylation was directly observed in $BphD_{LB400}$. However, this histidine was required for acylation during pNPB turnover. Thus, while the catalytic triad of the MCP hydrolases behaves in a “textbook” fashion for C-O bond cleavage, C-C bond cleavage

appears to proceed through a substrate-assisted mechanism of nucleophile activation. During this reaction, the catalytic histidine can be considered as a contributor to the P-subsite, which influences substrate binding, destabilization and ketonization.

4.1.4.1 The role of the catalytic histidine in the acylation reaction

Kinetic characterization of histidine variants of $BphD_{LB400}$ suggested that acylation was histidine-independent, reduced by only 5- to 40-fold compared to the WT. In the case of $BphD_{LB400}$ H265Q, this was confirmed by mass spectrometry of a chemically quenched reaction mixture. Moreover, a $BphD_{LB400}$ D237N variant behaved similarly to His265 variants during single turnover experiments[89], exhibiting a hyperchromic-shift at 434 nm and a slower rate constant for acylation. These initial studies were the impetus for the hypothesis of a substrate-assisted mechanism of nucleophile activation in the MCP hydrolases. Further inspection of the rates provisionally associated with acylation/HPD formation (limited by ketonization) in DxnB2 His255 variants revealed a more complex role for this catalytic residue. Specifically, acylation of the DxnB2 variants was more drastically perturbed, and the measured rates of HPD formation were reduced by up to 6000-fold. The moderate decrease in the rate of acylation observed in $BphD_{LB400}$ His265 variants likely reflects cognate enzyme-substrate interactions. Thus, the catalytic histidine is integral to a properly organized P-subsite, which is required for efficient ketonization (see section 4.4). Differences in enzyme-substrate interactions, originating from both enzyme dynamics and active site microenvironment may also contribute to the large differences in the effect of histidine substitution in DxnB2 compared to $BphD_{LB400}$. Along these lines, $BphD_{LB400}$ is a tetramer whereas DxnB2 is a dimer, and the active site of $BphD_{LB400}$ contains an additional polar interaction between its Tyr52 hydroxyl and the backbone carbonyl of Asn111 in the P-

subsite (Figure 50A). This additional interaction may account for stabilization of the P-subsite in $BphD_{LB400}$ compared to DxnB2, in which a phenylalanine is present in the same position (Figure 50B). In the observed DxnB2 S105A:MCP binary complexes but not the ligand-free structures, the position of Asn104 (Asn111 in $BphD_{LB400}$) and the organization of the P-subsite is the same as that observed in the $BphD_{LB400}$ WT active site. Overall, the results indicate that the catalytic histidine contributes to but is not required for serine activation and acylation in MCP hydrolases, showing a remarkable divergence from the canonical mechanism typified by the serine proteases[73,121].

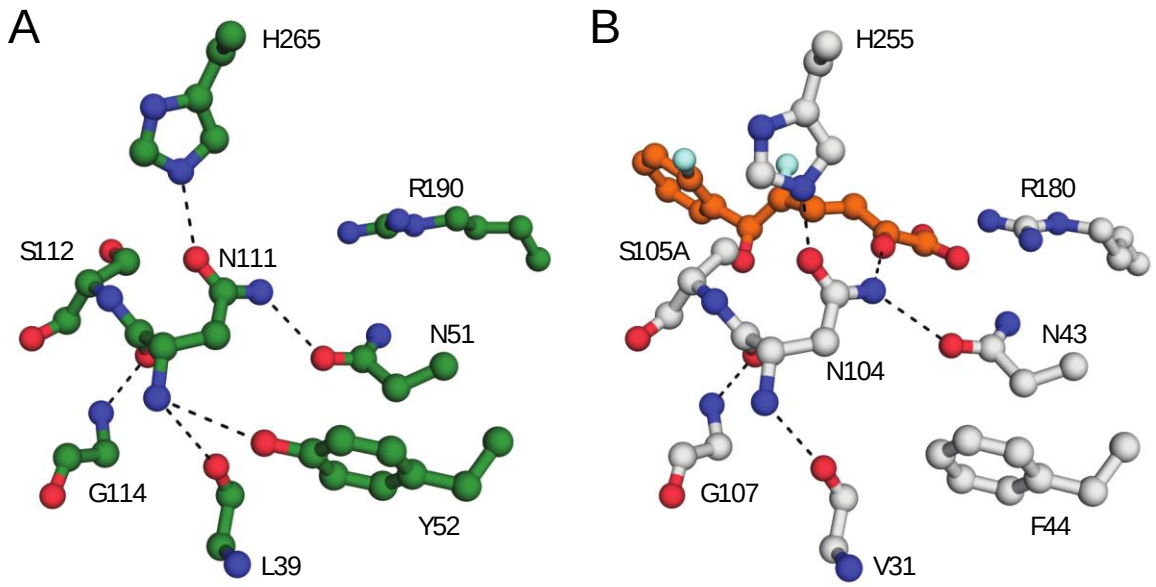

Figure 50. Ball-and-stick representations of $BphD_{LB400}$ and DxnB2 active sites. (A) The $BphD_{LB400}$ WT active site (PDB ID: 2OG1, chain A) in the absence of an MCP. (B) The DxnB2 S105A:5,8-diF HOPDA binary complex (coordinates provided by Bhowmik & Bolin, [117]). Possible polar interactions are indicated by dashed lines and the potential role of Tyr52 in the pre-organization of the P-subsite is highlighted by the comparison.

In the histidine-independent mechanism of nucleophile activation proposed for the MCP hydrolases, the substrate rather than the His-Asp pair acts as a general base to deprotonate Ser112, which also completes substrate ketonization. Interestingly, concerted movement of the catalytic His and the adjacent, conserved Trp residue away from the

nucleophile has also been observed in unpublished structures of DxnB2 upon substrate binding[117,119]. Thus, the kinetic and crystallographic data highlight the divergent catalytic mechanism of the Ser-His-Asp containing MCP hydrolases, which have evolved to utilize the chemical potential of the MCP substrates.

4.1.4.2 The role of the catalytic histidine in ES^{red} formation

The catalytic histidine is not absolutely required for the formation of ES^{red} in the MCP hydrolases. Contrary to the rate constants reported for ketonization, which were greater for $BphD_{LB400}$ than for DxnB2 catalytic histidine variants, the DxnB2 His255 variants accumulated ES^{red} while the $BphD_{LB400}$ His265 variants did not. Interestingly, the fact that a red-shifted species is observed in DxnB2 but is less reactive indicates that the catalytic His also has a role in the ketonization reaction. As discussed above, the histidine is fundamental for the maintenance of the P-subsite.

The crystal structure of the $BphD_{LB400}$ S112A/H265Q variant reinforces the importance of the catalytic histidine in forming ES^{red} and maintaining the P-subsite. The comparison of the $BphD_{LB400}$ S112A and S112A/H265Q variants provides unique insight into the nature of cognate enzyme-substrate interactions and disruption thereof. Thus, geometrically distinct HOPDA conformations are correlated to ES^{red} or a species that possesses a hyperchromically-shifted absorption spectrum. As previously outlined, the conformation of ES^{red} is non-planar and includes a *gauche+* conformation about the C4-C5 bond. Ultimately, the observed conformation is thought to be poised for ketonization but is trapped in these structures due to the lack of the serine hydroxyl. In contrast, the X-ray structure of a $BphD_{LB400}$ S112A/H265Q:HOPDA complex revealed a presumably non-productive binding mode[119]. Restrained refinements of HOPDA at the active site

suggested that a (3*E*,5*Z*)-2-oxo-6-oxido-dienoate was compatible with the X-ray data although the binding of a (2*E*,4*E*)-2-hydroxy-6-oxo- or a (3*E*)-2,6-dioxo isomer could not be eliminated based on the electron density observed for the substrate. The latter isomer is disfavored in light of the visible absorption spectra observed in solution: the enol has an expected λ_{max} at 340 nm whereas an enolate spiecies, λ_{max} 434 nm, is observed in BphD S112A/H265Q. In the absence of enzyme, the existence of a (3*E*,5*Z*)-2-oxo-6-oxido-dienoate was validated by observations of solvent ^{18}O exchange into the substrate. The observed binding mode, in which the dienoate carbons, C1 to C6, are coplanar, is stabilized in part by a number of polar contacts (Figure 51A). In particular, the 6-oxido group is H-bonded to both the 'oxyanion hole' amides. At the P-subsite, the HOPDA carboxylate hydrogen bonds with Gly43, Arg190, Trp266 and a water molecule that also forms H-bond with Gly41, Asn51, and Asn111. In the absence of HOPDA, a second water molecule (not shown) replaces the interactions of a carboxylate oxo-group in the P-subsite. The orientation of the planar (3*E*,5*Z*)-2-oxo-6-oxido- isomer and its interaction with the active site differ significantly from the observed binding mode in the S112A:HOPDA complex, which has been fit to a non-planar (3*E*)-2,6-dioxo isomer (Figure 51B).

The contribution of the catalytic His to the maintenance of the P-subsite is highlighted in structures of the $BphD_{LB400}$ S112A/H265Q variant with and without an MCP. The substitution of His265 to glutamine results in significant perturbations to the P-subsite. First, the orientation of the two asparagine side chains, Asn51 and Asn111, are flipped compared to the conformation observed in the WT and S112A variant structures (Figure 52A). Typically, an H-bonding network is observed between His265, Asn111 and Asn51: the His $N\varepsilon^2$ acts as an H-bond donor to the Asn111 $O\delta^1$, and the Asn111 $N\delta^1$ interacts with the

Oδ[1] of Asn51 (Figure 52B). Second, the electron density for three P-subsite residues (Asn51, Asn111 and Trp266) resulted in modeling two distinct conformers for each.

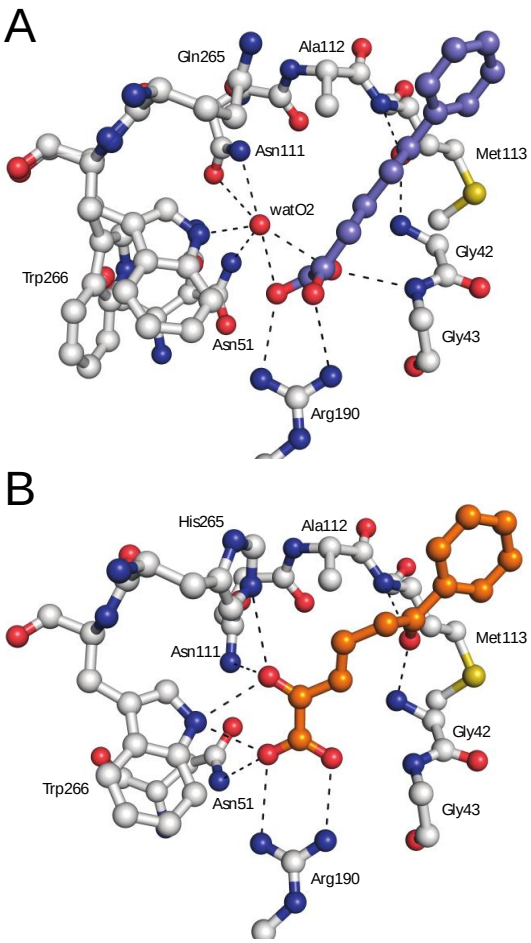

Figure 51. Ball-and-stick representations of the stable HOPDA binding modes observed in crystalline ES complexes. Polar contacts equal to or less than 3.4 Å are drawn as dashed lines. (A) The planar dienoate bound to BphD S112A/H265Q showing an additional water molecule in the P-subsite, below the dienoate plane (PDB ID: 3V1M). (B) The non-planar, electronically excited species, ES^{red}, bound by BphD S112A (PDB ID: 2PUH).

These two distinct P-subsite conformations were observed at a 3:2 ratio and the first or major set of sites is thought to be occupied by the substrate (colored green in Figure 52A). The hydrogen bonding network in the crystal structure of the S112A/H265Q:HOPDA binary complex differs significantly from that reported for the S112A variant. The Gln265 Oε[1] is

within H-bonding distance of the Asn111 $N\delta^1$, and the Asn111 $O\delta^1$ can interact with the $N\delta^1$ of Asn51. This inversion of H-bond donors and acceptors, centered at Asn111, also results in the orientation of the Asn51 $O\delta^1$ towards the Trp256 $N\varepsilon^1$, which is located at ~3.6 Å. Thus, in addition to the differences between the geometric isomers of HOPDA observed at the active site, the hydrogen bonding network at the P-subsite is significantly distinct from that correlated to ES^{red} or observed in WT structures. The results from the crystallographic analysis further underline the importance of His265 in maintenance of the P-subsite.

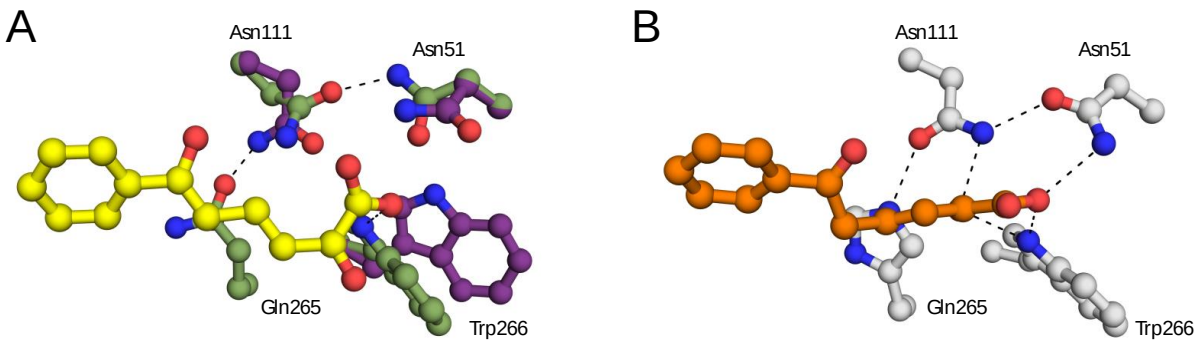

Figure 52. $BphD_{LB400}$ P-subsite variability upon substitution of His265. (A) The active site of a $BphD_{LB400}$ S112A/H265Q:HOPDA complex (PDB ID: 3V1M). The active site conformations were modeled at a 3:2 ratio and are coloured green and purple, respectively. (B) The active site of a $BphD_{LB400}$ S112A:HOPDA complex (PDB ID: 2PUH).

The distinct sets of P-subsite interactions that associated with either the planar and non-planar substrate binding modes in $BphD_{LB400}$ suggest that changes to the substrate conformation are accompanied by changes at the enzyme active site. In line with this proposal and the defined role of the MCP hydrolase lid in substrate recognition and specificity, a role for MCP hydrolase lid movement in catalysis is probable (see section 4.5). Further structural studies on the DxnB2 S105A/H255X variants may resolve the nature of binding in the histidine-independent ES^{red} species that are not observed in $BphD_{LB400}$.

4.1.4.3 The role of the catalytic histidine in the deacylation reaction

Overall, the data indicate that the MCP hydrolases utilize the His-Asp dyad to activate water for enzyme deacylation, a conserved role among serine hydrolases. Thus, while histidine-independent acylation was directly observed in $BphD_{LB400}$, and inferred in DxnB2, steady-state hydrolysis was essentially abrogated in catalytic histidine variants of both enzymes. In fact, the turnover of HOPDA and/or 9-Cl HOPDA occurred on the timescale of hours rather than milliseconds or seconds, as observed for the WT enzymes.

4.1.5 Pre-steady-state kinetic behaviour of wild type enzymes and half-site reactivity

The existence of a pre-steady-state kinetic burst is consistent with a covalent mechanism of catalysis in which a process following acylation is rate-limiting. Remarkably, the pre-steady-state kinetic behaviour of $BphD_{LB400}$ and DxnB2 differed with respect to the ratio of active enzyme during HOPDA cleavage. For the reaction of DxnB2 and HOPDA, 1:1 reactivity was observed during the first catalytic cycle. Interestingly, for 9-Cl HOPDA turnover, quantification of the amount of HPD produced during the burst phase indicated that only 67% of the enzyme was active. This peculiar reactivity may reflect either (i) an additional specificity determinant at C9 that invokes half-site reactivity or (ii) the relatively strong substrate inhibition by 9-Cl HOPDA, $K_{si} = 6 \pm 2$ μM[39]. The accuracy of the values reported for k_{burst}, k_{ss} and their associated amplitudes may be limited by the fact that the burst and steady-state rate constants differ by only a factor of five. Finally, full occupancy of the HsaD S114A active site was observed when HOPDA, a poor substrate, was incubated with crystals of this enzyme[41], suggesting that non-cognate substrates may also perturb reactivity.

The magnitude of the pre-steady-state burst in $BphD_{LB400}$ is consistent with the

proposed two-conformation model of catalysis; quantification of HPD produced during the pre-steady-state burst corresponded to only half of the available hydrolase active sites. Moreover, the relative ratio of modified to unmodified enzyme and peptides as measured by MS from chemically quenched reactions was also more consistent with half-site reactivity. This kinetic feature of the MCP hydrolases was first proposed based on the half-site occupancy of MhpC complexed with an inhibitor[69] and has since been observed in two HsaD:MCP complexes[41]. Unfortunately, crystallographic symmetry of all $BphD_{LB400}$:MCP complexes requires equivalence across all active sites, which limits information regarding differential active site binding affinities[66,81,86]. Nevertheless, in some enzymes, substrate binding is stoichiometric but reactivity is not; recently LuxG was shown to be a full-site binding, half-site reactive flavin reductase[124]. Here, analysis of substrate binding to DxnB2 P-subsite variants, specifically N43D/S105A, was indicative of 1:1 substrate binding. For $BphD_{LB400}$, the two-conformation model provides a more satisfactory explanation for the biphasic formation of HPD observed under single turnover conditions. In the two-conformation model, deacylation at one set of sites allows the second set to become active. In contrast, the kinetic behaviour of DxnB2 is less defined, changing with the substrate. However, the relevance of this aberrant behaviour is limited to *in vitro* studies of this enzyme since the physiologically relevant substrate is unknown.

4.2 Distinct kinetic features of DxnB2 wild type

Although the half-site reactive behaviour of $BphD_{LB400}$ is an interesting kinetic phenomenon, the associated kinetic complexity had contributed to a minimal assignment of observed kinetic steps during C-C bond hydrolysis. Moreover, the observation of biphasic turnover also influenced arguments in support of a general base mechanism, assigning

ketonization and HPD formation to distinct observable steps under single turnover conditions[65,83]. In the context of the covalent mechanism, the biphasic decay of ES^{red} can be attributed to HPD formation/acylation at distinct catalytic sites. Nevertheless, the apparent two-conformation behaviour of $BphD_{LB400}$ limits information on the ketonization reaction and the determinants thereof. The timescale of acylation observed by mass spectrometric studies on $BphD_{LB400}$ allowed for the provisional assignment of $1/\tau_2$ and $1/\tau_3$ to this process. The later phase also represents the rate-determining deacylation of the first set of active sites, $1/\tau_3 \sim k_{cat} \sim 6.5\ s^{-1}$. However, the determinants of $1/\tau_2$ are unclear, and are complicated by its sensitivity to solvent viscosity and temperature in $BphD_{LB400}$[81]. Thus, the mechanisms of substrate destabilization, ketonization, and ultimately acylation in the MCP hydrolases were gleaned from studies of DxnB2 as discussed below.

4.2.1 Defining observable kinetic steps in DxnB2

Pre-steady-state kinetic experiments indicated that the DxnB2-mediated turnover of HOPDA could be used to better define the mechanism of acylation. The reaction was apparently 1:1 with respect to protomer concentration, and therefore devoid of the kinetic complexity of the two-conformation model (Figure 53). The DxnB2-catalyzed hydrolysis of HOPDA is defined by the spectrophotometric observation of three kinetic steps. The first two, ES^{red} formation ($1/\tau_1 > 500\ s^{-1}$) and decay or enzyme-acylation ($1/\tau_2 \sim 69\ s^{-1}$), could be monitored under single turnover conditions at 487 and/or 270 nm. The third step, deacylation, was reported from steady-state characterization of the enzymatic reaction, k_{cat} $\sim 0.4\ s^{-1}$[39]. In particular, the rate constant for the second step was insensitive to solvent viscosity and had an SKIE of ~2.5. The involvement of a rate-limiting proton transfer in this

step further suggests that it represents substrate ketonization and that the generation of an electron sink limits acylation in the MCP hydrolases.

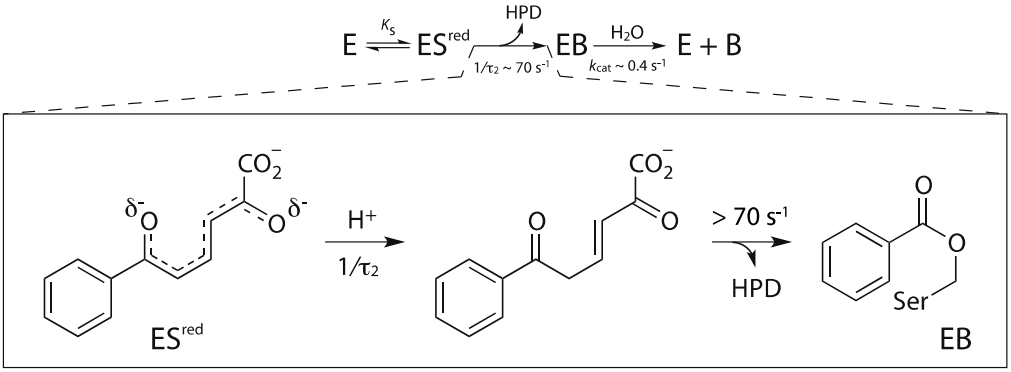

Figure 53. Kinetic scheme for DxnB2 hydrolysis of HOPDA showing the underlying chemical process that has been assigned to observable transient state kinetic phase that was previously assigned to acylation/HPD formation in $BphD_{LB400}$.

While the SKIE on $1/\tau_2$ indicates that substrate ketonization limits acylation in the MCP hydrolases, the specific source of the reactive proton remains unknown. In the context of the proposed substrate-assisted mechanism, the proton is abstracted from the Ser105 hydroxyl, which is expected to be deuterated under the reaction conditions[125]. In spite of the consistency between the proposed mechanism and observed effect, several other proton sources exist within the reaction media, including other exchangeable protein sites, the solvent itself and the substrate's own protons, which can exchange with the solvent.

4.2.2 A correlation between substrate basicity and ketonization by DxnB2

Kinetic characterization of the substrate ketonization reaction using a series of HOPDA analogues supported the notion of substrate-assisted nucleophile activation in the MCP hydrolases. An extended Brønsted analysis revealed a positive linear correlation between substrate basicity and the rate constant for substrate ketonatization. Here, substrate basicity is defined by the enol:enolate equilibrium, which is empirically measured as

pK_{a2}[37], and substrate ketonization is measured as $1/\tau_2$ during a single turnover of the tested substrates (HOPDA, 5-Cl, 8-Cl, 9-Cl and 5,8-diF). More explicitly, the results suggest that the reactivity of the substrates towards protonation at C5 mirrors the enol:enolate equilibrium (protonation of a hydroxyl). The positive linear correlation is in agreement with the assignment of $1/\tau_2$ to a proton transfer step. The observed slope, β_{nuc} ~1, is particularly interesting since White and Jencks interpreted a similar analysis of succinyl-CoA:3-ketoacid CoA transferase to be representative of a change in charge from -1 to 0 when the substrate reached the transition state[126]. This change in charge is expected to occur upon substrate ketonization in the MCP hydrolases. The observable β_{nuc} also argues against a concerted mechanism for acylation in the MCP hydrolases. Instead, the results indicate that ketonization and acylation occur in a stepwise mechanism whereby the substrate ketonization precedes nucleophilic attack at the carbonyl. Interestingly, the substrate's reactivity or inherent ability to stabilize negative charge may ultimately limit catalysis. For example, this protonation reaction was determined to be rate-limiting for the turnover of 5,8-diF HOPDA, which is characterized by a low pK_{a2}.

4.2.2.1 Substrate-derived determinants of biphasic kinetics

Curiously, substitution of the phenyl ring altered the kinetic behaviour of DxnB2. More particularly, the DxnB2-mediated cleavage of HOPDA or dienoate-substituted analogs was biphasic under single turnover conditions, while the hydrolysis of ring-substituted analogs occurred in three distinct transient kinetic phases. In the case of 8 or 9-Cl HOPDA, the large amplitudes associated with $1/\tau_2$ and $1/\tau_3$ suggest that both phases can be assigned to acylation. In this way, the ring-substituents appear to invoke sub-stoichiometric turnover that is somewhat reminiscent of the half-site reactivity or, more so, pNPB turnover observed in

$BphD_{LB400}$. The kinetic behaviour under single turnover conditions is also consistent with the pre-steady-state burst of HPD formation observed for 9-Cl HOPDA. In contrast for 5,8-diF HOPDA, the small change in absorbance associated with $1/\tau_2$, accounting for only 2.6 % of the total amplitude, and the absence of a change in absorbance at 270 nm, indicate substrate destabilization was biphasic rather than product formation. The rate constant associated with substrate ketonization was reduced > 500-fold for 5,8-diF HOPDA, and the relatively slow turnover may have also influenced the number of observable transients preceding chemistry. Thus, ES^{red} decay and acylation was monophasic for 5,8-diF HOPDA instead of the biphasic behaviour for 8-Cl and 9-Cl HOPDA. Again, it is unclear whether the observation of multiphasic ES^{red} decay can be correlated to a two-conformation model of catalysis or if the kinetic behaviour reflects the fact that HOPDAs are not the cognate substrate of DxnB2.

4.3 Insight into the identity of ES^{red}

Prior to this study, two proposals on the identity of ES^{red} had been forwarded. In one, the spectral perturbation was ascribed to bond strain in an enzyme-bound (2*E*, 4*E*)-2-oxido-6-oxodienoate[65,81]. This strain hypothesis was rationalized by analogy to the rhodopsin family, which covalently bind retinal through a Schiff base at a lysine residue, forming a cationic species. The mechanism of the red-shift in rhodopsins is still debated, and includes arguments for conformational and electrostatic manipulation of the protein-bound chromophore[127]. Recently, extreme bathochromic shifting, > 200 nm, was observed from rationally designed variants of human cellular retinal binding protein II (hCRBPII), and complementary crystallographic studies revealed apparently little dependence on conformational strain[128]. Instead, sequestration of the chromophore from bulk solvent and balanced distribution of the cationic charge across the polyene, mediated by evenly

distributed electrostatic potential in proteins that lacked a cationic-counter ion interaction, were largely responsible for the spectral perturbations in hCRBPII variants. The strain hypothesis has also been challenged by crystallographic analysis of the $BphD_{LB400}$ S112A:HOPDA or DxnB2 S105A:HOPDA binary complexes. These data, which have been correlated to that observed in solution by single crystal spectroscopy, suggest that ES^{red} has a geometric conformation that is most consistent with a (3*E*)-2,6-dioxo isomer[81,119]. Unfortunately, studies on the electrostatic potential of the MCP hydrolase active site are lacking.

A second hypothesis for the identity of ES^{red} which is more consistent with the results of restrained refinements of the dienoate, is polarization of the π electrons of an α,β-unsaturated ketone. In fact, binding of an inhibitor to crotonase resulted in a 90 nm bathochromic shift[85]. Interestingly, the introduction of a negatively charged residue into the P-subsite of DxnB2 (N43D) did not dramatically alter the identity of ES^{red}: while the relative population of species observed at ~475 and 500 nm in ES^{red} for the N43D/S105A and S105A variants were inverted, the λ_{max} values were not significantly shifted. While these results argue against a uniform electrostatic environment and polarization, this interpretation is complicated by the timescale of ES^{red} formation in the P-subsite variants, which is drastically reduced. In contrast to the contributions of the P-subsite, the identity of ES^{red} was very similar between DxnB2 and $BphD_{LB400}$, which possess distinct NP-subsites, arguing for a minimal contribution from this site in ES^{red} formation.

Here, a third proposal is presented that posits ES^{red} may represent an enzyme-stabilized carbanionic species with charge localized at C5. An enzyme-stabilized C5 carbanion is compatible with the results of the restrained refinements of MCPs to (3*E*)-2,6-

dioxo isomer. Mechanistically, such a carbanion is also consistent with the negative charge that must accumulate on C5 for substrate ketonization. Although enzymatic carbanion formation is typically energetically unfavorable, it is only ~9 kcal/mol for an enolate[129], and delocalization into a carbonyl stabilized by coordination to a Lewis acid, such as an 'oxyanion hole', is a common catalytic motif[77]. Additionally, the requisite energy could be easily supported by the large number of polar and nonpolar contacts provided by the NP- and P-subsites (Table 24, Appendix V). In $BphD_{LB400}$ and DxnB2, the theoretical change in energy associated with the observed electronic transitions characteristic of ES^{red} versus the free enolate in solution range between ~7 to 12 kcal/mol. Indeed, these values are comparable to the energy required to stabilize an enolate carbanion. Finally, the spectrophotometric contribution of a carbanion is also consistent with a red-shifted intermediate, explained by an n to π^* transition. A similar, 50 nm bathochromic shift was observed between different species of triphenylmethyl lithium: the contact ion pair exhibited a λ_{max} at 446 nm whereas the absorption spectra of the solvent separated ion pair was centered around 496 nm[130]. In nature, the quinoid intermediates of PLP-dependent enzymes provide prevalent examples of carbanionic intermediates with red-shifted absorption profiles. For example, the quinonoid intermediates of the C-C bond hydrolase kynureninase are characterized by a λ_{max} between 490 and 500 nm, which are shifted ~80 nm from their respective external aldimine intermediates[131,132]. Despite consistency with the observed data, the absence of any direct evidence makes any assignment of ES^{red} provisional.

4.3.1 Preliminary experimental investigation of ES^{red} by NMR

Two indirect approaches were used to examine the electronic nature of ES^{red} in DxnB2. First, ^{19}F NMR experiments hinted at the development of sp^3 character at C5 in a

DxnB2:5,8-diF HOPDA binary complex by comparing the chemical shifts of F_5 to purchased standards. Nevertheless, these results provide minimal insight into the electronic nature of ES^{red} as the assignment of the hybridization state of C5 via the ^{19}F probe is ambiguous. Conversely, the major signals observed in the $^{1}H^{13}C$ HSQC spectrum of uniformly ^{13}C-labeled HOPDA complexed to DxnB2 S105A were at chemical shifts values between 100 to 130 ppm, suggesting that the system of π electrons is intact in ES^{red}. Future experiments should include the direct investigation of a site-specifically labeled [^{13}C5]-HOPDA to clarify the electronic nature of C5 in ES^{red}.

4.3.2 EI GC/MS analysis of ES^{red} decay products

The reactivity of ES^{red}, specifically at C5, was particularly intriguing. The reaction of a carbanionic intermediate with molecular oxygen, an electrophile, is an expected result. However, in the absence of heavy isotopes, the observations do not uniquely identify O_2 as the reactive species. Second, and most importantly, the resolution of the experiment is not sufficient for the identification of the product as a 1-(3-chlorophenyl)-2-hydroxyethanone. Isolation of the ES^{red} decay product for chemical characterization by NMR in conjunction with higher resolution MS analyses of products formed in the presence of $^{18}O_2$ and $H_2{}^{18}O$ should facilitate confident identification in the future. Additional control experiments that include the decay of an ES complex that is not red-shifted should also be performed. Finally, in the MCP hydrolases, the apparent sensitivity to O_2 may be further complicated by the possibility of an enzymatic affinity for and/or ability to utilize O_2. Specifically, while the cofactor-less dioxygenases of the α/β-hydrolase superfamily share only ~10% amino acid identity with DxnB2, comparison of their three-dimensional structure reveals a high degree of conservation. Structural superposition of DxnB2 and 1-H-3-hydroxy-4-oxoquinaldine 2,4-

dioxygenase (HOD) from *Arthobacter nitroguajacolicus* Rü61a and 1-H-3-hydroxy-4-oxoquinoline 2,4-dioxygenase from *Pseduomonas putida* 33/1 revealed root mean square deviations between 2.9 to 3.1 Å across 217-224 structurally conserved positions (~75% of the DxnB2 structure). Thus, the affinity and ability of DxnB2 and other MCP hydrolases to bind and utilize O_2 should be carefully characterized before concluding on the nature of ES^{red}. This is especially pertinent since substrate deprotonation to form an anionic intermediate is thought to precede O_2 activation and O_2 has been proposed to occupy the 'oxyanion hole' in these cofactor-less dioxygenases[63].

4.4 The role of P-subsite residues in catalysis

The current studies greatly extend previous investigations of the P-subsite residues. More particularly, previous studies of MhpC reported on the respective roles of three P-subsite residues: (i) Trp264 in substrate binding, (ii) Arg188 in MCP ketonization, and (iii) Asn109 in positioning the active site loop containing Ser110[65]. Substitution of each of these residues resulted in enzymes with greater C-S and/or C-O bond cleavage activity than the WT[114]. Nevertheless, the aforementioned roles for the P-subsite residues were forwarded based on steady-state kinetic or specific activity measurements, and the interpretation was guided by limited structural data. The experiments presented here better resolve the individual roles of Arg180 and Asn43 in DxnB2, although structural data of the P-subsite variants in complex with HOPDA and/or 9-Cl HOPDA would greatly augment these kinetic data. Finally, the contribution of the catalytic histidine to the P-subsite was identified and has been discussed above.

4.4.1 Kinetic behaviour of P-subsite variants

The role of Asn43 and Arg180 in substrate destabilization and ketonization is consistent with structural data showing that each directly contacts the dienoate moiety and/or other P-subsite residues. In fact, structural data for several MCP hydrolases suggests that Asn43 may also be involved indirectly in catalysis by properly orienting His255 during turnover through a conserved interaction with Asn104. In the crystal structures of DxnB2 S105A:HOPDA or 5,8-diF HOPDA complexes[117,119], which display the productive non-planar substrate binding mode characteristic of ES^{red}, the Asn43 $O\delta^1$ is within H-bonding distance of the Asn104 $N\delta^2$, and the Asn104 $O\delta^1$ may or may not interact with the His255 $N\delta^1$, depending on the residue's protonation state, which is unknown. In addition, Asn43 $N\delta^2$ is within H-bonding distance of the HOPDA carboxylate in crystalline complexes that are characteristic of ES^{red}[41,65,66,117,119] but not in complexes that are characterized by planar HOPDA dienoate binding[86,119]. For Arg180, the gunidinium group also H-bonds with the substrate carboxylate in ES^{red} or with both the carboxylate and C2-oxo in planar conformations, excluding the the DxnB2 S105A:3-Cl HOPDA complex[117].

Disruption of polar contacts between the P-subsite residues and the substrate perturbed the rate of HOPDA hydrolysis. The removal of a positively charged residue, R180M and R180Q, or the addition of a negatively charged residue, N43D, significantly reduced hydrolytic activity. In the case of Arg180 variants, the >100-fold increases in K_m values was due to reduced substrate affinity, reflecting the role of the guanidinium group in carboxylate binding. In contrast, the N43D variant bound and destabilized the substrate, shown by ES^{red} formation upon binding to the N43D/S105A variant. The measured k_{cat}/K_m values for N43D were reduced by 15000- and 4300-fold for HOPDA and 9-Cl HOPDA,

respectively, compared to the WT enzyme. Interestingly, while the Asn43 is typically located ~4 Å from Arg180 in MCP hydrolase structures, the closest distances between the two residues have been observed in class III homologues, and is as little as 3.6 Å in the structure of CarC (PDB ID: 1J1I). Accordingly, replacement of Asn43 with an aspartic acid may result in the introduction of a new interaction between Asp43 and Arg180. While this variant interaction does not appear to disrupt substrate destabilization in the N43D/S105A variant, the timescale of ES^{red} formation was in fact reduced (see section 4.4.2).

The greater activity of the second group of P-subsite variants reflects the more conservative nature of the amino acid substitutions: N43A, N43H and R180K. In each case, the substitution reduced the specificity of the enzyme for cleavage and the degree of substrate inhibition. For example, substrate inhibition was ~50-fold lower for R180K than in the WT for 9-Cl HOPDA. In light of the strong substrate inhibition observed for the DxnB2-mediated hydrolysis of ring-substituted HOPDAs (typically K_{si} < 10 μM) and the relatively modest 10-fold decrease in substrate specificity for R180K, this variant may be an interesting target for directed evolution experiments aimed at expanding the substrate range of the MCP hydrolases.

4.4.2 The role of the P-subsite in substrate destabilization and ketonization

The full suite of P-subsite interactions is required for efficient C-C bond cleavage. In particular, the ability of the enzyme to destabilize the substrate is critical for ketonization. The ability of S105A/P-subsite variants to accumulate ES^{red} further highlights the importance of this intermediate on the reaction pathway. Moreover, the absence of ES^{red} from kinetic traces under single turnover conditions argue that substrate destabilization is at least partially rate-limiting for ketonization, and thus, acylation in the N43A, N43D and R180K variants.

Overall, these results highlight the evolution of a finely tuned active site with extensive enzyme-substrate interactions.

4.5 Structural determinants in MCP hydrolases

The structural and catalytic role of the P-subsite, including the catalytic histidine has been discussed within the context of differences observed in HOPDA turnover by $BphD_{LB400}$ and DxnB2. Upon the analysis of the available structures, several other distinguishing features of phylogenetically diverse MCP hydrolase subfamilies became evident and may be linked to improved specificity of DxnB2 towards recalcitrant PCB metabolites.

4.5.1 Differences in MCP hydrolase structures and activity.

The structural analyses of the MCP hydrolases further support a significant contribution of the NC-loop to catalysis. This loop, which joins the core and lid domains, has been proposed to contribute to catalysis in several other α/β-hydrolase families including the lipases[46], haloalkane dehalogenases[133] and epoxide hydrolases[118]. Furthermore, substitution of the NC-loop was required to convert an esterase into an epoxide hydrolase[47]. In the MCP hydrolases, domain-swapping experiments between BphD ($BphD_{LA4}$) and MfphA from *Dyella ginsengisoli* LA-4 further established that the identity of the lid domain is a strong determinant of substrate specificity[134], and a single amino acid substitution located in the NC-loop of $BphD_{LA4}$ reduced k_{cat}/K_m for HOPDA by nearly 300-fold[135]. Molecular dynamics simulations have also been used to argue the relevance of NC-loop flexibility in the haloalkane dehalogenases[133] and significant α5 helix motions were observed in the *Candida antarctica* lipase B (CALB)[136]. Interestingly, while the CALB and MCP hydrolase lid domains are distinct, the first helix of each, which follows the NC-loop, occupy very similar three-dimensional space in relation to the α/β-hydrolase core.

Indeed, the sum of the available data for the α/β-hydrolases sets a precedent for the involvement of the NC-loop in substrate binding and catalysis by the MCP hydrolases.

The identification of the NC-loop as a determinant of MCP hydrolase oligomeric state provides a further example of the ability of the α/β-hydrolase core to accommodate family-specific insertions to determine substrate and chemical specificity[42,44]. Thus, comparison of the seven structurally characterized MCP hydrolases representing three different oligomeric states revealed high structural variation for the NC-loop. The NC-loop residues appear to be most highly conserved among the class I enzymes, and to at least partially mediate tetramer formation. In particular, the NC-loop contributes to two distinct tetrameric interfaces and the phenylalanine residue of its F-X-P-X-P motif lies at the core of the biological assembly. Moreover, differences in the NC-loop are propagated to the lid domain architecture: the position of and interactions involving the first helix of the MCP hydrolase lid, α5, are not conserved between the phylogenetically distinct classes. Each class possesses a distinguishing set of intra-lid interactions, which are likely to mitigate substrate specificity.

4.5.2 The DxnB2 lid domain and specificity for 3-Cl HOPDAs

The single turnover data together with the proposed catalytic mechanism of MCP hydrolases indicate that the higher specificity of DxnB2 for 3-Cl HOPDAs (k_{cat}/K_m) versus BphD is due to higher rate of ES^{red} formation in the former. More specifically, the hydrolysis of HOPDAs by DxnB2[137] and $BphD_{LB400}$[66,81,86] is defined by three observable steps for which the rate constants have been determined: (i) ES^{red} formation (> 500 s^{-1}); (ii) ES^{red} decay (50 to 70 s^{-1}), which is coupled to acylation/HPD formation and limited by the ketonization reaction; and (iii) deacylation (k_{cat} ~0.4 to 6.5 s^{-1}). In contrast, the hydrolysis of 3-Cl HOPDAs by these enzymes is characterized by just two observable processes:

(i) formation of an alternative, presumably non-productive, binding mode named ES^e in $BphD_{LB400[86]}$ and characterized by a hypo- and/or hypsochromically-shifted absorption spectrum in DxnB2; and (ii) ES^e decay, which is coupled to HPD formation and corresponds to k_{cat}. The failure to detect ES^{red} during 3-Cl HOPDA cleavage indicates that it is consumed at a rate that precludes detection. Thus, the similarity between the observed rate constants for HPD formation and steady-state turnover indicate that ES^{red} formation is rate-limiting to catalysis[39]. For 3-Cl HOPDA, this rate constant ($1/\tau_2$) is at least 3000-fold slower than for HOPDA in DxnB2[138]. However, formation of ES^{red} from 3-Cl HOPDA in DxnB2 (0.152 s^{-1}) is 20-fold faster than in $BphD_{LB400}$ (0.0077 s^{-1}), accounting for the increased reactivity of the former towards recalcitrant PCB metabolites. Interestingly, ES^{red} formation during turnover of 3,9,11-triCl HOPDA was only ~3-fold slower than 3-Cl HOPDA. This small reduction is in line with the general observation that ring-substituents are minor contributors to the substrate specificity of $BphD_{LB400}$ and DxnB2 with the exception of 9-Cl HOPDA for the latter enzyme[37,39].

The variable disorder in helix α5 observed in crystal structures of DxnB2 suggests that this region has increased mobility relative to other MCP hydrolases with the exception of CarC. Such movement may be restricted in the tetrameric enzymes based on the location the tetrameric interfaces. Interestingly, superposition of three DxnB2 S105A:HOPDA binary complexes reveals a difference in the position of helix α5 of up to ~6 Å based on placement of the Cα atoms. The position of helix α5 drastically affects the form of the NP-subsite. Specifically, it carries Leu146 and Val149, which are further removed from the substrate in crystal structures of DxnB2 than in $BphD_{LB400}$[86,117]. Accordingly, the comparatively limited restraint placed by the DxnB2 NP-site on the substrate is also likely to contribute to

the relative increase in hydrolytic activity towards recalcitrant PCB metabolites. Thus, the possible mobility of this helix may account for the increased accessibility to ES^{red} in DxnB2 versus $BphD_{LB400}$.

The high structural variance of the NC-loop contributes to the ability of DxnB2 to overcome the stabilization of 3-Cl HOPDAs in non-productive, planar dienoate binding modes. Moreover, the NC-loop is prominent at MCP hydrolase tetrameric interfaces suggesting that it at least partially stabilizes the oligomeric state of class I family members. The attributes of this loop have implications for both environmental bioremediation and the design of therapeutics. Replacement of $BphD_{LB400}$ (or other *bona fide* BphD enzymes) by DxnB2 in the Bph pathway may alleviate the metabolic bottleneck caused by 3-Cl HOPDAs. The dimeric MCP hydrolases could also represent better starting points for future enzyme engineering efforts. The plasticity of the NC-loop should also be considered in designing inhibitors of HsaD, which appears to be required for survival of *Mycobacterium tuberculosis* in macrophages[139]. Finally, while the results further establish the catalytic adaptability of the α/β-hydrolase superfamily and highlight the influence of lid architecture within a specific enzyme family, the correlation of loop and lid movements to catalysis is relevant to a broader understanding of enzyme dynamics[140].

4.6 Concluding Remarks

This thesis described the chemical mechanism of the MCP hydrolases. Thus, considering the conservation of the P-subsite throughout the family, it provides an outline for the development of mechanism-based inhibitors for the *M. tuberculosis* enzyme. In addition, through the kinetic characterization of two homologues of differing oligomeric state, DxnB2 and $BphD_{LB400}$, substrate ketonization was found to be rate-limiting for the acylation

reaction. A more definitive role for the P-subsite, including the catalytic histidine, in the ketonization reaction has been established. Finally, while the identity of ES^{red} remains unknown, progress towards its identification has been reported, and future experiments have been proposed.

REFERENCES

1. Boerjan W, Ralph J, Baucher M (2003) Lignin biosynthesis. Annu Rev Plant Biol 54: 519-546.
2. Carmona M, Zamarro MT, Blazquez B, Durante-Rodriguez G, Juarez JF, et al. (2009) Anaerobic catabolism of aromatic compounds: a genetic and genomic view. Microbiol Mol Biol Rev 73: 71-133.
3. Vaillancourt FH, Bolin JT, Eltis LD (2006) The ins and outs of ring-cleaving dioxygenases. Crit Rev Biochem Mol Biol 41: 241-267.
4. Dagley S (1978) Microbial catabolism, the carbon cycle and environmental pollution. Naturwissenschaften 65: 85-95.
5. Mason JR, Cammack R (1992) The electron-transport proteins of hydroxylating bacterial dioxygenases. Annu Rev Microbiol 46: 277-305.
6. Palfey BA, McDonald CA (2010) Control of catalysis in flavin-dependent monooxygenases. Arch Biochem Biophys 493: 26-36.
7. Harayama S, Rekik M (1989) Bacterial aromatic ring-cleavage enzymes are classified into two different gene families. J Biol Chem 264: 15328-15333.
8. Gibson J, C SH (2002) Metabolic diversity in aromatic compound utilization by anaerobic microbes. Annu Rev Microbiol 56: 345-369.
9. Olivera ER, Minambres B, Garcia B, Muniz C, Moreno MA, et al. (1998) Molecular characterization of the phenylacetic acid catabolic pathway in Pseudomonas putida U: the phenylacetyl-CoA catabolon. Proc Natl Acad Sci U S A 95: 6419-6424.
10. Rather LJ, Knapp B, Haehnel W, Fuchs G (2010) Coenzyme A-dependent aerobic metabolism of benzoate via epoxide formation. J Biol Chem 285: 20615-20624.
11. Lunt D, Evans WC (1970) The microbial metabolism of biphenyl. Biochem J 118: 54P-55P.
12. Denef VJ, Park J, Tsoi TV, Rouillard JM, Zhang H, et al. (2004) Biphenyl and benzoate metabolism in a genomic context: outlining genome-wide metabolic networks in Burkholderia xenovorans LB400. Appl Environ Microbiol 70: 4961-4970.
13. Furukawa K, Miyazaki T (1986) Cloning of a gene cluster encoding biphenyl and chlorobiphenyl degradation in Pseudomonas pseudoalcaligenes. J Bacteriol 166: 392-398.
14. Furukawa K, Tomizuka N, Kamibayashi A (1979) Effect of chlorine substitution on the bacterial metabolism of various polychlorinated biphenyls. Appl Environ Microbiol 38: 301-310.
15. Baker P, Seah SY (2012) Rational design of stereoselectivity in the class II pyruvate aldolase BphI. J Am Chem Soc 134: 507-513.
16. Hurtubise Y, Barriault D, Powlowski J, Sylvestre M (1995) Purification and characterization of the Comamonas testosteroni B-356 biphenyl dioxygenase components. J Bacteriol 177: 6610-6618.
17. Faroon OM, Keith LS, Smith-Simon C, De Rose CT (2003) Polychlorinated Biphenyls: Human Health Aspects. World Health Organization, Geneva.
18. AgencyforToxicSubstancesandDiseaseRegistry (2000) Toxicological Profile for Polychlorinated Biphenyls (PCBs). Atlanta, GA: U.S. Department of Human Health and Human Services.

19. Hopf NB, Ruder AM, Succop P (2009) Background levels of polychlorinated biphenyls in the U.S. population. Sci Total Environ 407: 6109-6119.
20. Haddock JD, Gibson DT (1995) Purification and characterization of the oxygenase component of biphenyl 2,3-dioxygenase from Pseudomonas sp. strain LB400. J Bacteriol 177: 5834-5839.
21. Fortin PD, Horsman GP, Yang HM, Eltis LD (2006) A glutathione S-transferase catalyzes the dehalogenation of inhibitory metabolites of polychlorinated biphenyls. J Bacteriol 188: 4424-4430.
22. Gomez-Gil L, Kumar P, Barriault D, Bolin JT, Sylvestre M, et al. (2007) Characterization of biphenyl dioxygenase of Pandoraea pnomenusa B-356 as a potent polychlorinated biphenyl-degrading enzyme. J Bacteriol 189: 5705-5715.
23. Iwasaki T, Takeda H, Miyauchi K, Yamada T, Masai E, et al. (2007) Characterization of two biphenyl dioxygenases for biphenyl/PCB degradation in A PCB degrader, Rhodococcus sp. strain RHA1. Biosci Biotechnol Biochem 71: 993-1002.
24. Pieper DH, Seeger M (2008) Bacterial metabolism of polychlorinated biphenyls. J Mol Microbiol Biotechnol 15: 121-138.
25. Iwai S, Chai B, Sul WJ, Cole JR, Hashsham SA, et al. (2010) Gene-targeted-metagenomics reveals extensive diversity of aromatic dioxygenase genes in the environment. ISME J 4: 279-285.
26. Standfuss-Gabisch C, Al-Halbouni D, Hofer B (2012) Characterization of biphenyl dioxygenase sequences and activities encoded by the metagenomes of highly polychlorobiphenyl-contaminated soils. Appl Environ Microbiol 78: 2706-2715.
27. Kim D, Chae JC, Zylstra GJ, Kim YS, Kim SK, et al. (2004) Identification of a novel dioxygenase involved in metabolism of o-xylene, toluene, and ethylbenzene by Rhodococcus sp. strain DK17. Appl Environ Microbiol 70: 7086-7092.
28. Yoo M, Kim D, Zylstra GJ, Kang BS, Kim E (2011) Biphenyl hydroxylation enhanced by an engineered o-xylene dioxygenase from Rhodococcus sp. strain DK17. Res Microbiol 162: 724-728.
29. Cho HJ, Kim K, Sohn SY, Cho HY, Kim KJ, et al. (2010) Substrate binding mechanism of a type I extradiol dioxygenase. J Biol Chem 285: 34643-34652.
30. Kumamaru T, Suenaga H, Mitsuoka M, Watanabe T, Furukawa K (1998) Enhanced degradation of polychlorinated biphenyls by directed evolution of biphenyl dioxygenase. Nat Biotechnol 16: 663-666.
31. Barriault D, Sylvestre M (2004) Evolution of the biphenyl dioxygenase BphA from Burkholderia xenovorans LB400 by random mutagenesis of multiple sites in region III. J Biol Chem 279: 47480-47488.
32. Mohammadi M, Sylvestre M (2005) Resolving the profile of metabolites generated during oxidation of dibenzofuran and chlorodibenzofurans by the biphenyl catabolic pathway enzymes. Chem Biol 12: 835-846.
33. Viger JF, Mohammadi M, Barriault D, Sylvestre M (2012) Metabolism of chlorobiphenyls by a variant biphenyl dioxygenase exhibiting enhanced activity toward dibenzofuran. Biochem Biophys Res Commun 419: 362-367.
34. Furukawa K, Suenaga H, Goto M (2004) Biphenyl dioxygenases: functional versatilities and directed evolution. J Bacteriol 186: 5189-5196.

35. Fortin PD, MacPherson I, Neau DB, Bolin JT, Eltis LD (2005) Directed evolution of a ring-cleaving dioxygenase for polychlorinated biphenyl degradation. J Biol Chem 280: 42307-42314.
36. Bedard DL, Haberl ML (1990) Influence of Chlorine Substitution Pattern on the Degradation of Polychlorinated Biphenyls by Eight Bacterial Strains. Microbial Ecology 20: 87-102.
37. Seah SY, Labbe G, Nerdinger S, Johnson MR, Snieckus V, et al. (2000) Identification of a serine hydrolase as a key determinant in the microbial degradation of polychlorinated biphenyls. J Biol Chem 275: 15701-15708.
38. Seah SY, Labbe G, Kaschabek SR, Reifenrath F, Reineke W, et al. (2001) Comparative specificities of two evolutionarily divergent hydrolases involved in microbial degradation of polychlorinated biphenyls. J Bacteriol 183: 1511-1516.
39. Seah SY, Ke J, Denis G, Horsman GP, Fortin PD, et al. (2007) Characterization of a C-C bond hydrolase from Sphingomonas wittichii RW1 with novel specificities towards polychlorinated biphenyl metabolites. J Bacteriol 189: 4038-4045.
40. Van der Geize R, Yam K, Heuser T, Wilbrink MH, Hara H, et al. (2007) A gene cluster encoding cholesterol catabolism in a soil actinomycete provides insight into Mycobacterium tuberculosis survival in macrophages. Proc Natl Acad Sci U S A 104: 1947-1952.
41. Lack NA, Yam KC, Lowe ED, Horsman GP, Owen RL, et al. (2010) Characterization of a carbon-carbon hydrolase from Mycobacterium tuberculosis involved in cholesterol metabolism. J Biol Chem 285: 434-443.
42. Ollis DL, Cheah E, Cygler M, Dijkstra B, Frolow F, et al. (1992) The alpha/beta hydrolase fold. Protein Eng 5: 197-211.
43. Nardini M, Dijkstra BW (1999) Alpha/beta hydrolase fold enzymes: the family keeps growing. Curr Opin Struct Biol 9: 732-737.
44. Holmquist M (2000) Alpha/Beta-hydrolase fold enzymes: structures, functions and mechanisms. Curr Protein Pept Sci 1: 209-235.
45. Larsen NA, Lin H, Wei R, Fischbach MA, Walsh CT (2006) Structural characterization of enterobactin hydrolase IroE. Biochemistry 45: 10184-10190.
46. Li B, Yang G, Wu L, Feng Y (2012) Role of the NC-loop in catalytic activity and stability in lipase from Fervidobacterium changbaicum. PLoS One 7: e46881.
47. Jochens H, Stiba K, Savile C, Fujii R, Yu JG, et al. (2009) Converting an esterase into an epoxide hydrolase. Angew Chem Int Ed Engl 48: 3532-3535.
48. Semeriva M, Chapus C, Bouvier-Lapierre C, Desnuelle P (1974) On the transient formation of an acetyl enzyme intermediate during the hydrolysis of p-nitrophenyl acetate by pancreatic lipase. Biochem Biophys Res Commun 58: 808-813.
49. Chapus C, Semeriva M, Bovier-Lapierre C, Desnuelle P (1976) Mechanism of pancreatic lipase action. 1. Interfacial activation of pancreatic lipase. Biochemistry 15: 4980-4987.
50. Koller W, Kolattukudy PE (1982) Mechanism of action of cutinase: chemical modification of the catalytic triad characteristic for serine hydrolases. Biochemistry 21: 3083-3090.

51. Froede HC, Wilson IB (1984) Direct determination of acetyl-enzyme intermediate in the acetylcholinesterase-catalyzed hydrolysis of acetylcholine and acetylthiocholine. J Biol Chem 259: 11010-11013.
52. Li J, Szittner R, Derewenda ZS, Meighen EA (1996) Conversion of serine-114 to cysteine-114 and the role of the active site nucleophile in acyl transfer by myristoyl-ACP thioesterase from Vibrio harveyi. Biochemistry 35: 9967-9973.
53. Nazi I, Wright GD (2005) Catalytic mechanism of fungal homoserine transacetylase. Biochemistry 44: 13560-13566.
54. De Pascale G, Nazi I, Harrison PH, Wright GD (2011) beta-Lactone natural products and derivatives inactivate homoserine transacetylase, a target for antimicrobial agents. J Antibiot (Tokyo) 64: 483-487.
55. Lejon S, Ellis J, Valegard K (2008) The last step in cephalosporin C formation revealed: crystal structures of deacetylcephalosporin C acetyltransferase from *Acremonium chrysogenum* in complexes with reaction intermediates. J Mol Biol 377: 935-944.
56. Verschueren KH, Seljee F, Rozeboom HJ, Kalk KH, Dijkstra BW (1993) Crystallographic analysis of the catalytic mechanism of haloalkane dehalogenase. Nature 363: 693-698.
57. Stennicke HR, Mortensen UH, Breddam K (1996) Studies on the hydrolytic properties of (serine) carboxypeptidase Y. Biochemistry 35: 7131-7141.
58. Medrano FJ, Alonso J, Garcia JL, Romero A, Bode W, et al. (1998) Structure of proline iminopeptidase from Xanthomonas campestris pv. citri: a prototype for the prolyl oligopeptidase family. EMBO J 17: 1-9.
59. Pathak D, Ashley G, Ollis D (1991) Thiol protease-like active site found in the enzyme dienelactone hydrolase: localization using biochemical, genetic, and structural tools. Proteins 9: 267-279.
60. Chakravarty B, Gu Z, Chirala SS, Wakil SJ, Quiocho FA (2004) Human fatty acid synthase: structure and substrate selectivity of the thioesterase domain. Proc Natl Acad Sci U S A 101: 15567-15572.
61. Yin DT, Kazlauskas RJ (2012) Revised molecular basis of the promiscuous carboxylic acid perhydrolase activity in serine hydrolases. Chemistry 18: 8130-8139.
62. Andexer JN, Staunig N, Eggert T, Kratky C, Pohl M, et al. (2012) Hydroxynitrile lyases with alpha/beta-hydrolase fold: two enzymes with almost identical 3D structures but opposite enantioselectivities and different reaction mechanisms. Chembiochem 13: 1932-1939.
63. Steiner RA, Janssen HJ, Roversi P, Oakley AJ, Fetzner S (2010) Structural basis for cofactor-independent dioxygenation of N-heteroaromatic compounds at the alpha/beta-hydrolase fold. Proc Natl Acad Sci U S A 107: 657-662.
64. Fleming SM, Robertson TA, Langley GJ, Bugg TD (2000) Catalytic mechanism of a C-C hydrolase enzyme: evidence for a gem-diol intermediate, not an acyl enzyme. Biochemistry 39: 1522-1531.
65. Li C, Li JJ, Montgomery MG, Wood SP, Bugg TD (2006) Catalytic role for arginine 188 in the C-C hydrolase catalytic mechanism for Escherichia coli MhpC and Burkholderia xenovorans LB400 BphD. Biochemistry 45: 12470-12479.
66. Horsman GP, Bhowmik S, Seah SY, Kumar P, Bolin JT, et al. (2007) The tautomeric half-reaction of BphD, a C-C bond hydrolase. Kinetic and structural evidence

supporting a key role for histidine 265 of the catalytic triad. J Biol Chem 282: 19894-19904.
67. Seah SY, Terracina G, Bolin JT, Riebel P, Snieckus V, et al. (1998) Purification and preliminary characterization of a serine hydrolase involved in the microbial degradation of polychlorinated biphenyls. J Biol Chem 273: 22943-22949.
68. Lack N, Lowe ED, Liu J, Eltis LD, Noble ME, et al. (2008) Structure of HsaD, a steroid-degrading hydrolase, from Mycobacterium tuberculosis. Acta Crystallogr Sect F Struct Biol Cryst Commun 64: 2-7.
69. Dunn G, Montgomery MG, Mohammed F, Coker A, Cooper JB, et al. (2005) The structure of the C-C bond hydrolase MhpC provides insights into its catalytic mechanism. J Mol Biol 346: 253-265.
70. Fushinobu S, Saku T, Hidaka M, Jun SY, Nojiri H, et al. (2002) Crystal structures of a meta-cleavage product hydrolase from Pseudomonas fluorescens IP01 (CumD) complexed with cleavage products. Protein Sci 11: 2184-2195.
71. Riddle RR, Gibbs PR, Willson RC, Benedik MJ (2003) Purification and properties of 2-hydroxy-6-oxo-6-(2'-aminophenyl)hexa-2,4-dienoic acid hydrolase involved in microbial degradation of carbazole. Protein Expr Purif 28: 182-189.
72. Diaz E, Timmis KN (1995) Identification of functional residues in a 2-hydroxymuconic semialdehyde hydrolase. A new member of the alpha/beta hydrolase-fold family of enzymes which cleaves carbon-carbon bonds. J Biol Chem 270: 6403-6411.
73. Hedstrom L (2002) Serine protease mechanism and specificity. Chem Rev 102: 4501-4524.
74. Grogan G (2005) Emergent mechanistic diversity of enzyme-catalysed beta-diketone cleavage. Biochem J 388: 721-730.
75. Phillips RS (2011) Structure, mechanism, and substrate specificity of kynureninase. Biochim Biophys Acta 1814: 1481-1488.
76. Lam WW, Bugg TD (1997) Purification, characterization, and stereochemical analysis of a C-C hydrolase: 2-hydroxy-6-keto-nona-2,4-diene-1,9-dioic acid 5,6-hydrolase. Biochemistry 36: 12242-12251.
77. Begley TP, Ealick SE (2004) Enzymatic reactions involving novel mechanisms of carbanion stabilization. Curr Opin Chem Biol 8: 508-515.
78. Van Vleet JL, Reinhardt LA, Miller BG, Sievers A, Cleland WW (2008) Carbon isotope effect study on orotidine 5'-monophosphate decarboxylase: support for an anionic intermediate. Biochemistry 47: 798-803.
79. Bornscheuer UT, Kazlauskas RJ (2004) Catalytic promiscuity in biocatalysis: using old enzymes to form new bonds and follow new pathways. Angew Chem Int Ed Engl 43: 6032-6040.
80. Li JJ, Bugg TD (2005) Stereochemistry of the reaction catalysed by 2-hydroxy-6-keto-6-phenyl-hexa-2,4-dienoic acid 5,6-hydrolase (BphD). Chem Commun (Camb): 130-132.
81. Horsman GP, Ke J, Dai S, Seah SY, Bolin JT, et al. (2006) Kinetic and structural insight into the mechanism of BphD, a C-C bond hydrolase from the biphenyl degradation pathway. Biochemistry 45: 11071-11086.
82. Catelani D, Colombi A (1974) Metabolism of biphenyl. Structure and physicochemical properties of 2-hydroxy-6-oxo-6-phenylhexa-2,4-dienoic acid, the meta-cleavage

product from 2,3-dihydroxybiphenyl by Pseudomonas putida. Biochem J 143: 431-434.
83. Henderson IM, Bugg TD (1997) Pre-steady-state kinetic analysis of 2-hydroxy-6-keto-nona-2,4-diene-1,9-dioic acid 5,6-hydrolase: kinetic evidence for enol/keto tautomerization. Biochemistry 36: 12252-12258.
84. Dahl KH, Dunn MF (1984) Carboxymethylated liver alcohol dehydrogenase: kinetic and thermodynamic characterization of reactions with substrates and inhibitors. Biochemistry 23: 6829-6839.
85. D'Ordine RL, Tonge PJ, Carey PR, Anderson VE (1994) Electronic rearrangement induced by substrate analog binding to the enoyl-CoA hydratase active site: evidence for substrate activation. Biochemistry 33: 12635-12643.
86. Bhowmik S, Horsman GP, Bolin JT, Eltis LD (2007) The molecular basis for inhibition of BphD, a C-C bond hydrolase involved in polychlorinated biphenyls degradation: large 3-substituents prevent tautomerization. J Biol Chem 282: 36377-36385.
87. Bugg TD, Fleming SM, Robertson TA, Langley GJ (2002) 2-hydroxy-6-keto-nona-2,4-diene 1,9-dioic acid 5,6-hydrolase: evidence from 18O isotope exchange for gem-diol intermediate. Methods Enzymol 354: 106-118.
88. Hyland LJ, Tomaszek TA, Jr., Roberts GD, Carr SA, Magaard VW, et al. (1991) Human immunodeficiency virus-1 protease. 1. Initial velocity studies and kinetic characterization of reaction intermediates by 18O isotope exchange. Biochemistry 30: 8441-8453.
89. Li JJ, Li C, Blindauer CA, Bugg TD (2006) Evidence for a gem-diol reaction intermediate in bacterial C-C hydrolase enzymes BphD and MhpC from 13C NMR spectroscopy. Biochemistry 45: 12461-12469.
90. Speare DM, Olf P, Bugg TD (2002) Hammett analysis of a C-C hydrolase-catalysed reaction using synthetic 6-aryl-2-hydroxy-6-ketohexa-2,4-dienoic acid substrates. Chem Commun (Camb): 2304-2305.
91. Speare DM, Fleming SM, Beckett MN, Li JJ, Bugg TD (2004) Synthetic 6-aryl-2-hydroxy-6-ketohexa-2,4-dienoic acid substrates for C-C hydrolase BphD: investigation of a general base catalytic mechanism. Org Biomol Chem 2: 2942-2950.
92. Bender ML, Nakamura K (1962) The effect of strructure on the rates of some α-chymotrypsin-catalyzed reactions. J Am Chem Soc 84: 2577-2582.
93. Li JJ, Bugg TD (2007) Investigation of a general base mechanism for ester hydrolysis in C-C hydrolase enzymes of the alpha/beta-hydrolase superfamily: a novel mechanism for the serine catalytic triad. Org Biomol Chem 5: 507-513.
94. Seydoux F, Malhotra OP, Bernhard SA (1974) Half-site reactivity. CRC Crit Rev Biochem 2: 227-257.
95. Fersht A (1999) Structure and mechanism in protein science: a guide to enzyme catalysis and protein folding: W.H. Freeman and Company.
96. Silverman RB (2000) The organic chemistry of enzyme-catalyzed reactions: Academic Press.
97. Couture MM, Colbert CL, Babini E, Rosell FI, Mauk AG, et al. (2001) Characterization of BphF, a Rieske-type ferredoxin with a low reduction potential. Biochemistry 40: 84-92.

98. Patil DN, Tomar S, Sylvestre M, Kumar P (2010) Expression, purification, crystallization and preliminary crystallographic studies of cis-biphenyl-2,3-dihydrodiol-2,3-dehydrogenase from Pandoraea pnomenusa B-356. Acta Crystallogr Sect F Struct Biol Cryst Commun 66: 1517-1520.
99. Maniatis T, Fritsch EF, Sambrook J (1982) Molecular cloning: a laboratory manual. New York: Cold Spring Harbor Laboratory.
100. Bauchop T, Elsden SR (1960) The growth of micro-organisms in relation to their energy supply. J Gen Microbiol 23: 457-469.
101. Horsman GP (2008) Characterization of BphD, a C-C boond hydrolase involved in the degradation of polychlorinated biphenyls. Vancouver: The University of British Columbia.
102. Cornish-Bowden A (1995) Analysis of enzyme kinetic data. New York: Oxford University Press.
103. Team RDC (2010) R: A language and environment for statistical computing. Vienna, Austria: R Foundation for Statistical Computing.
104. Chan QW, Howes CG, Foster LJ (2006) Quantitative comparison of caste differences in honeybee hemolymph. Mol Cell Proteomics 5: 2252-2262.
105. Russell RB, Barton GJ (1992) Multiple protein sequence alignment from tertiary structure comparison: assignment of global and residue confidence levels. Proteins 14: 309-323.
106. Roberts E, Eargle J, Wright D, Luthey-Schulten Z (2006) MultiSeq: unifying sequence and structure data for evolutionary analysis. BMC Bioinformatics 7: 382.
107. Humphrey W, Dalke A, Schulten K (1996) VMD: visual molecular dynamics. J Mol Graph 14: 33-38, 27-38.
108. Emsley P, Cowtan K (2004) Coot: model-building tools for molecular graphics. Acta Crystallogr D Biol Crystallogr 60: 2126-2132.
109. Nandhagopal N, Senda T, Hatta T, Yamada A, Masai E, et al. (1997) Three-dimensional structure of microbial 2-hydroxyl-6-oxo-phenylhexa-2,4-dienoic acid (HPDA) hydrolase (BphD enzyme) from *Rhodococcus* sp. strain RHA1, in the PCB degradation pathway,. Proceedings of the Japan Academy, Ser B 73: 154.
110. Habe H, Morii K, Fushinobu S, Nam JW, Ayabe Y, et al. (2003) Crystal structure of a histidine-tagged serine hydrolase involved in the carbazole degradation (CarC enzyme). Biochem Biophys Res Commun 303: 631-639.
111. Pollard JR, Henderson IM, Bugg TD (1997) Chemical and biochemical properties of 2-hydroxypentadienoic acid, a homologue of enolpyruvic acid. Chem Commun: 1885-1886.
112. Ghosh S (2012): Purdue University.
113. Li C, Montgomery MG, Mohammed F, Li JJ, Wood SP, et al. (2005) Catalytic mechanism of C-C hydrolase MhpC from Escherichia coli: kinetic analysis of His263 and Ser110 site-directed mutants. J Mol Biol 346: 241-251.
114. Li C, Hassler M, Bugg TD (2008) Catalytic promiscuity in the alpha/beta-hydrolase superfamily: hydroxamic acid formation, C--C bond formation, ester and thioester hydrolysis in the C--C hydrolase family. Chembiochem 9: 71-76.
115. Zhou H, Qu Y, Kong C, Wu Y, Zhu K, et al. (2012) Promiscuous esterase activities of the C-C hydrolases from Dyella ginsengisoli. Biotechnol Lett 34: 1107-1113.

116. Abell LM, Schloss JV (1991) Oxygenase side reactions of acetolactate synthase and other carbanion-forming enzymes. Biochemistry 30: 7883-7887.
117. Bhowmik S (2008) Structural investigation into the mechanism of catalysis and inhibition of two carbon-carbon bond hydrolases. Ann Arbor: Purdue University.
118. Barth S, Fischer M, Schmid RD, Pleiss J (2004) Sequence and structure of epoxide hydrolases: a systematic analysis. Proteins 55: 846-855.
119. Ghosh S (2012) Structural Studies of BphD LB400 Variants : Insights into the reaction mechanism of MCP hydrolases.: Purdue University.
120. Sprinson DB, Rittenberg D (1951) Nature of the activation process in enzymatic reactions. Nature 167: 484.
121. Blow DM, Birktoft JJ, Hartley BS (1969) Role of a buried acid group in the mechanism of action of chymotrypsin. Nature 221: 337-340.
122. Fastrez J, Fersht AR (1973) Demonstration of the acyl-enzyme mechanism for the hydrolysis of peptides and anilides by chymotrypsin. Biochemistry 12: 2025-2034.
123. Ostrowski W, Barnard EA (1973) Evidence for a phosphoryl-enzyme intermediate in the catalytic reaction of prostatic acid phosphatase. Biochemistry 12: 3893-3898.
124. Nijvipakul S, Ballou DP, Chaiyen P (2010) Reduction kinetics of a flavin oxidoreductase LuxG from Photobacterium leiognathi (TH1): half-sites reactivity. Biochemistry 49: 9241-9248.
125. Liepinsh E, Otting G, Wuthrich K (1992) NMR spectroscopy of hydroxyl protons in aqueous solutions of peptides and proteins. J Biomol NMR 2: 447-465.
126. White H, Jencks WP (1976) Mechanism and specificity of succinyl-CoA:3-ketoacid coenzyme A transferase. J Biol Chem 251: 1688-1699.
127. Nielsen MB (2009) Model systems for understanding absorption tuning by opsin proteins. Chem Soc Rev 38: 913-924.
128. Wang W, Nossoni Z, Berbasova T, Watson CT, Yapici I, et al. (2012) Tuning the electronic absorption of protein-embedded all-trans-retinal. Science 338: 1340-1343.
129. Schloss JV, Hixon MS (1997) Enol chemistry and enzymology, in Comprehensive Biological Catalysis; Sinnod M, editor. London: Academic Press.
130. Buncel E, Menon B (1979) Carbanion Mechanisms. 9. Spectrophotometric Study of Triphenylmethyl Alkali Metal Salts. Contact and Solvent-Seperated Ion Pairs in Ethereal Solvents. J Org Chem 44: 317-320.
131. Phillips RS, Holtermann G (2005) Differential effects of temperature and hydrostatic pressure on the formation of quinonoid intermediates from L-Trp and L-Met by H463F mutant Escherichia coli tryptophan indole-lyase. Biochemistry 44: 14289-14297.
132. Kumar S, Gawandi VB, Capito N, Phillips RS (2010) Substituent effects on the reaction of beta-benzoylalanines with Pseudomonas fluorescens kynureninase. Biochemistry 49: 7913-7919.
133. Otyepka M, Damborsky J (2002) Functionally relevant motions of haloalkane dehalogenases occur in the specificity-modulating cap domains. Protein Sci 11: 1206-1217.
134. Zhou H, Qu Y, Shen E, Kong C, Zhang X, et al. (2012) Tuning the substrate selectivity of meta-cleavage product hydrolase by domain swapping. Appl Microbiol Biotechnol.

135. Zhou H, Qu Y, Kong C, Shen E, Wang J, et al. (2013) The key role of a non-active-site residue Met148 on the catalytic efficiency of meta-cleavage product hydrolase BphD. Appl Microbiol Biotechnol.
136. Skjot M, De Maria L, Chatterjee R, Svendsen A, Patkar SA, et al. (2009) Understanding the plasticity of the alpha/beta hydrolase fold: lid swapping on the Candida antarctica lipase B results in chimeras with interesting biocatalytic properties. Chembiochem 10: 520-527.
137. Ruzzini AC, Bhowmik S, Yam KC, Ghosh S, Bolin JT, et al. (2013) unpublished.
138. Ruzzini AC, Horsman GP, Eltis LD (2012) The catalytic serine of meta-cleavage product hydrolases is activated differently for C-O bond cleavage than for C-C bond cleavage. Biochemistry 51: 5831-5840.
139. Rengarajan J, Bloom BR, Rubin EJ (2005) Genome-wide requirements for Mycobacterium tuberculosis adaptation and survival in macrophages. Proc Natl Acad Sci U S A 102: 8327-8332.
140. Nashine VC, Hammes-Schiffer S, Benkovic SJ (2010) Coupled motions in enzyme catalysis. Curr Opin Chem Biol 14: 644-651.
141. Wilkinson AJ, Fersht AR, Blow DM, Winter G (1983) Site-directed mutagenesis as a probe of enzyme structure and catalysis: tyrosyl-tRNA synthetase cysteine-35 to glycine-35 mutation. Biochemistry 22: 3581-3586.

APPENDIX I: CHEMICAL PROPERTIES OF SUBSTRATES

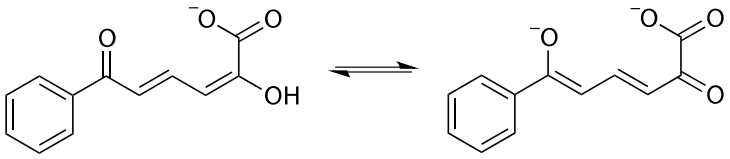

Figure 54. The HOPDA enol:enolate equilibrium, defined by pK_{a2}. An ^{18}O-incorporation event into the C2-oxo was observed in KPi (I = 0.1 M), pH 7.5, suggesting that the 2-oxo-6-oxido- isomer exists under those conditions.

Table 20. HOPDA pK_{a2} values and extinction coefficients in KPi (I = 0.1 M), pH 7.5

Substrate/Product	λ_{max} (nm)	ε ($mM^{-1}cm^{-1}$)	pK_{a2}
HOPDA	434	25.7	7.3
3-Cl HOPDA	432	40.6	6.1
5-Cl HOPDA	402	40.1	6.1
8-Cl HOPDA	393	40.3	6.5
9-Cl HOPDA	436	28.2	6.8
10-Cl HOPDA	438	26.3	6.9
3,9,11 tri-Cl HOPDA	438	35.6	ND
8-F HOPDA	398	ND	ND
5,8-diF HOPDA	405	31.2	5.0 ± 0.2
HPD	270	19.7	ND

APPENDIX II: MASS SPECTROMETRY RESULTS

Table 21. *b*-series ion fragment matches to a $BphD_{LB400}$ peptide analyzed by ESI/MS/MS[a,b,c]

b-series ion	Peptide		
	WT (unmodified)	WT S112-benzoyl	H265Q S112-benzoyl
b^{9+}	977.52 / 977.5163	977.54 / 977.5163	977.51 / 977.5163
b^{10+}	1091.58 / 1091.5592	1091.58 / 1091.5592	1091.57 / 1091.5592
b^{11+}	1178.61 / 1178.5913		1282.64 / 1282.6175
b^{12+}	1309.66 / 1309.6317	1413.69 / 1413.6580	1413.73 / 1413.6580
b^{13+}	1366.65 / 1366.6532	1470.69 / 1470.6794	
b^{14+}	1423.67 / 1423.6747	1527.73 / 1527.7009	
b^{15+}	1494.74 / 1494.7118	1598.74 / 1598.7380	
b^{17+}	1666.82 / 1666.7966		
b^{11++}	641.83 / 641.8124	589.81 / 589.7993	
b^{13++}	735.85 / 735.8434		735.83 / 735.8434
b^{14++}	764.36 / 764.3541	712.34 / 712.3410	764.33 / 764.3541
b^{15++}	764.85 / 799.8726		
b^{17++}	885.97 / 885.9150		
b^{19++}	999.95 / 999.4785		
b^{11*++}	581.30 / 581.2860		
b^{16*++}	789.89 / 789.8701	841.91 / 841.8832	
b^{17*++}		877.43 / 877.4018	
b^{11o+}	1160.61 / 1160.5807		
b^{16o+}	1577.72 / 1577.7489		
b^{11o++}	580.80 / 580.7940		
b^{16o++}	789.39 / 789.3781	841.41 / 841.3912	841.37 / 841.3912
b^{17o++}		876.91 / 876.9098	876.91 / 876.9098
	Search Result Statistics		
Ions score	85	63	50
Expect Value	3.8 E-6	0.00057	0.022
Matches (out of 212)	25	34	23
RMS error (ppm)	207	220	276

a – values of the observed fragments based on manual inspection of raw data and fits to Gaussian peaks followed by MASCOT match results

b – MASCOT search of *B. xenovorans* LB400 proteins resulted in a match to the BphD peptide, DIDRAHLVGNSMGGATALNF

c – Symbols * and ^{o} indicate ions with an additional loss of NH_3 and H_2O, respectively.

Table 22. Example of modeling EI GC/MS data to ^{18}O incorporation events

	Observed relative abundance of ions from EI/GC/MS (%)						
m/z	179 [M]	180 [M+1]	181 [M+2]	182 [M+3]	183 [M+4]	184 [M+5]	
Control[a]	83.5	12.4	3.9	0.35			
WT + HOPDA[b]	12	2.7	71	10.7	3.6	0.3	
Modeling the relative abundance (R.A.) of benzoate species in the sample (%)							
Model 1: Two species accounting for a single ^{18}O incorporation event							
	R.A. [M]	R.A. [M+1]	R.A. [M+2]	R.A. [M+3]	R.A. [M+4]	R.A. [M+5]	Average R.A.[c,d]
$^{16}O/^{16}O$	14	22	16	14			15 ± 1
$^{16}O/^{18}O$			84	86	92	86	85 ± 1
Model 2: Three species including 3% of doubly ^{18}O-incorporated benzoate[e]							
$^{16}O/^{16}O$	14	22	16	14			15 ± 1
$^{16}O/^{18}O$			84	86	28	-21	82 ± 3

a – Control values represent the average of all benzoate ion fragments observed in H_2O

b – Benzoate derived from HOPDA incubated with WT BphD for 20 minutes without any pre-incubation

c – The relative abundance of each species ($^{16}O/^{18}O$ and $^{18}O/^{18}O$) was calculated from the observed intensity of each ion (Obs) from the WT reaction and the control (Co) as follows:

R.A. $[M]_{16O/16O} = [M]_{Obs}/[M]_{Co}$

R.A. $[M+1]_{16O/16O} = [M+1]_{Obs}/[M+1]_{Co}$,

R.A. $[M+2]_{16O/16O} = ([M]_{Co} - [M+2]_{Obs})/([M]_{Co}-[M+2]_{Co})$

R.A. $[M+3]_{16O/16O} = ([M+1]_{Co} - [M+3]_{Obs})/([M+1]_{Co}-[M+3]_{Co})$

R.A. $[M+4]_{16O/16O} = ([M+2]_{Co} - [M+4]_{Obs})/([M+2]_{Co}-[M+4]_{Co})$

R.A. $[M+5]_{16O/16O} = ([M+3]_{Co} - [M+5]_{Obs})/([M+3]_{Co}-[M+5]_{Co})$

R.A. of $[M+N]_{16O/18O} = 1 - [M+N]_{16O/16O}$

d – The averages and errors were weighted based on fragment ion intensity

e – The calculation in Table S4 used a model in which 3% of the benzoate contains two equivalents of ^{18}O. Ion fragments derived from this species only contribute to the observed signals at M+4 and M+5: no M+6 or M+7 ions were observed.

Table 23. Relative abundance of ion fragments analyzed by EI GC/MS

Sample and Incubation time			Relative abundance (%)[a] of benzoate ion fragments (m/z) 105 [M]	106 [M+1]	107 [M+2]	108 [M+3]	109 [M+4]		^{18}O incorporation[b]
benzoate	300 min	H_2O	92 ± 1	7 ± 1	1.0 ± 0.1				
		$H_2{}^{18}O$	92.2 ± 0.2	6.7 ± 0.1	1.1 ± 0.1				ND
WT + benzoate	300 min	H_2O	92.3 ± 0.1	6.6 ± 0.2	1.1 ± 0.1				
		$H_2{}^{18}O$	91.5 ± 0.7	7.2 ± 0.5	1.3 ± 0.2				ND
WT + HOPDA	20 min	H_2O	92.2 ± 0.4	6.8 ± 0.8	1.0 ± 0.4				
		$H_2{}^{18}O$	53 ± 2	4.9 ± 0.4	39 ± 3	2.7 ± 0.2	0.3 ± 0.2		42 ± 1%
WT + HOPDA	5 min PI 20 min rxn	H_2O	92 ± 2	7 ± 1	1.0 ± 0.3				
		$H_2{}^{18}O$	52.9 ± 0.3	5.5 ± 0.9	38 ± 1	3.1 ± 0.2	0.17 ± 0.02		42 ± 2%
WT + HOPDA	20 min PI 20 min rxn	H_2O	91 ± 2	8 ± 1	0.9 ± 0.4				
		$H_2{}^{18}O$	52.5 ± 0.6	4.8 ± 0.3	38.5 ± 0.4	3.8 ± 0.1	0.29 ± 0.03		43 ± 2%
			179 [M]	180 [M+1]	181 [M+2]	182 [M+3]	183 [M+4]	184 [M+5]	
benzoate	300 min	H_2O	83.2 ± 0.6	12.9 ± 0.5	3.4 ± 0.1	0.44 ± 0.08			
		$H_2{}^{18}O$	83.1 ± 0.5	12.4 ± 0.3	4.1 ± 0.1	0.4 ± 0.2			ND
WT + benzoate	300 min	H_2O	84.1 ± 0.4	11.9 ± 0.4	3.6 ± 0.1	0.31 ± 0.01			
		$H_2{}^{18}O$	83 ± 0.2	12.3 ± 0.1	4.3 ± 0.1	0.4 ± 0.04			ND
WT + HOPDA	20 min	H_2O	84 ± 1	12 ± 1	3.9 ± 0.1	0.3 ± 0.1			
		$H_2{}^{18}O$	12 ± 1	2.7 ± 0.1	71 ± 2	10.7 ± 0.5	3.6 ± 0.1	0.3 ± 0.1	85 ± 1%
WT + HOPDA	5 min PI 20 min rxn	H_2O	82.7 ± 0.9	12 ± 1	4.4 ± 0.5	0.4 ± 0.1	0.23 ± 0.01		
		$H_2{}^{18}O$	14 ± 3	3.9 ± 0.3	68 ± 2	11 ± 1	3.1 ± 0.1	0.3 ± 0.2	80 ± 2%
WT + HOPDA	20 min PI 20 min rxn	H_2O	82.7 ± 0.1	12.8 ± 0.4	4.0 ± 0.4	0.33 ± 0.07	0.12 ± 0.04		
		$H_2{}^{18}O$	16.7 ± 0.4	3.3 ± 0.2	65 ± 1	10.0 ± 0.1	4 ± 1	0.5 ± 0.2	79 ± 2%
			193 [M-1]	194 [M]	195 [M+1]	196 [M+2]	197 [M+3]	198 [M+4]	
benzoate	300 min	H_2O	15.7 ± 0.1	70.2 ± 0.7	11.2 ± 0.3	3 ± 1			
		$H_2{}^{18}O$	18 ± 2	65.6 ± 0.4	12.6 ± 0.1	3 ± 1			ND
WT + benzoate	300 min	H_2O	15.5 ± 0.3	69 ± 1	12 ± 2	4.0 ± 0.7			
		$H_2{}^{18}O$	14.3 ± 0.8	69.5 ± 0.3	11.8 ± 0.3	3.9 ± 0.4	0.39 ± 0.06		ND
WT + HOPDA	20 min	H_2O	17 ± 5	66 ± 1	11 ± 2	5 ± 1			
		$H_2{}^{18}O$	3 ± 1	11 ± 4	15 ± 2	57 ± 8	11 ± 2	2.7 ± 0.8	85 ± 4 %
WT + HOPDA	5 min PI 20 min rxn	H_2O	16 ± 2	69 ± 2	11 ± 4	3 ± 5			
		$H_2{}^{18}O$	3.0 ± 0.4	15 ± 1	12 ± 2	55 ± 1	11.5 ± 0.8	3.0 ± 0.9	72 ± 9 %
WT + HOPDA	20 min PI 20 min rxn	H_2O	14 ± 3	71 ± 1	10.7 ± 0.1	5 ± 1			
		$H_2{}^{18}O$	4 ± 1	10 ± 1	12.5 ± 0.4	59 ± 2	10 ± 1	4.4 ± 0.1	80 ± 10 %
			Relative abundance (%) of HOPDA ion fragments (m/z)						
			245 [M]	246 [M+1]	247 [M+2]	248 [M+3]	249 [M+4]	250 [M+5]	
HOPDA	20 min	H_2O	78 ± 2	16.0 ± 0.2	5 ± 2	0.5 ± 0.2			
		$H_2{}^{18}O$	65.0 ± 0.1	12.7 ± 0.2	17.9 ± 0.1	3.2 ± 0.1	1.0 ± 0.2	0.12 ± 0.01	18 ± 1%
			257 [M]	258 [M+1]	259 [M+2]	260 [M+3]	261 [M+4]		
HOPDA	20 min	H_2O	71 ± 5	22 ± 5	6.7 ± 0.1				
		$H_2{}^{18}O$	62.3 ± 0.3	15 ± 3	18 ± 8	3.1 ± 0.1	1.1 ± 0.1		17.± 1 %
			347 [M]	348 [M+1]	349 [M+2]	350 [M+3]	351 [M+4]		
HOPDA	20 min	H_2O	73 ± 6	18 ± 2	8 ± 2	1 ± 1			
		$H_2{}^{18}O$	58 ± 3	17 ± 2	16 ± 2	6.3 ± 0.8	2 ± 1		17 ± 5%

a – errors for relative abundance measurements are a standard deviation from two replicates

b – errors for ^{18}O incorporation represent the root mean square error from fitting the experimentally observed data to a single ^{18}O incorporation or to a model that accounts for 2% incorporation of a second ^{18}O equivalent in parentheses

c – overall rms error based on weighted residual plot analysis, where residual = predicted % intensity from model – observed value

APPENDIX III: PRE- OR POST-CATALYTIC EVENTS

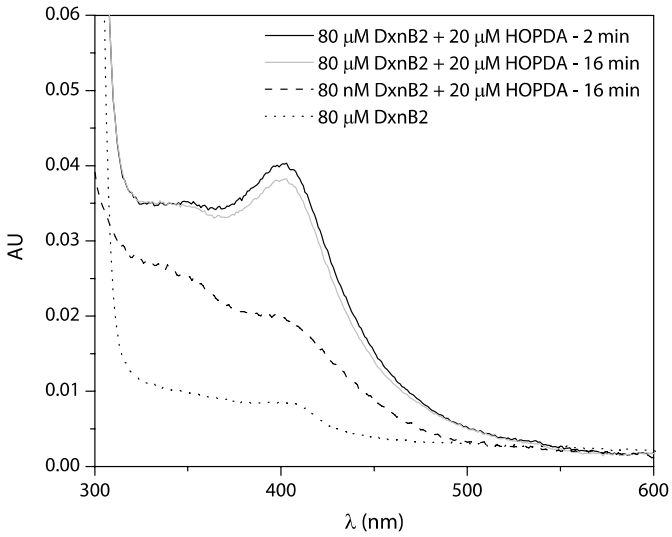

Figure 55. Visible spectra of post-reaction mixtures of DxnB2 and 20 μM HOPDA under single or multiple turnover conditions. The signal at 405 nm has tentatively been assigned to a DxnB2:HPD complex based on the enzyme-dependent increase in absorptivity.

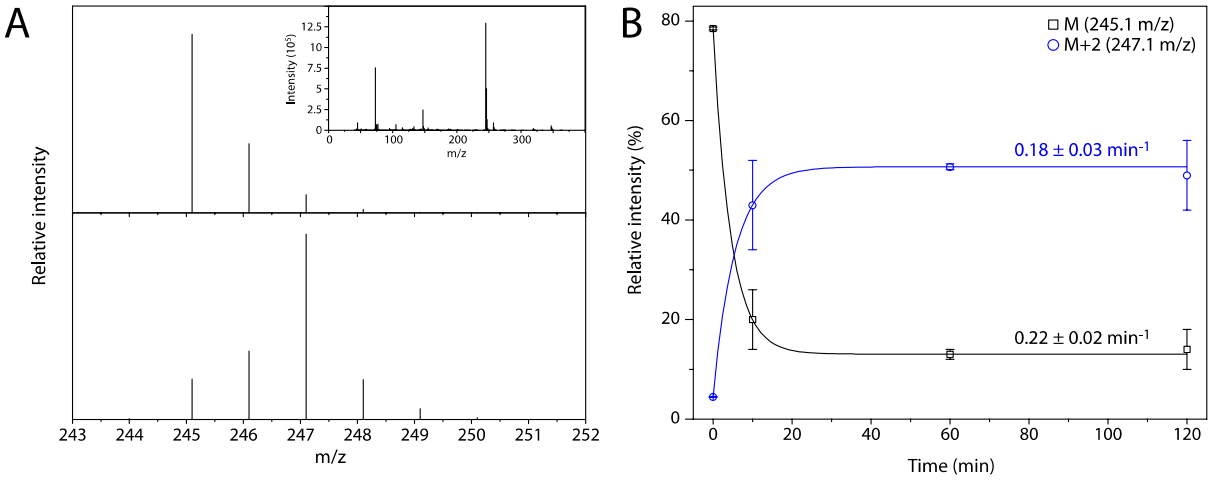

Figure 56. EI GC/MS demonstrating deuterium exchange into HOPDA over 2 hours. (A) The HOPDA base peak (245 m/z) at t = 0 h (top panel) and t = 2 h (bottom panel). The mass spectrum of HOPDA at t = 0 h is inset. (B) The time-dependent exchange of deuterium into the HOPDA base peak and calculation of the exponential rate of exchange using the M and M+2 species. Two equivalents of deuterium were incorporated into approximately 63% of the sample. The incorporation was previously determined to occur at C3 and C5 of the dienoate[76].

APPENDIX IV: $^{1}H^{13}C$ HSQC SPECTRUM OF DxnB2 S105A:HOPDA COMPLEX

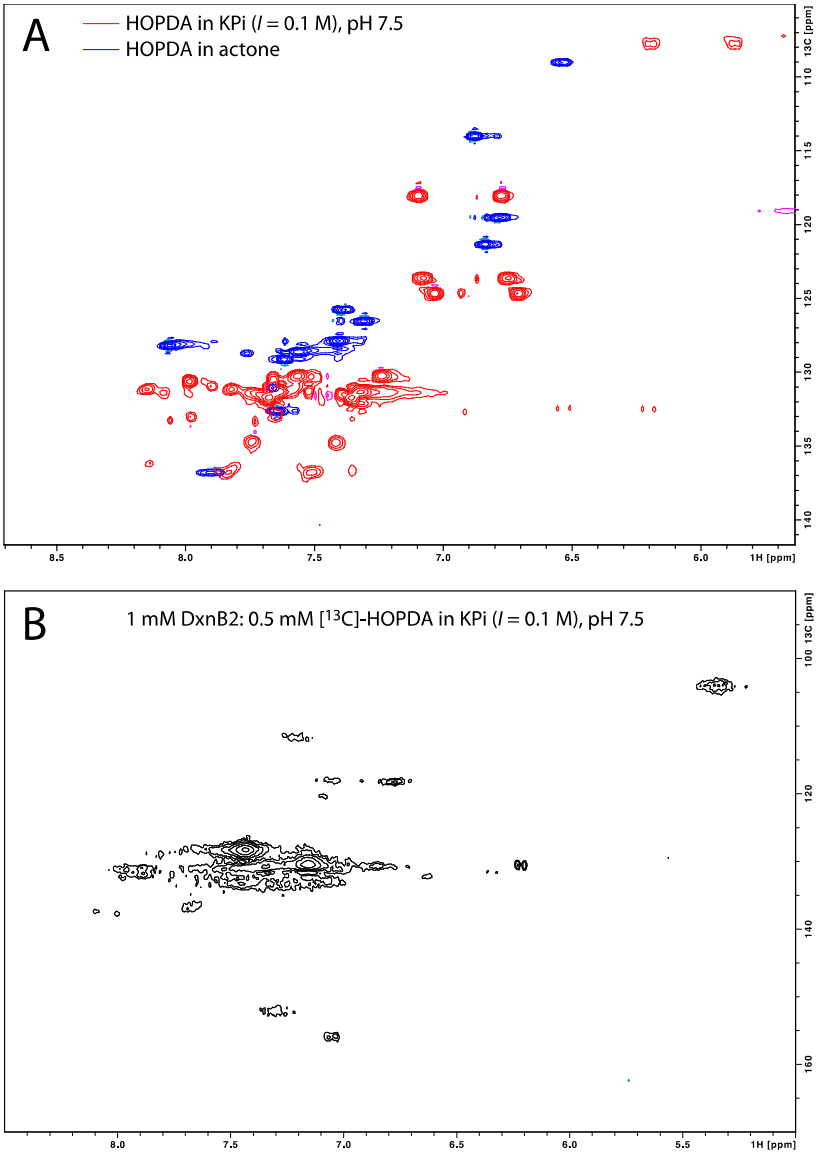

Figure 57. (A) ^{1}H ^{13}C HSQC spectra of HOPDA in acetone (blue) and phosphate buffer (red). (B) The ^{1}H ^{13}C HSQC spectrum of a DxnB2 S105A:[^{13}C]-HOPDA binary complex. Definitive assignment of the carbons in the binary complex is not possible from the HSQC experiment. Background signal origination from the enzyme is also clearly visible in this region, and was especially significant for nuclei with ^{1}H shifts < 5 ppm (not shown**).**

APPENDIX V: STEADY-STATE KINETICS AND EQUILIBRIUM BINDING

Equations used for the determination of steady-state kinetic parameters

(1) Michaelis-Menten equation

$$v_0 = \frac{V_{max}[S]}{K_m + [S]}$$

(2) Substrate Inhibition

$$v_0 = \frac{V_{max}[S]}{K_m + [S]\left(1 + \frac{[S]}{K_{si}}\right)}$$

Equations used for the determination of dissociation constants

(3) Hyperbolic binding equation

$$A = \frac{A_{max}[E]}{K_d + [E]}$$

where A is the difference in absorbance (ΔAbs) of the sample upon the addition of enzyme, [E], and A_{max} is the absorbance once all the substrate is bound.

(4) Quadratic binding equation

$$A = A_{max}\frac{S + E + K_d - \sqrt{(S + E + K_d)^2 - 4SE}}{2E}$$

where S is the concentration of substrate and E is the concentration of enzyme

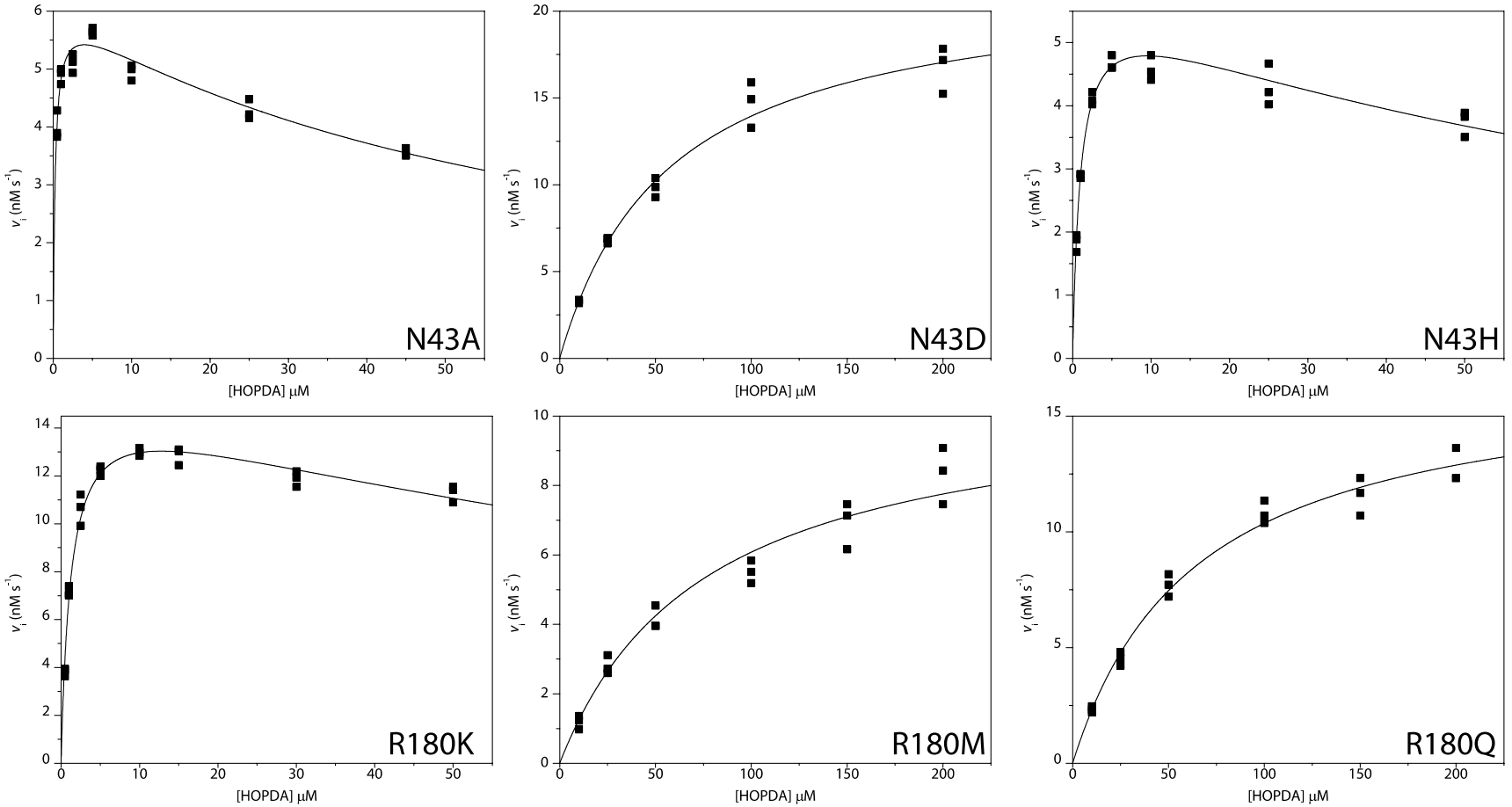

Figure 58. Steady-state kinetic curves (v_0 versus [S]) for the DxnB2 P-subsite variant catalyzed hydrolysis of HOPDA. The fit to each dataset is shown as a line.

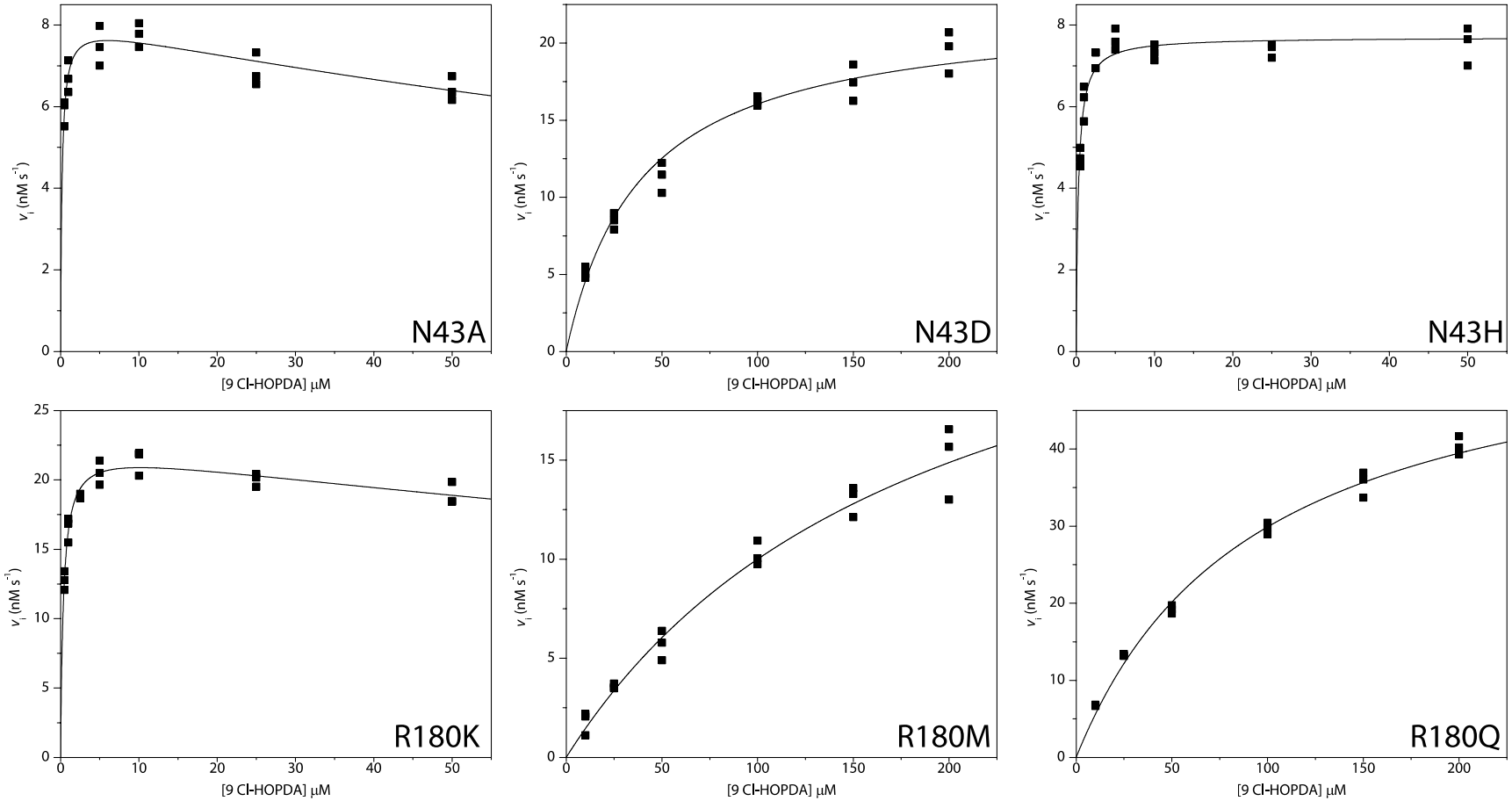

Figure 59. Steady-state kinetic curves (v_0 versus [S]) for the DxnB2 P-subsite variant catalyzed hydrolysis of 9-Cl HOPDA. The fit to each dataset is shown as a line.

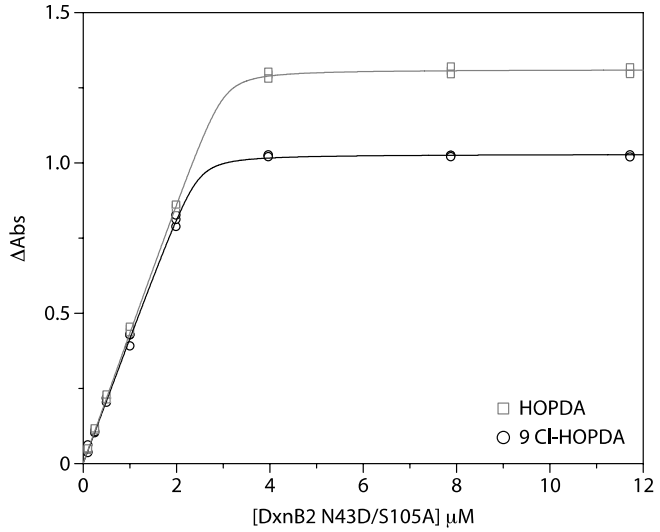

Figure 60. Titration of 4 μM HOPDA (grey) or 3 μM 9-Cl HOPDA (black) with DxnB2 N43D/S105A in KPi (I = 0.1 M), pH 7.5 at 25 °C. The data were fit with a quadratic binding equation. In each case, the K_d was determined to be ~0.02 μM, indicating the limit of the assay. Overall, the results from fitting the quadratic equation to each dataset also poorly modeled the amount of substrate known to be present in each assay: estimates of the known amount 4 or 3 μM of HOPDA or 9-Cl HOPDA were only 75 and 82%, respectively. Thus, a K_d < 20 nM was used to describe the binding of both substrates to the N43D/S105A.

Table 24. Transition state stabilization by MCP hydrolase side chains to HOPDA.

Enzyme	k_{cat}/K_m ($M^{-1}s^{-1}$)	$\lvert\Delta G_R\rvert$ (kcal mol^{-1})
BphD wild type, pH 7.5[a]	3.2×10^6	
S112C	9.5×10^4	2.1
BphD wild-type, pH 8.0[b]	3.3×10^6	
R190Q	5.7×10^2	5.1
R190K	2.8×10^3	4.2
MhpC, pH 8.0[b]	4.1×10^6	
N109A	3.3×10^4	2.9
N109H	1.9×10^4	3.2
F173G	1.3×10^4	2.0
F173D	2.6×10^4	3.0
R188Q	1.4×10^3	4.7
R188K	1.9×10^4	3.2
C261A	2.9×10^6	0.2
W264G	2.1×10^4	3.1
DxnB2, pH 7.5	1.2×10^7	
N43A	4.9×10^5	1.9
N43D	7.9×10^2	5.7
N43H	2.3×10^4	3.7
R180K	2.5×10^5	2.3
R180M	2.9×10^2	6.3
R180Q	5.4×10^2	5.9

[a,b] k_{cat}/K_m values were taken from references [81] and [65], respectively.

Analysis of steady-state kinetic data. Contributions of individual residues to transition state stabilization were estimated from previously measured steady-state kinetic parameters for $BphD_{LB400}$, MhpC and those presented in this work for DxnB2. The analysis was performed as previously described for a C35G variant of tyrosyl-tRNA synthetase[141]. Briefly, the specificity constants were compared using the following equation: $\Delta G_R = RT\ln[(k_{cat}/K_m)_{mut} / (k_{cat}/K_m)_{WT}]$, which assumes that the transition state energy is unaffected by substitution, and that the mutated side-chains do not affect productive binding of a second substrate, in this case H_2O.